THESIS

DIAGNOSING MONTHLY MEAN BOUNDARY LAYER PROPERTIES FROM RE-ANALYSIS DATA USING A MIXED-LAYER MODEL

Submitted by

Maike Ahlgrimm

Department of Atmospheric Science

In partial fulfillment of the requirements

For the Degree of Master of Science

Colorado State University

Fort Collins, Colorado

Spring 2004

ABSTRACT OF THESIS

DIAGNOSING MONTHLY MEAN BOUNDARY LAYER PROPERTIES FROM RE-ANALYSIS DATA USING A MIXED-LAYER MODEL

The mixed-layer approach to modeling the planetary boundary layer (PBL) is particularly well suited to inversion-topped PBLs, such as the stratocumulus-topped boundary layer found off the continental American coasts in the subtropical Pacific ocean. However, a strong temperature inversion near 850 hPa (the trade-wind inversion) is not confined to the stratocumulus regimes, but has been observed over most parts of the subtropical-tropical Pacific ocean. In this thesis, we test a simple mixed-layer model's (MLM) ability to diagnose PBL depth, entrainment velocity and cumulus mass flux velocity from monthly mean re-analysis data. Part of this test involves a comparison between the Colorado State University's General Circulation Model (CSU GCM) and the MLM run with input data from the CSU GCM. The results are also compared to available observations. Then we examine the sensitivity of the MLM to changes in the formulation of some of the input parameters.

The MLM succeeds in diagnosing positive PBL depths and entrainment velocities on the order of hundreds of meters and $\mathrm{mm\,s^{-1}}$, respectively. Convective regions are marked by deep PBLs in the MLM's output, and entrainment is generally large where the PBL is deep. The cumulus mass flux velocity is the least reliable field of the model output and is negative in some regions.

Observations with similar spatial and temporal coverage as the model output are as yet unavailable. The available observations, in particular of PBL depth, are used as guidelines for the evaluation and interpretation of the model output.

In the process of comparing the MLM to the GCM, some strengths and weaknesses of the GCM are discussed. Among the strengths are very smooth monthly mean fields for PBL depth, entrainment and cumulus mass flux velocities. The PBL depth is of comparable magnitude to available observations. Some of the weaknesses are a very moist free atmosphere, a low surface sensible heat flux and negative entrainment velocities along the continental coasts.

Maike Ahlgrimm
Department of Atmospheric Science
Colorado State University
Fort Collins, CO 80523
Spring 2004

ACKNOWLEDGMENTS

I would like to extend my sincerest appreciation to my advisor Dr. David A. Randall for his guidance and support throughout this work. He is a great mentor, and I feel very lucky to have had the chance to learn from him. I would also like to thank Drs. David W. J. Thompson and Michael J. Kirby for officiating on my committee.

All of Randall's Rabbits have contributed to this work one way or another by keeping their doors open and answering my questions. You guys are awesome!

Thanks to the CSU Lutheran Campus Ministry, and Pastor Connie Winter-Eulberg in particular, for making me feel at home in Fort Collins.

Last but not least, I would like to thank the *Evangelisches Studienwerk e.V.* in Germany for their support and counsel. Without it, I never would have considered studying abroad, nor applying to CSU.

This research was funded through the Pan American Climate Studies (PACS) of the National Oceanic and Atmospheric Administration under contract #NA17RJ1228.

TABLE OF CONTENTS

LIST OF TABLES

LIST OF FIGURES

FIG. 3.11: Monthly mean incidence of PBL stratus clouds in %. Black indicates areas of 0% incidence. - 40

FIG. 3.12: Monthly mean 10 m wind divergence and 10 m winds. Zero contour in black. - 40

FIG. 3.13: Monthly mean cumulus mass flux velocity - - - - - - - - - - - - - - - - - - 41

FIG. 3.14: Monthly mean entrainment velocity. Zero contour in white. - - - - - - - 41

FIG. 3.15: Monthly mean PBL depth - 41

FIG. 3.16: PBL depth calculated by MLM from GCM input. White areas (other than continents) indicate above-scale values. - 43

FIG. 3.17: Entrainment velocity calculated by MLM from GCM input. White areas (other than continents) indicate above-scale values. Same scale as in Fig. 3.14. - 44

FIG. 3.18: Same entrainment velocity as in Fig. 3.17, but on a different scale to show more detail. - 44

FIG. 3.19: Cumulus massflux as calculated by the MLM from GCM input fields. White areas (other than continents) indicate above-scale values. - - - - - - - - - - - - - - 44

FIG. 3.20: Difference plot: GCM PBL depth minus MLM PBL depth. Black indicates areas of below-scale values. - 48

FIG. 3.21: Difference plot of GCM PBL depth minus MLM PBL from model equations including all corrective terms except $q1$. - 51

FIG. 3.22: Difference plot of GCM PBL depth minus MLM PBL depth from model equations including all corrective terms except $\theta 1$. - - - - - - - - - - - - - - - - - - 51

FIG. 3.23: Difference plot of GCM PBL depth minus MLM PBL depth from model equations including all corrective terms except $\theta 1$ and $q1$. - - - - - - - - - - - - - 51

FIG. 3.24: Difference plot of GCM PBL depth minus MLM PBL depth from model equations including all corrective terms except $q3$. Black indicates areas of below-scale values. The black solid line is the zero contour. Notice: Scale has changed. - 51

FIG. 3.25: Difference plot of GCM PBL depth minus MLM PBL depth from model equations including all corrective terms except $\theta 3$. The black solid line is the zero contour. White along the ITCZ indicates above scale values. Notice: Scale has changed. - 52

FIG. 3.26: Difference plot of GCM PBL depth minus MLM PBL depth from model equations including all corrective terms except $\theta3$ and $q3$. The black solid line is the zero contour. - 52

FIG. 3.27: Difference plot of GCM PBL depth minus MLM PBL depth from model equations including all corrective terms except $q2$. Black indicates areas of below-scale values. The black solid line is the zero contour. - - - - - - - - - - - - - - - - - 52

FIG. 3.28: Difference plot of GCM PBL depth minus MLM PBL depth from model equations including all corrective terms except $\theta2$. Black indicates areas of below-scale values. The black solid line is the zero contour. - - - - - - - - - - - - - - - - - 52

FIG. 3.29: Difference plot of GCM PBL depth minus MLM PBL depth from model equations including all corrective terms except $q2$ and $\theta2$. Black indicates areas of below-scale values. The black solid line is the zero contour. - - - - - - - - - - - 53

FIG. 3.30: Scatterplots of a) $q3$ vs. the monthly mean entrainment velocity and b) $\theta3$ vs. the monthly mean entrainment velocity, only grid points over the ocean are included - 54

FIG. 3.31: $\overline{w_E(q_H - q_B)}$ - 55

FIG. 3.32: $\overline{w_E(\theta_H - \theta_B)}$ - 55

FIG. 3.33: $\overline{w_E}(\overline{q_H} - \overline{q_B})$ - 55

FIG. 3.34: $\overline{w_E}(\overline{\theta_H} - \overline{\theta_B})$ - 55

FIG. 3.35: MLM PBL depth, only corrective terms in model equations are q_term_2 and th_term_2. - 58

FIG. 4.1: Monthly Mean Surface evaporation from NCEP re-analysis - - - - - - - 61

FIG. 4.2: Monthly mean surface sensible heat flux from NCEP re-analysis - - - - 62

FIG. 4.3: Monthly mean radiative cooling factor from NCEP re-analysis - - - - - - 63

FIG. 4.4: Shaded contours: Monthly mean 10 m wind divergence, zero contour in black. Arrows: Monthly mean10 m wind vectors. Data from NCEP re-analysis - - - - 65

FIG. 4.5: Monthly mean water vapor mixing ratio of the mixed PBL from NCEP re-analysis - 66

FIG. 4.6: Monthly mean water vapor mixing ratio above the PBL top from NCEP re-

analysis - 67

FIG. 4.7: Monthly mean dry static energy per specific heat at constant pressure (c_p) of the mixed PBL from NCEP re-analysis- 69

FIG. 4.8: Monthly mean dry static energy per specific heat at constant pressure (c_p) above the PBL top from NCEP re-analysis - 70

FIG. 4.9: Monthly mean sea-surface temperature from NCEP re-analysis - - - - - 72

FIG. 4.10: Monthly mean sea-level pressure from NCEP re-analysis - - - - - - - - - 73

FIG. 4.11: MLM PBL depth from NCEP re-analysis input. White areas indicate above-scale values, black areas indicate below-scale values - - - - - - - - - - - - - - - - - 75

FIG. 4.12: MLM entrainment velocity from NCEP re-analysis input. White areas indicate above-scale values, black areas indicate below-scale values. - - - - - - 76

FIG. 4.13: MLM cumulus mass flux velocity from NCEP re-analysis input. White areas indicate above-scale values, black areas indicate below-scale values. Zero contour in black. - 78

FIG. 4.14: w_E^q calculated from the moisture equation only, assuming uniform PBL depth of 1000 m. - 81

FIG. 4.15: w_E^s calculated from the dry static energy equation only, assuming uniform PBL depth of 1000 m. - 81

FIG. 4.16: a) Covariance $\overline{\mathbf{v}' \cdot \nabla q'}$ from the GCM run for data every 200s.b) Covariance $\overline{\mathbf{v}' \cdot \nabla \theta'}$ from the GCM run for data every 200s. - 83

FIG. 4.17: a) Covariance $\overline{\mathbf{v}' \cdot \nabla q'}$ from the MLM run with NCEP re-analysis input for April 2001, four times daily. Covariance $\overline{\mathbf{v}' \cdot \nabla \theta'}$ from the MLM run with NCEP re-analysis for April 2001, four times daily. - 83

FIG. 4.18: Locations of the radiosonde observations - 84

FIG. 4.19: Time series of GCM a) entrainment velocity, b) cumulus mass flux velocity, c) PBL depth and d) surface buoyancy flux at the Galapagos location (~90W,1S) for the sample month. The vertical lines are 24 hour markers at 00 UTC. - - - - - - 95

FIG. 4.20: Time series of GCM a) entrainment velocity, b) cumulus mass flux velocity,

c) PBL depth and d) surface buoyancy flux at the Chuuk location (~152E,7N) for the sample month. The vertical lines are 24 hour markers at 00 UTC. - - - - - - - - - - 96

FIG. 4.21: Time series of GCM a) entrainment velocity, b) cumulus mass flux velocity, c) PBL depth and d) surface buoyancy flux at the coastal location (81.1W, 2.8S) for the sample month. The vertical lines are 24 hour markers at 00 UTC. - - - - - - 98

FIG. 4.22: Schematic of water vapor mixing ratio (green) and dry static energy per specific heat (red) profiles for a stratocumulus topped PBL. Dashed lines indicate the profiles for the mixed layer assumption. Solid lines show actual profile. - - - - 101

FIG. 4.23: Difference in PBL depth between regular MLM run with monthly mean input from NCEP re-analysis data and a run where the mixed layer value of q is reduced by 10% and the mixed layer value of s is increased by $L_C \cdot 0.1 q_B$. Regions with above-scale values are white. - 103

FIG. 4.24: PBL depth from MLM run with monthly mean input from NCEP re-analysis data. The mixed layer value of q is decreased by 10% and the mixed layer value of s is increased by $L_C \cdot 0.1 q_B$. Regions with above-scale values are white, with below-scale values are black. - 104

FIG. 4.25: Difference in entrainment velocity between regular MLM run with monthly mean input from NCEP re-analysis data and a run where the mixed layer value of q is reduced by 10% and the mixed layer value of s is increased by $L_C \cdot 0.1 q_B$. Regions with above-scale values are white. - 105

FIG. 4.26: Entrainment velocity from MLM run with monthly mean input from NCEP re-analysis data. The mixed layer value of q is decreased by 10% and the mixed layer value of s is increased by $L_C \cdot 0.1 q_B$. Regions with above-scale values are white, with below-scale values are black. - 106

FIG. 4.27: Difference in cumulus mass flux velocity between regular MLM run with monthly mean input from NCEP re-analysis data and a run where the mixed layer value of q is reduced by 10% and the mixed layer value of s is increased by $L_C \cdot 0.1 q_B$. Regions with above-scale values are white, with below-scale values are black. - 107

FIG. 4.28: Cumulus mass flux velocity from MLM run with monthly mean input from NCEP re-analysis data. The mixed layer value of q is decreased by 10% and the mixed layer value of s is increased by $L_C \cdot 0.1 q_B$. Regions with above-scale values are white, with below-scale values are black. - 108

Chapter 1: Introduction and Literature Review

1-A: Theory

The atmosphere over the tropical and subtropical oceans is a rich field for studies. From the modeler's perspective, it is an area of numerous challenges. So far, most general circulation models (GCMs) fail to realistically reproduce subtropical and tropical features such as the location of the intertropical convergence zone (ITCZ) and the transition between regions of marine stratocumuli and shallow trade wind cumuli (e.g. Randall et al.,1998, Kirtman et al., 2002). Marine stratocumulus clouds have been recognized as important players in climate (Klein and Hartmann, 1995; Ma et al., 1996). Due to their high albedo and strong long wave emission, they act to cool the Earth. The wide basin of the tropical and subtropical Pacific accommodates a variety of distinctly different regimes: The marine stratocumulus regime, the trade wind cumulus regime and the transition between those two cloud types, the well defined band of deep convection (the ITCZ) and the warm pool regime. Because of this diversity, the Pacific makes a good test bed for the model that will be presented in this thesis.

The concept of a well-mixed, slab-like boundary layer topped by a strong inversion in the subtropical regions of subsidence has been well established for over half a century. Early work on this subject was done by Bunker et al. (1949), Malkus (1958), Ball (1960)

and Lilly (1968). The large scale subsidence produced by the descending branch of the Hadley cell creates a warm, dry mid and upper tropospheric air mass overlying a relatively cool and moist turbulent boundary layer. The temperature inversion separating those two air masses is particularly strong over the cold upwelling regions of the eastern ocean basins. Evaporation from the sea surface and cool air temperatures under the inversion lead to high relative humidities. Since the moisture is trapped under the inversion, extensive marine stratocumulus clouds can develop over the cold ocean. Farther equatorward, where the sea-surface temperatures increase and the strength of the inversion decreases, the stratocumulus decks start to break up and shallow trade wind cumuli are common (Randall et al., 1998).

Lilly's original model concentrated on the stratocumulus-topped boundary layer (STBL), which is a very persistent feature in the eastern ocean basins. Subsidence and low level divergence in those areas work together to lower the temperature inversion. In order to maintain the inversion against the subsidence, the warm, dry upper air must pass through the boundary represented by the inversion. As the air is entrained into the boundary layer it acquires the boundary layer's properties by means of a moisture flux convergence and radiative, as well as evaporative cooling at the boundary-layer top. If this were not the case, there would be no distinct temperature inversion.

In most planetary boundary layer (PBL) models, including Lilly's, the rate at which this entrainment takes place must be parameterized. Lilly's model can be run with two alternative parameterizations: the 'maximum entrainment condition' and 'minimum

entrainment condition'.

Subsequent studies expanded on Lilly's model. Schubert (1976) assumed that the 'true' entrainment rate lies somewhere between the maximum and the minimum cases investigated by Lilly. Hence, he used an average of Lilly's maximum and minimum closure assumptions, weighted by an entrainment parameter. With those alterations, Schubert then investigated the sensitivity of the model to changes in sea-surface temperature, large-scale divergence and the entrainment parameter. He also introduced a diurnal cycle forced by a diurnally varying radiative flux. One of Lilly's original insights was the importance of a radiative cooling concentrated at the boundary-layer top. Schubert et al. (1979) and Randall (1980 a) found that radiative cooling applied over a thin layer at the top of the PBL has a strong influence on the turbulent fluxes and entrainment, and thus the PBL structure.

A major shortcoming of Lilly's mixed-layer model is, ironically, also one of its strengths: the model's simplicity. More complex models have been developed that make it possible to describe the vertical structure of the PBL in more detail, and that can deal with horizontally and vertically inhomogeneous PBLs.

In any set of equations that describes the statistics of turbulent flow, there are more unknowns than equations. Introducing additional predictive equations to solve for those unknowns (higher-order moments) only leads to additional unknowns. This is referred to as the 'closure problem'. In order to solve a set of equations (i.e. close the set of equations), the number of equations must equal the number of unknowns.

Parameterization effectively adds to the number of equations without adding to the number of unknowns by expressing higher-order moments in terms of the already existing unknowns. The mixed-layer model, in this framework, is a turbulent boundary-layer model of “simplified first-order closure” (Mellor and Yamada, 1974), or “half-order closure” (using terminology from Stull, 1988). In a first-order closure model, the mean quantities of the variables are predicted at each level. Fluxes are parameterized, the simplest parameterization being down-gradient mixing. In the simplified first-order closure model (mixed-layer model), the vertical profiles of the predicted variables (wind, temperature etc.) are prescribed throughout the PBL, but their mean values are predicted.

Higher-order closure (HOC) models include predictive equations for higher-order moments, e.g. the turbulent kinetic energy equation. The closure level of the model indicates how many of the higher-order moments are predicted, the rest being parameterized. First order turbulent PBL models with down-gradient mixing as closure parameterization only communicate with the neighboring levels, and are referred to as ‘local’ closure models (Moeng and Wyngaard, 1989). This is appropriate for PBLs that are dominated by local processes and small scale eddies, such shear-driven PBLs. These models cannot describe convective PBLs in which large-scale eddies transport properties of the air all the way from the surface to the top of the PBL (a ‘non-local’ process). The mixed-layer model predicts the PBL properties from fluxes diagnosed at the surface and at the PBL top, and therefore falls into the category of ‘non-local’ closure models.

In second- and third-order closure models, some of the transport terms are

predicted, but often the third- and fourth-order moments are still parameterized with down-gradient mixing (Bougeault and Andre, 1986). In the framework of turbulent PBL models, the weaknesses of the mixed-layer model are apparent. In regions where the PBL is not well mixed, the model cannot be expected to perform well. The model is also non-local. Mixed-layer models therefore won't perform well in regions where local processes are important (e.g. shear-driven PBLs). These constraints on the mixed-layer model were recognized some time ago, and an effort has been made to improve PBL models with higher order closures that can describe local and non-local processes (e.g. Deardorff, 1966, Holtslag and Moeng, 1991) and that work for other than well-mixed PBLs (Stull, 1988).

Parallel to the development of more sophisticated HOC, the concept of mass flux closure was introduced (Arakawa, 1969). The mass flux scheme, whose basic concept is the parameterization of vertical fluxes as an updraft area fraction (cloud) multiplied by the difference of updraft and downdraft properties, was originally introduced to describe deep convective cumulus clouds. Later on, the mass flux concept was adapted to dry convection in the PBL (Betts, 1976, Wang and Albrecht, 1990) and PBLs with shallow cumulus clouds (Lappen and Randall, 2001)

Most closure schemes seem to work best for a particular PBL type or cloud type; therefore the majority of research has been done on distinct regimes (e.g. stratocumulus, shallow cumulus, deep convection, dry convection, shear-driven PBL etc.). More recently, a focus has been to develop a PBL parameterization that works for at least several of those

regimes, if not all, (Lappen and Randall 2001) and/or includes both cloud parameterization and PBL parameterization (Grenier and Bretherton, 2001, Bretherton et al., submitted to M. Wea. Rev. 2003).

Despite these more recent developments, Lilly's model continues to be widely used. Even though it is not applicable to all types of PBL, it remains a very simple and elegant description of the mixed, inversion-topped boundary layer and variations of it are in fact part of GCMs currently in use. Its simplicity and low computational expense will probably keep it in use for some time to come.

As Moeng (2000) points out, we have a fairly good idea how e.g. radiative cooling at the cloud top *qualitatively* influences the inversion height, but we know little about the *quantitative* effect of the cooling on the inversion height. The extensive work with Lilly-type mixed-layer models has greatly contributed to this qualitative understanding of the processes involved in maintaining a STBL. As it is very difficult to obtain PBL observations with large spatial and temporal coverage, out quantitative understanding of the PBL, particularly of the vertical mass fluxes, is still limited. In most of the studies mentioned above, entrainment and vertical mass fluxes are parameterized. Predicting these fluxes from the model equations may improve our quantitative understanding.

1-B: Observations

Entrainment, unfortunately, is very hard to measure. Observational estimates of this quantity are scarce. The depth of the boundary layer can be determined more easily from radiosonde and dropsonde measurements. More recently, satellite products, such as

cloud-top pressure, can give an estimate of the inversion height in the STBL regions. However, the Pacific is still a very remote region, and the data acquired during measurement missions by no means provide complete spatial coverage. Furthermore, the missions' durations are usually limited to a few months.

Von Ficker (1936) and Neiburger (1961) were among the first to produce a map of the inversion base height over the Atlantic and Pacific respectively. Their work, as well as subsequent studies (for an overview, see Schubert et al. 1995), shows a picture of a fairly uniform inversion base pressure of about 800 to 850 hPa over the Pacific and Atlantic with a rather weak upslope of about 300 m height per1000 km distance towards the ITCZ.

Since then, measurement missions like the First GARP Global Experiment (FGGE; GARP: Global Atmospheric Research Program) in 1979, the Tropical Ocean Global Atmosphere/Coupled Ocean-Atmosphere Response Experiment (TOGA/COARE) in 1992/93 and the East Pacific Investigation of Climate (EPIC) in 2001 have provided us with better coverage of the vertical atmospheric structure over the tropical Pacific.

Data obtained from FGGE corroborates Neiburger's and von Ficker's observations of a fairly uniform inversion height of 850 to 800 hPa over the central and eastern Pacific (160 W to 90W, 10S to 15N) (Firestone and Albrecht 1986, Kloesel and Albrecht 1989, Yin and Albrecht 2000). Yin and Albrecht's study observes in particular that, even though only 30% of the soundings in the ITCZ region show a stable boundary-layer structure, the inversion height in those stable cases does not differ much from that outside the ITCZ.

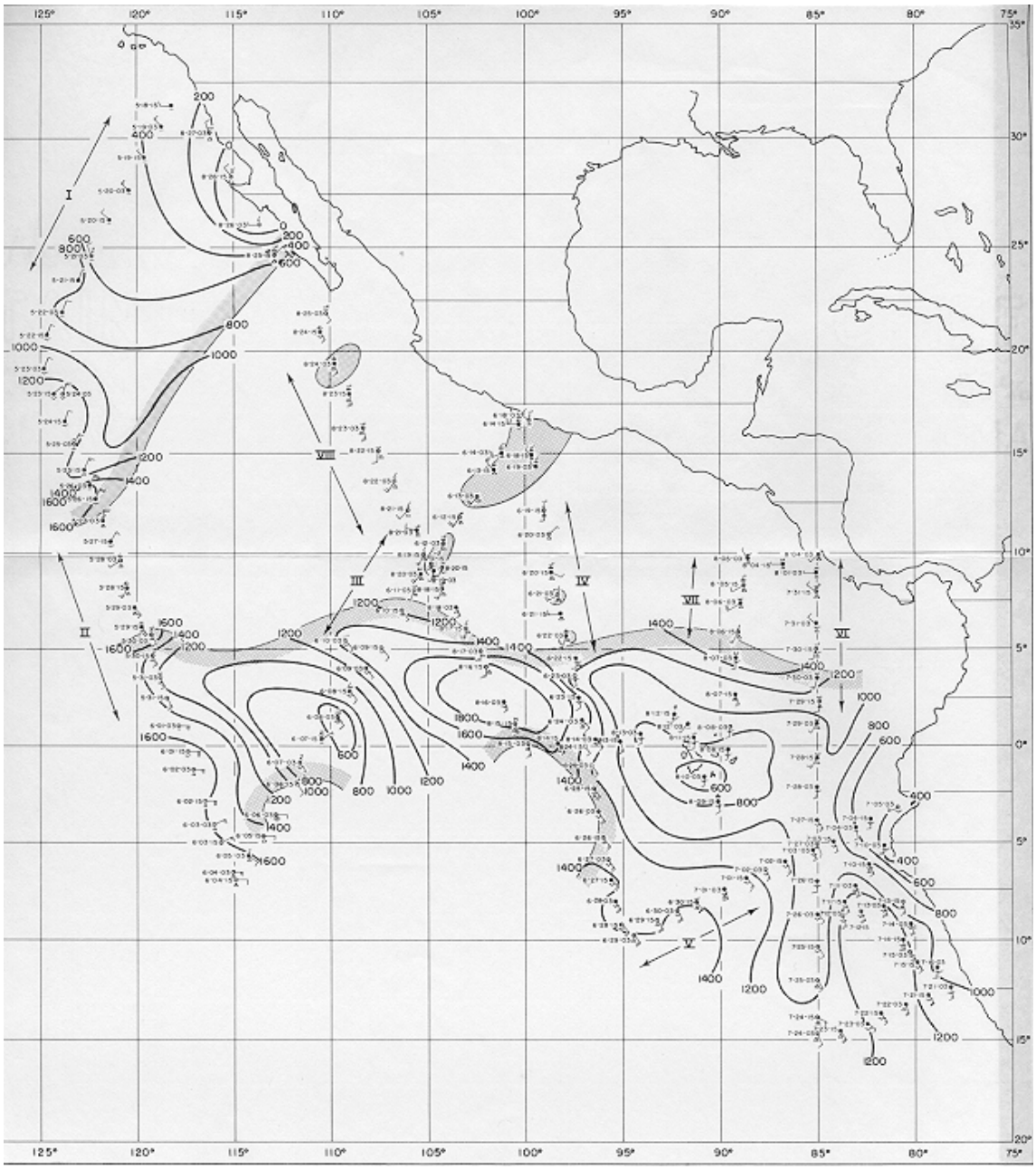

Figure 1.1: Plot of inversion base height from 1952 cruises of the Horizon. Figure taken from Neiburger (1961)

From a purely thermodynamic viewpoint that considers only local properties like sea surface temperature and divergence, a significantly stronger upslope towards the ITCZ would be expected. Schubert et al. (1995) argue that not only local subsidence and entrainment determine the inversion height, but that advection of the inclined inversion layer has an important influence as well. Thus, dynamical adjustment processes act to extend the low-level inversion of the stable regions towards the ITCZ, leading to a slope close to the observations.

Strong downdrafts in the vicinity of deep convection may also contribute to a lower inversion height. Cool air penetrating the boundary layer in a strong downdraft and spreading out along the surface could conceivably form a new mixed layer underlying the old boundary layer, if mixing were constrained to the cool air mass of the downdraft. The new mixed layer's top would then be lower than the old one's.

Observations from TOGA COARE show the common occurrence of an inversion at about 800 hPa as well (Johnson et al. 1993, Johnson et al. 1996).

This study incorporates the very basic concepts of the mixed boundary layer into a simplified two-layer slab model that predicts the boundary-layer depth as well as the entrainment and cumulus mass fluxes across the boundary-layer top. The domain spans the tropical Pacific (Fig. 1.2). Surface heat and moisture fluxes, radiative cooling, the wind field and the properties of boundary-layer air as well as above-boundary-layer air are all prescribed fields, taken from either a GCM run or from National Centers for Environmental Prediction (NCEP) re-analysis data. The model results are then compared

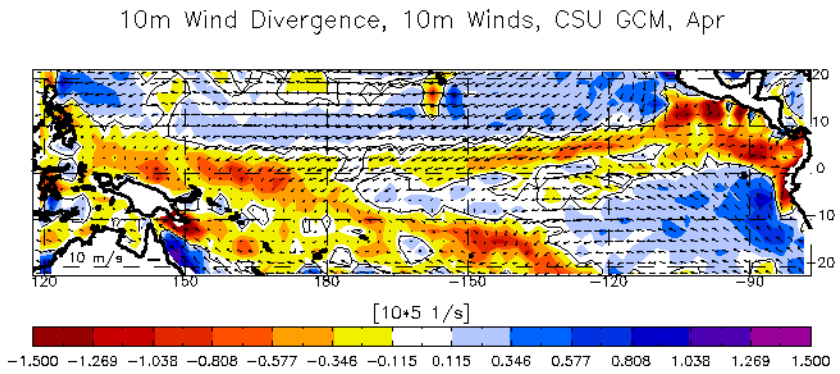

Figure 1.2: Domain covered by the mixed-layer model discussed in this thesis

to GCM output and direct measurements of the inversion from radiosondes and dropsondes, as well as to a cloud-top pressure product.

1-C: The PBL in different regimes

Since the model described in this thesis predicts the PBL depth, it is a quantity that will be mentioned a lot. The question remains which part of the atmosphere can be termed the PBL, and how it is defined in the observations, the models and the theoretical concepts on which the models are based. The mixed-layer concept equates the mixed layer with the PBL and the mixed-layer depth is identical to the PBL depth. In the real atmosphere, the PBL can be defined as the part of the troposphere that is directly influenced by the presence of the Earth's surface and responds to surface forcings on rather short time scales.

Several distinct regimes can be distinguished in the model domain. There are transitional regions, and regions that cannot be classified into any of the regimes, but three regimes mentioned below show some distinct PBL characteristics.

The stratocumulus regime, located over the cold upwelling ocean on the eastern boundaries of the Pacific basin, is characterized by a well-mixed PBL with a distinct top. Here, the large scale subtropical subsidence creates a dry, warm free atmosphere overlying a cool and moist layer. Stratocumulus clouds form under the strong temperature inversion (trade inversion) that separates the two air masses. Here, the distinction between the PBL and the free atmospheric is quite obvious: the layer under the trade inversion is cold and moist and therefore influenced by the underlying ocean, the free atmosphere above the inversion is not. In the temperature soundings discussed in Chapter 5, we will assume that the base of the temperature inversion is coincident with the PBL top. The PBL can be further divided into subcloud and cloud layers. In the stratocumulus regime, several conservative quantities (total water, equivalent potential temperature) are still well mixed throughout the subcloud and the cloud layer, so the cloud layer is usually considered to be part of the PBL.

The stratocumulus regime transitions into the trade cumulus regime over warmer waters. The trade cumulus regime is characterized by a well mixed subcloud layer topped by a weak inversion under shallow cumulus clouds capped by the trade inversion. While the subcloud layer is still well mixed, the cloud layer is less so, and whether the PBL is considered to include only the subcloud layer or both subcloud and cloud layer is a matter of discussion.

In the deep convective regime in the warm pool and along the ITCZ and SPCZ, the subcloud layer is still well mixed and capped by a weak inversion, but the cumulus clouds

above it can rise all the way to the tropopause. Here, the subcloud layer is clearly identified as the PBL. During times of suppressed convection, the situation in the warm pool may resemble the trade cumulus regime (when only shallow convection exists) or even the stratocumulus regime (without the clouds) when the trade inversion is dominant and the air is well mixed up to the trade inversion.

As we will see in Chapters 3 and 4, the Colorado State University (CSU) GCM seems to place its PBL top at the top of the subcloud layer: the PBL depth is low in the warm pool under the deep convective clouds and higher in the east Pacific in the stratocumulus regime. The mixed-layer model discussed in this thesis, however, increases the PBL depth towards the deep convective regime. This makes sense if the mixed-layer model's PBL top follows the trade inversion, which is lowest over stratocumulus and lifts over shallow convection. In the convective regions where the trade inversion disappears, at least during convective phases, it is not completely clear where the mixed-layer model places the PBL top.

These regimes shift and change with the seasons, as well as interannually. In the northern hemispheric summer, the ITCZ shifts northward, in the winter southward. Its intensity is maximal during the northern hemisphere's summer and fall. In March and April, a southern-hemisphere ITCZ can sometimes be observed (e.g. Lietzke et al., 2001). On an interannual time scale, the deep convection in the Pacific is influenced primarily by the El Niño- Southern Oscillation (ENSO). During the warm phase (El Niño), the deep convection shifts from the west Pacific toward the central Pacific, the upwelling off the

Chilean coast is suppressed and the sea-surface temperature (SST) in the eastern Pacific is higher than normal. In the cold phase (La Niña) the contrast in SST across the Pacific basin is at its maximum, with very cold temperatures in the east Pacific and a very pronounced cold tongue along the Equator. The deep convection is strongest in the far west Pacific. A pronounced cold tongue favors the development of a southern ITCZ in the northern hemispheric spring (Waliser and Gautier, 1993). The year 2001, that the sample months in this study are taken from, was predominantly a neutral ENSO year.

Chapter 2 describes the mixed-layer model used in this study, the data used as model input as well as some observations. The results from the mixed-layer model runs will be discussed in Chapters 3 and 4. In Chapter 5, those results will be compared to observations, and a summary and conclusions will be presented in Chapter 6.

Chapter 2: Model Description and Data

2-A: Derivation of model equations

The boundary-layer model used in this work is based on three conservation equations, one each for mass, water vapor mixing ratio and dry static energy. The mass conservation equation is derived starting from the continuity equation in height coordinates:

$$\frac{\partial \rho}{\partial t} = -\nabla \cdot (\rho \mathbf{v}) . \tag{2.1}$$

Here, $\mathbf{v}$ denotes the three dimensional wind vector. Integrating (2.1) with respect to height from the surface to the boundary-layer top H yields

$$\int_0^H \frac{\partial \rho}{\partial t} dz = -\int_0^H \nabla \cdot (\rho \mathbf{v}) dz . \tag{2.2}$$

Applying the Leibnitz rule to (2.2) leads to

$$\frac{\partial}{\partial t}\int_0^H \rho dz - \rho_H \frac{\partial H}{\partial t} = -\nabla \cdot \int_0^H (\rho \mathbf{v}) dz + \rho_H \mathbf{v}_H \cdot \nabla H \tag{2.3}$$

$$\frac{\partial}{\partial t}(\rho H) - \rho_H \frac{\partial H}{\partial t} = -\nabla_h \cdot \int_0^H (\rho \mathbf{v}_h) dz - \frac{\partial}{\partial z}\int_0^H (\rho w) dz + \rho_H \mathbf{v}_{hH} \cdot \nabla_h H . \tag{2.4}$$

In (2.4), the horizontal and vertical derivatives on the right hand side have been separated. The subscript h denotes a horizontal operator or vector. The density ρ_0 throughout the depth of the boundary layer is assumed to be constant. Defining the horizontal bulk wind $\mathbf{v}_{hB}$ of the boundary layer

$$\mathbf{v}_{hB} = \frac{1}{H}\int_0^H \mathbf{v}_h dz , \tag{2.5}$$

(2.4) can be written as

$$\frac{\partial}{\partial t}(\rho H) - \rho_H \frac{\partial H}{\partial t} = -\rho_0 \nabla_h \cdot (H \mathbf{v}_{hB}) - \int_{\rho w(0)}^{\rho w(H)} d(\rho w) + \rho_H \mathbf{v}_{hH} \cdot \nabla_h H \ . \tag{2.6}$$

For purposes of this model, the sea surface is assumed to be flat and stationary, so that

$$w(0) = 0 \tag{2.7}$$

and

$$\frac{\partial}{\partial t}(\rho H) + \rho_0 \nabla_h \cdot (H \mathbf{v}_{hB}) = \rho_H \left(\frac{\partial H}{\partial t} + \mathbf{v}_{hH} \cdot \nabla_h H - w_H \right) . \tag{2.8}$$

Here, w_H is the vertical velocity of an air particle at $z = H$. The right-hand-side of (2.8) describes the net mass flow across the PBL top. We can substitute $\rho_H(w_E - w_C)$ for $\rho_H\left(\frac{\partial H}{\partial t} + \mathbf{v}_{hH} \cdot \nabla_h H - w_H\right)$, where $\rho_H w_C$ is the area-averaged upward cumulus mass flux across the PBL top and $\rho_H w_E$ is the area-averaged entrainment mass flux across the PBL top. Using this notation and averaging over time, equation (2.8) reduces to

$$\overline{\rho_0 \frac{\partial}{\partial t}(H)} + \overline{\rho_0 \nabla_h \cdot (H \mathbf{v}_{hB})} = \overline{\rho_H (w_E - w_C)}, \tag{2.9}$$

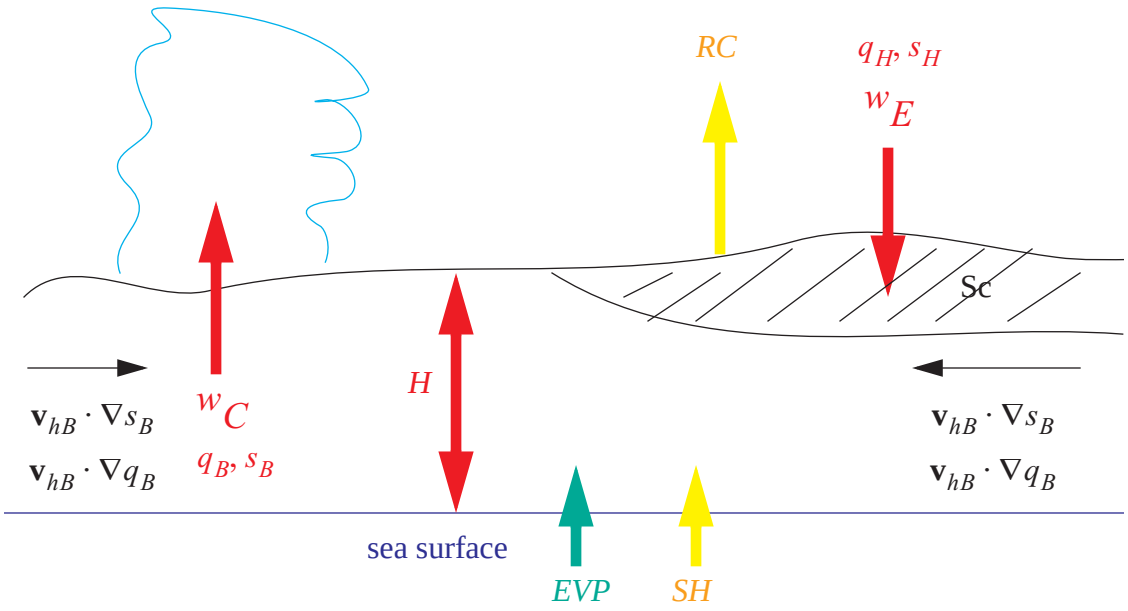

Figure 2.1: Schematic of the processes accounted for in the non-precipitating model. Notation as in the text.

where the overbar denotes the time average. For simplicity, we will assume that the covariances are negligible, i.e. that (2.9) is equal to

$$\overline{\rho_0}\frac{\partial}{\partial t}\overline{H} + \overline{\rho_0}\nabla_h \cdot (\overline{H}\overline{\mathbf{v}_{hB}}) \;=\; \overline{\rho_H}(\overline{w_E} - \overline{w_C})\,. \tag{2.10}$$

Dropping the overbars and assuming steady state for the PBL depth leads to

$$\rho_0\nabla_h \cdot (H\mathbf{v}_{hB}) \;=\; \rho_H(w_E - w_C)\,. \tag{2.11}$$

Whether or not neglecting the covariances is a good approximation will be discussed in Chapter 3.

The water-vapor equation can be derived in a similar manner. Starting from the continuity equation and the moisture equation:

$$\frac{\partial \rho}{\partial t} \;=\; -\nabla \cdot (\rho\mathbf{v}) \tag{2.12}$$

$$\frac{\partial q}{\partial t} \;=\; -\mathbf{v} \cdot \nabla q + S\,. \tag{2.13}$$

Here, q is the water vapor mixing ratio and S are sources and sinks of water vapor. Multiplying (2.12) by q and (2.13) by ρ and adding the two leads to

$$\frac{\partial}{\partial t}(\rho q) \;=\; -\nabla \cdot (q\rho\mathbf{v}) + S\rho \tag{2.14}$$

Integration with respect to height and separation of horizontal and vertical derivatives yields

$$\frac{\partial}{\partial t}\int_0^H (q\rho)dz - \rho_H q_H \frac{\partial H}{\partial t} = -\int_0^H \nabla_h \cdot (q\rho \mathbf{v}_h)dz - \int_0^H \frac{\partial}{\partial z}(wq\rho)dz + \int_0^H S\rho dz \qquad (2.15)$$

$$\frac{\partial}{\partial t}\int_0^H (q\rho)dz - \rho_H q_H \frac{\partial H}{\partial t} = \\ -\nabla_h \cdot \int_0^H (\rho q \mathbf{v}_h)dz - \rho_H q_H \mathbf{v}_{hH} \cdot \nabla_h H - \int_{\rho qw(0)}^{\rho qw(H)} d(\rho qw) + \int_0^H S\rho dz \qquad (2.16)$$

Defining the bulk water vapor mixing ratio $q_B \equiv \frac{1}{H}\int_0^H q dz$, and assuming that the horizontal bulk water vapor transport can be expressed by $\rho_0 q_B \mathbf{v}_{hB} \equiv \frac{1}{H}\int_0^H \rho q \mathbf{v}_h dz$, equation (2.16) can be rewritten as:

$$\frac{\partial}{\partial t}(q_B H \rho_0) + \nabla_h \cdot (H q_B \mathbf{v}_{hB} \rho_0) = \rho_H q_H \left(\frac{\partial H}{\partial t} + \mathbf{v}_{hH} \cdot \nabla_h H - w_H\right) + \int_0^H S\rho dz . \qquad (2.17)$$

Under the same assumptions as for the mass equation (steady state, covariances neglected, overbars dropped), and substituting for the right-hand-side bracket with w_C and w_E, the time averaged equation (2.17) simplifies to (2.18):

$$\nabla_h \cdot (Hq_B \mathbf{v}_{hB}) = w_E q_H - w_C q_B + \frac{1}{\rho_0} \int_0^H S\rho dz . \tag{2.18}$$

Here, the assumption has been made that the densities of the boundary-layer air and of the air mass above it are approximately the same:

$$\rho_0 = \rho_H . \tag{2.19}$$

This assumption is fairly good in the entrainment terms because the mass transported across the PBL top has in fact the density of just below H and just above H. For the case of a discontinuous PBL top, ρ_0 and ρ_H are very close.

Surface evaporation EVP and precipitation P are the moisture source and sink:

$$\nabla_h \cdot (Hq_B \mathbf{v}_{hB}) = w_E q_H - w_C q_B + \frac{EVP - P}{\rho_0} \tag{2.20}$$

Analogously, the equation for dry static energy can be derived:

$$\nabla_h \cdot (s_B H \mathbf{v}_{hB}) = w_E s_H - w_C s_B + \frac{SH + L_C P - RC}{\rho_0} \tag{2.21}$$

Here, $s_B \equiv \frac{1}{H} \int_0^H s dz$ is the bulk dry static energy, and L_C the latent heat of condensation.

The surface sensible heat flux is denoted by SH, $L_C P$ is the latent heat released in the boundary layer through formation of cloud water (assuming all cloud water precipitates

out), and RC stands for radiative cooling. RC is positive for cooling of the mixed layer, SH is positive for heating of the mixed layer. Since radiative cooling of the boundary layer depends on the height of the boundary-layer top, it is assumed to vary linearly with the PBL height: $RC = \gamma \cdot H$, where γ is a constant. Thus, the dry static energy equation becomes

$$\nabla_h \cdot (s_B H \mathbf{v}_{hB}) = w_E s_H - w_C s_B + \frac{SH + L_C P - \gamma H}{\rho_0} \tag{2.22}$$

The system of three equations (eqns. (2.11), (2.20) and (2.22)) can be solved analytically and leads to expressions for the three unknowns H (boundary-layer depth), w_E, (entrainment velocity) and w_C (cumulus mass flux velocity):

$$H = \frac{((SH + L_c P)/\rho_0)(q_H - q_B) - ((EVP - P)/\rho_0)(s_H - s_B)}{(\mathbf{v}_{hB} \cdot \nabla_h s_B)(q_H - q_B) - (\mathbf{v}_{hB} \cdot \nabla_h q_B)(s_H - s_B) - (q_H - q_B)(\gamma/\rho_0)} \tag{2.23}$$

$$w_E = \frac{((SH + L_c P - \gamma H)/\rho_0)(\mathbf{v}_{hB} \cdot \nabla_h q_B) - ((EVP - P)/\rho_0)(\mathbf{v}_{hB} \cdot \nabla_h s_B)}{(\mathbf{v}_{hB} \cdot \nabla_h s_B)(q_H - q_B) - (\mathbf{v}_{hB} \cdot \nabla_h q_B)(s_H - s_B)} \tag{2.24}$$

$$w_C = w_E - \nabla_h \cdot (\mathbf{v}_{hB} H) \tag{2.25}$$

This version of the model applies all precipitation in the PBL, which is a reasonable assumption in regions where rain falls from PBL clouds such as marine stratocumulus, or even shallow cumuli. In regions of deep convection, placing all precipitation in the PBL is obviously wrong. The model has been tested with monthly

mean precipitation rates from the Tropical Rain Measurement Mission (TRMM) 3B43 data set, but the results for these runs are not discussed in detail here. While of interest when studying the behavior of the model, the results of these runs turn out to be so unrealistic that we have concentrated on the non-precipitating version of the model for this thesis.

Neglecting precipitation in the model equations leads to:

$$H = \frac{(SH/\rho_0)(q_H - q_B) - (EVP/\rho_0)(s_H - s_B)}{(\mathbf{v}_{hB} \cdot \nabla_h s_B)(q_H - q_B) - (\mathbf{v}_{hB} \cdot \nabla_h q_B)(s_H - s_B) - (q_H - q_B)(\gamma/\rho_0)} \tag{2.26}$$

$$w_E = \frac{((SH - \gamma H)/\rho_0)(\mathbf{v}_{hB} \cdot \nabla_h q_B) - (EVP/\rho_0)(\mathbf{v}_{hB} \cdot \nabla_h s_B)}{(\mathbf{v}_{hB} \cdot \nabla_h s_B)(q_H - q_B) - (\mathbf{v}_{hB} \cdot \nabla_h q_B)(s_H - s_B)} \tag{2.27}$$

$$w_C = w_E - \nabla_h \cdot (\mathbf{v}_{hB} H). \tag{2.28}$$

The processes accounted for by this non-precipitating version of the model are sketched in Fig. 2.1.

From this point on, whenever the mixed-layer model (MLM) is mentioned, we mean the non-precipitating version of the mixed-layer model described in this section.

2-B: Model input data

2-B-1 Run with NCEP re-analysis data

For the runs with NCEP re-analysis data, the model domain covers the Pacific from 120° E to 80° W and from 20° S to 20° N. The input data fields are provided on a

$2.5° \text{x} 2.5°$ longitude-latitude grid (65x17 grid points). The gradients of dry static energy and water vapor are approximated using centered differences on the same grid, using one additional grid point at the edges of the domain.

The expression for the cumulus mass flux velocity w_C includes a horizontal gradient of the PBL depth H (see (2.28)). To avoid boundary layer issues, the w_C field is one grid point smaller at each boundary.

All input fields, except for precipitation, are from the monthly mean NCEP re-analysis product (ds090.2) obtained from the Scientific Computing Division's Data Support Section (DSS) at the National Center for Atmospheric Research (NCAR). Geopotential height, relative humidity and temperature are provided on pressure levels and on a $2.5° \text{x} 2.5°$ longitude-latitude grid. The surface fields (sensible heat flux, latent heat flux, net longwave flux, sea-surface temperature, 10m winds) came on a Gaussian grid (T62, even grid spacing of $1.875°$ in longitudinal direction, and uneven spacing in latitudinal direction of roughly $1.9°$) and were remapped onto a regular longitude-latitude grid with code provided by DSS. The longwave radiative heating rate used to calculate the radiative cooling of the atmosphere is provided on the 26 sigma levels of the model ($\sigma = p/p_{sfc}$, where p_{sfc} is the surface pressure), and on the Gaussian grid. Using the relationship

$$\frac{dT}{dt} = \frac{g}{c_p}\left(\frac{dF_{net}}{dp}\right), \tag{2.29}$$

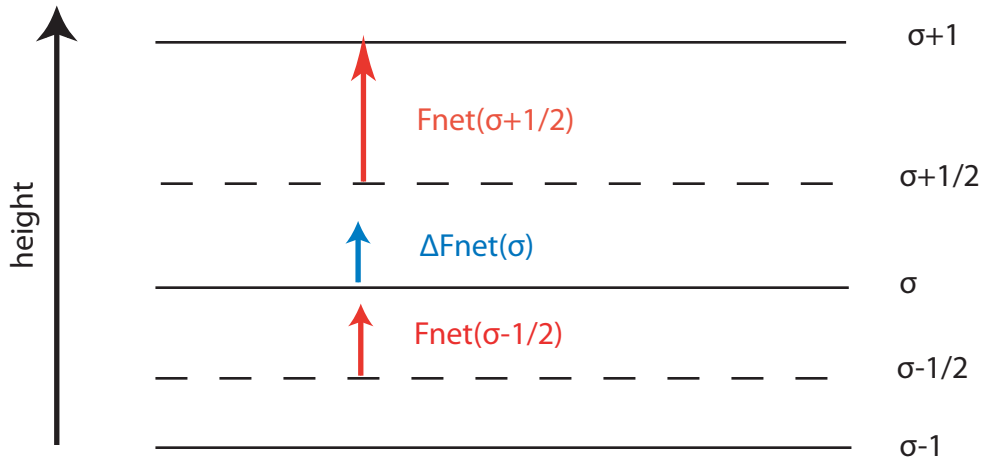

Figure 2.2: Schematic of σ levels and net longwave fluxes.

the net longwave-flux difference between the surface and the pressure at $\sigma = 0.7761$ is calculated from the longwave radiative heating rate:

$$(\Delta F_{net})_{\sigma} = (F_{net})_{\sigma+\frac{1}{2}} - (F_{net})_{\sigma-\frac{1}{2}} = -\frac{c_p}{g}\left(\frac{dT}{dt}\right)_{\sigma}\left[p\left(\sigma+\frac{1}{2}\right) - p\left(\sigma-\frac{1}{2}\right)\right]. \qquad (2.30)$$

Here, $(\Delta F_{net})_{\sigma}$ is the net longwave flux difference between the pressure levels $\sigma+\frac{1}{2}$ and $\sigma-\frac{1}{2}$. $\left(\frac{dT}{dt}\right)_{\sigma}$ is the longwave radiative heating rate on a sigma level as provided by the NCEP re-analysis. The minus sign makes sure the radiative cooling factor γ (defined below) has the correct sign. We define

$$\Delta F_{net} = \sum_{\sigma=0}^{7} (\Delta F_{net})_{\sigma} \qquad (2.31)$$

as the net longwave flux difference between the pressure at $\sigma = 0.7761$ and the surface. γ, the linear radiative cooling factor should be the longwave radiative cooling of the boundary layer per height, not per pressure, and is therefore given by

$$\gamma = \Delta F_{net}\left(\frac{-g\rho_0}{p_{\sigma = 0.7761} - p_{sfc}}\right). \tag{2.32}$$

In order to keep the system of equations simple enough to solve analytically, the radiative cooling depends only linearly on height. The choice of the factor γ is somewhat arbitrary, and a linear fit does not describe the height dependence of the radiative cooling accurately, but this simple height dependence should be preferable to a prescribed constant.

The mixed-layer dry static energy, s_B, is calculated from temperature and geopotential height on the 1000 hPa pressure surface. The bulk water vapor mixing ratio q_B is the saturation mixing ratio at sea-surface temperature and sea-level pressure.

The dry static energy in Joules at a given pressure level (here e.g. 600 hPa) is calculated as

$$s_{600} = c_p T_{600} + gGPH_{600}\ , \tag{2.33}$$

where s_{600} is the dry static energy at 600 hPa, c_p is the specific heat of air at constant pressure, T_{600} is the air temperature at 600 hPa in Kelvin, g is the gravitational acceleration and GPH_{600} is the geopotential height at 600 hPa. The water vapor mixing ratio in kg kg^{-1} at 600 hPa is calculated as follows:

$$q_{600} = 0.622 \frac{V}{600hPa - V}, \tag{2.34}$$

where V is the vapor pressure at 600 hPa in hPa:

$$V = RH_{600}\left(\frac{6.1078 \exp\left(17.2693882 \frac{(T_{600} - 273.16)}{(T_{600} - 273.16 + 237.3)}\right)}{100}\right). \tag{2.35}$$

RH_{600} is the relative humidity at 600 hPa in % as obtained from the NCEP re-analysis.

The dry static energy above the boundary-layer top increases close to linearly. Since the observed trade wind inversion height frequently lies around 800 to 850 hPa, the 850 hPa pressure level is not a safe choice for the above-boundary-layer value s_H. Instead, the dry static energy is linearly extrapolated downward from the 600 hPa and 700 hPa levels to approximately 800 hPa. The same is done for q_H.

Since stratocumulus clouds tend to precipitate little (on the order of 1 mm day^{-1} or so), considering these clouds to be part of the PBL (as is implicitly done by the

application of radiative cooling to the PBL, and not to a separate cloud layer) should be acceptable.

The model is run for the months January, April, July and October of 2001. The year is chosen to coincide with the East Pacific Investigation of Climate (EPIC, September/ October 2001). April is the month with the most apparent double-ITCZ structure, and January and July are typical test months.

2-B-2 Run with GCM output data

The output from the GCM that the MLM is compared to in Chapter 3 is remapped from the geodesic grid onto a 1.125° x1.125° longitude-latitude grid. The geodesic grid is created by subdividing an icosahedron's triangular planes multiple times and projecting the new vertices onto a sphere. Fig. 2.3 shows an icosahedron and the geodesic grid on a sphere. The MLM has been adapted to this 1.125° x1.125° grid size for the runs with GCM data input. Accordingly, the domain size is slightly different, but the fields have been plotted over the same domain as is used for the re-analysis runs. More information on

a) b)

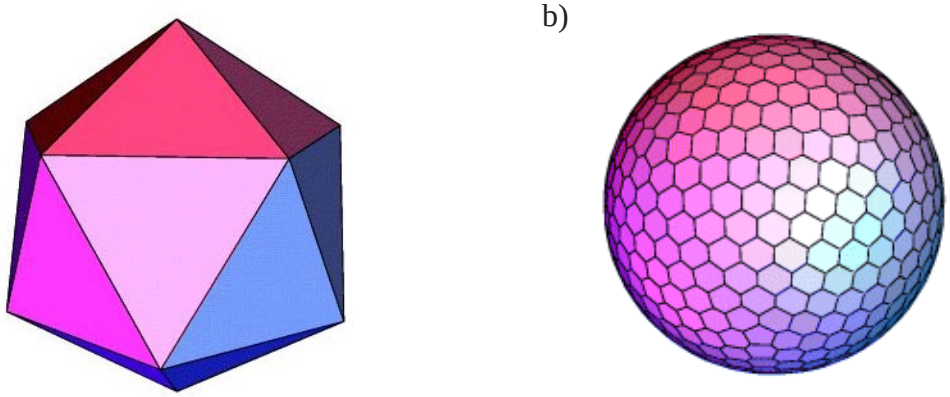

Figure 2.3: a) Icosahedron and b) geodesic grid

the GCM run and data is given in Chapter 3.

2-C: Observations

2-C-1 EPIC

During the East Pacific Investigation of Climate (EPIC), the Ronald H. Brown traveled along the 95W meridian from 12N to the Galapagos Islands (see Fig. 2.4) on the first leg of its cruise. During the first leg, a total of 124 radiosondes were launched. The majority of these launches took place near 10° N, 95° W, where the ship remained more or less stationary from September 12th through October 1st 2001.

On the second leg of the cruise, a total of 116 radiosondes were launched from the NOAA ship Ronald H. Brown between October 9th and 25th 2001. The sondes used were Vaisala RS80 sondes utilizing GPS tracking to determine the winds. The cruise track is shown in Fig. 2.5.

During the first leg of the cruise, the focus was on the temporal variation of the atmosphere, whereas the second leg explored spatial variations as well. Therefore, the data obtained during the second leg of the Ronald H. Brown's cruise is of more interest for this study.

Over approximately the same time period as the radiosonde launches during the first leg, the NSF C-130 aircraft released 181 dropsondes on fourteen days between 12° N and the Equator. Eight of the flights traveled along the 95° W meridian from about 12° N to the Equator, the others stayed further north in the ITCZ.

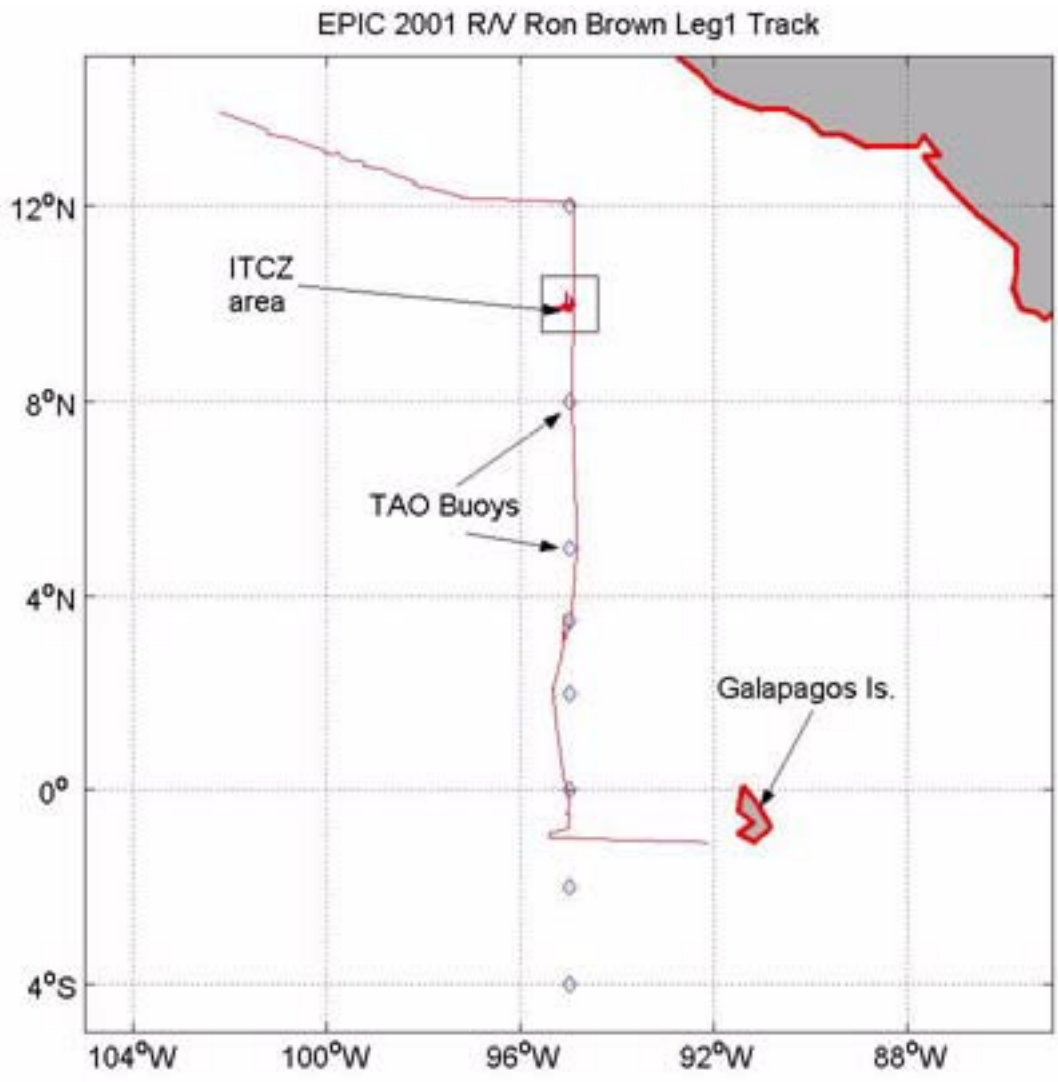

Figure 2.4: Cruise track of the Ronald H. Brown, Leg 1

2-C-2 TOGA/COARE

The Tropical Ocean Global Atmosphere/Coupled Ocean Atmosphere Response Experiment (TOGA/COARE) took place from 1 November 1992 through 28 February 1993 over the west Pacific (10° S to 10° N and 140° E to 180° E), and involved several ships and aircraft and numerous island stations.

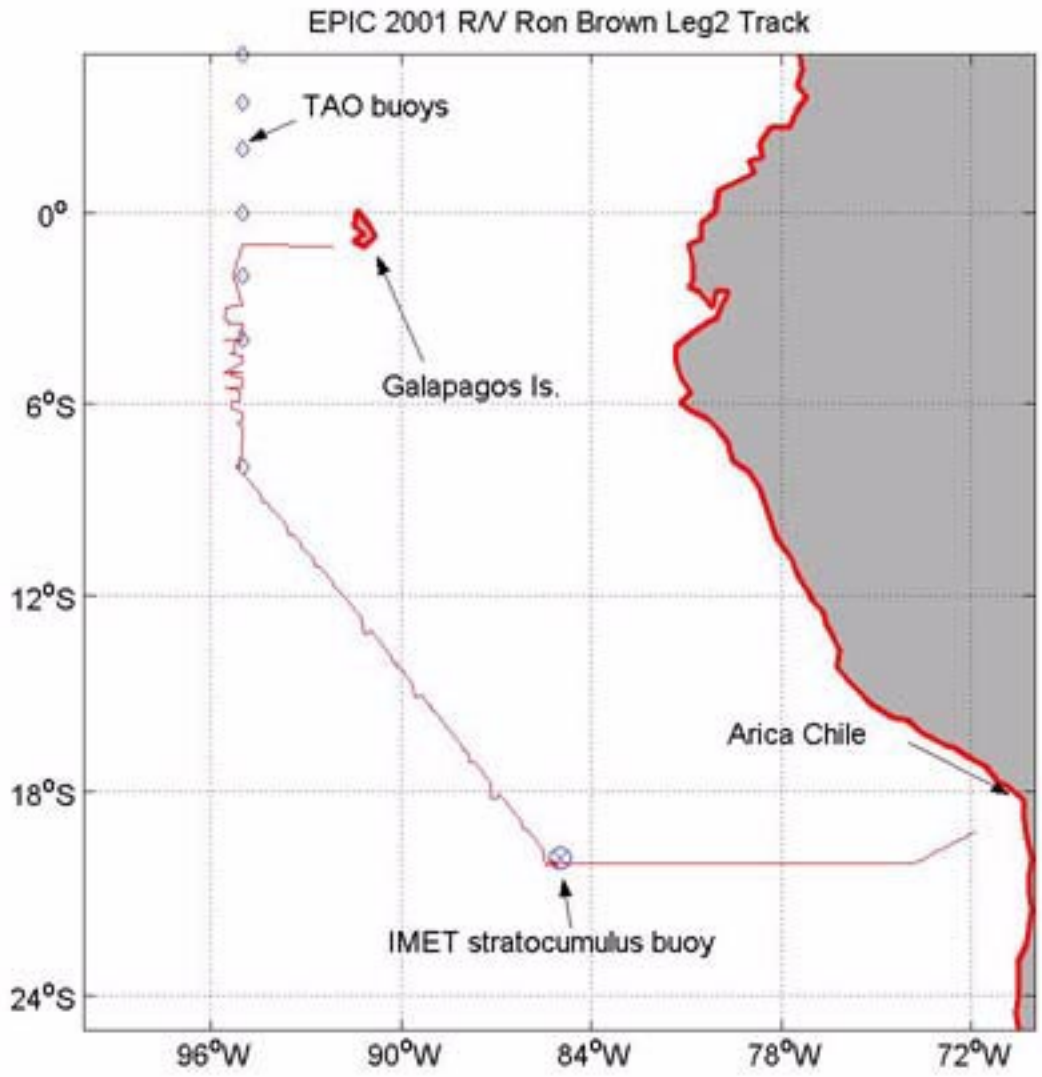

Figure 2.5: Cruise rack of the Ronald H. Brown, Leg 2

The mixed PBL was not a focus of TOGA/COARE, and there has been little evaluation of the data on this subject. Since data evaluation is not the primary objective of this study either, radiosonde data from only one of the island stations (Thursday Island at 142.2° E, 10.6° S) is used in this thesis for a general overview of the lower atmospheric conditions in the warm pool region (see Chapter 5).

2-C-3 MODIS cloud-top pressure

The Moderate Resolution Imaging Spectroradiaometer (MODIS) is one of five instruments aboard the Terra Earth Observing System (EOS) platform. Among the cloud top properties from the MODIS product is cloud-top pressure. It is inferred with a CO_2 slicing technique discussed in detail by Menzel et al. (1983) and Wylie and Menzel(1999). The cloud-height accuracy increases as the observed cloud signal (clear sky minus measured radiance) increases. Unfortunately, for clouds lower than 700 hPa, the cloud signal decreases and the CO_2 slicing technique cannot be used. Instead, the cloud-top temperature is determined from the $11-\mu m$ infrared band, assuming the cloud is optically thick, and the cloud-top pressure is assigned by comparison to the NCEP Global Data Assimilation System (GDAS) temperature profile (Platnick et al., 2003). The cloud-top pressure is provided as monthly mean or daily mean on a $1^\circ x1^\circ$ grid.

2-C-4 LITE and GLAS

Another way of measuring the PBL depth from space was explored during the Lidar In-space Technology Experiment (LITE). A three-wavelength backscatter lidar developed by the National Aeronautics and Space Administration's (NASA) Langley Research Center was mounted on a space shuttle collecting data for eleven days in September 1994. For a comprehensive overview of the mission refer to Winker et al. (1996).

The PBL top is frequently marked by a sharp gradient in aerosol concentration, which can be detected by the lidar. The PBL depth can be determined by locating the

surface and the aerosol gradient that marks the PBL top. This was done manually for 5337 points along the footprints from LITE (Mark Branson, personal communication). Unfortunately, the temporal and spatial coverage of the data were very limited, and are of little use here.

On January 26, 2003 the Ice, Cloud, and land Elevation (ICESat) satellite was launched with the Geoscience Laser Altimeter System (GLAS) instrument aboard. This instrument retrieves the PBL top in a similar manner as was done in the LITE experiment, using two lasers at wave lengths of 532 nm and 1064 nm. More information about NASA's ICESat mission can be found in Goddard Space Flight Center publication ICESat, Ice, Cloud, and land Elevation Satellite, September, 2002 (FS-2002-9-047-GSFC). In October 2003, preliminary data became available. The project is still in its beginning phase, though. More on this data can be found in Chapter 5.

Chapter 3: Comparing the GCM and the MLM

The Colorado State University General Circulation Model (CSU GCM) uses a mixed layer scheme very similar to the MLM described in Chapter 2. One might therefore expect that, given the same initial conditions, both models would produce the same monthly mean PBL depth, entrainment and cumulus mass flux velocities. As it turns out, this is not the case. The major difference between the models is that the GCM predicts the PBL properties on a very short time step, while the MLM diagnoses the PBL properties from monthly mean fields. This chapter discusses the impact of neglecting the short temporal variability in the MLM. Any weaknesses of the MLM discovered here may then be of use when interpreting the results of the MLM runs using other input data, as in Chapter 4.

3-A: The PBL in the GCM

The version of the CSU GCM used here runs on a geodesic grid with 10242 cells in the horizontal (this corresponds roughly to a 250 km grid spacing) and 17 levels of a modified σ coordinate from the surface to 1 hPa (Ringler et al. 2000). Except for radiation and convection, which are calculated hourly, the time step is 200 s. The model uses the Fowler-Randall-Rutledge microphysics (Fowler et al. 1996 a, b & c) and a modified Arakawa-Schubert scheme for convection (Pan and Randall, 1998; Ding and Randall

1998; Fowler and Randall, 2002). Radiation is included using the Harshvardhan scheme (Harshvardhan et al. 1987). Land-surface processes are parameterized with the Simple Biosphere Model Version II (SiBII; Sellers et al. 1996 a & b, Randall et al. 1996). At the lower boundary, seasonally varying SST, sea ice distribution and thickness, vegetation types, surface albedo and roughness as well as realistic topography are applied. In this run, the model uses the climatological SST for April.

The CSU GCM uses a time-dependent boundary-layer model that is otherwise very similar to the one described in Chapter 2. However, the GCM uses potential temperature instead of dry static energy for the third conservation equation. All precipitation falls through the PBL without evaporating.

We will use results from a run in which the contributions to the mass, moisture and potential temperature equations in advective form have been saved at every time step and subsequently averaged over a month. The GCM guarantees that the three variables, mass, potential temperature and water vapor mixing ratio, are truly conserved at every time step. Hence, the monthly averages of those contributing terms in all three equations are guaranteed to satisfy the monthly mean conservation equations exactly:

$$\begin{aligned}
\overline{\frac{\partial \pi}{\partial t}} &= -\overline{\nabla \cdot (\pi \mathbf{v}_{hB})} + \bar{E} - \bar{M} \\
\overline{\pi \frac{\partial}{\partial t}(q_B)} &= -\overline{(\pi \mathbf{v}_{hB} \cdot \nabla q_B)} + \overline{E(q_H - q_B)} + \overline{EVP} \\
\overline{\pi \frac{\partial}{\partial t}(\theta_B)} &= -\overline{(\pi \mathbf{v}_{hB} \cdot \nabla \theta_B)} + \overline{E(\theta_H - \theta_B)} + \overline{SH} - \overline{RC}
\end{aligned} \tag{3.1}$$

The GCM uses pressure thickness $\pi = \Delta p / g$ as a measure of the PBL mass. $E = w_E \rho$ and $M = w_C \rho$ are the entrainment mass flux and the cumulus mass flux respectively. In contrast to the set of equations (3.2), (3.1) includes all temporal covariances for the transport terms, the entrainment terms and the time-rate-of-change terms. The GCM also has a varying density.

This is an important difference from the MLM, in which we *assume* that the monthly mean variables approximately satisfy the conservation equations:

$$\begin{aligned} 0 &= -\rho_0 \nabla_h \cdot (\overline{H}\,\overline{\mathbf{v}_{hB}}) + \rho_0 \overline{w_E} - \rho_0 \overline{w_C} \\ 0 &= -\rho_0 \nabla_h \cdot (\overline{H}\,\overline{q_B}\,\overline{\mathbf{v}_{hB}}) + \rho_0 \overline{w_E}\,\overline{q_H} - \rho_0 \overline{w_C}\,\overline{q_B} + \overline{EVP} \\ 0 &= -\rho_0 \nabla_h \cdot (\overline{H}\,\overline{s_B}\,\overline{\mathbf{v}_{hB}}) + \rho_0 \overline{w_E}\,\overline{s_H} - \rho_0 \overline{w_C}\,\overline{s_B} + (\overline{SH} - \bar{\gamma}\,\overline{H}) \end{aligned} \tag{3.2}$$

As an example, compare the entrainment terms of the moisture equation: We see that in the GCM, the moisture entrainment is calculated at every time step and the complete term then averaged over the month: $\overline{\rho w_E (q_H - q_B)}$. In the MLM, the entrainment velocity and the water vapor mixing ratios are first averaged over the month, then the moisture entrainment is calculated: $\rho_0 \overline{w_E}\,\overline{q_H} - \rho_0 \overline{w_C}\,\overline{q_B}$. This way of calculating the terms does not account for temporal covariances, as discussed below, and so may be too simplistic to describe reality.

Fig. 3.1 to Fig. 3.16 show the monthly mean fields of the GCM run for a climatological April.

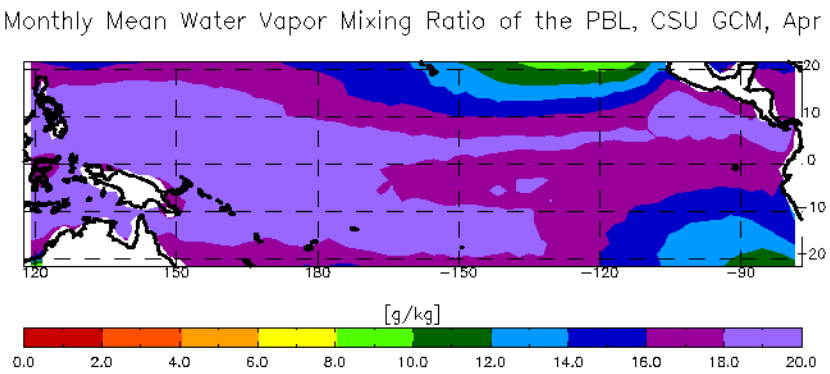

Figure 3.1: Monthly mean water vapor mixing ratio of the mixed PBL

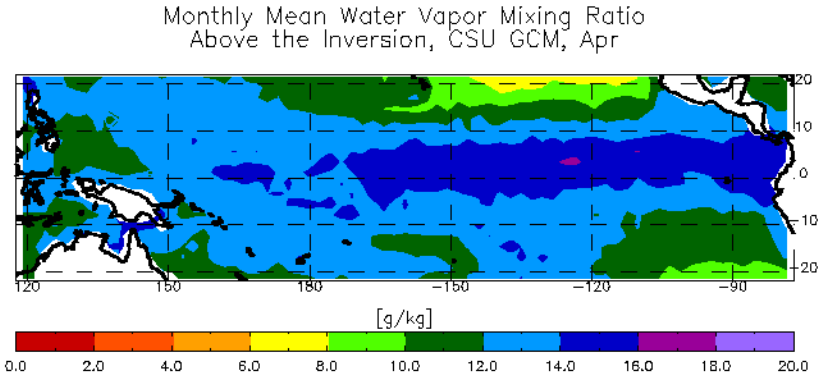

Figure 3.2: Monthly mean water vapor mixing ratio just above the PBL top

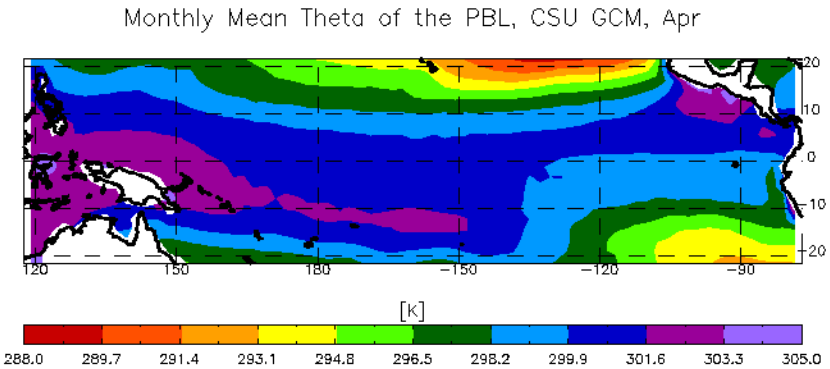

Figure 3.3: Monthly mean potential temperature of the mixed PBL

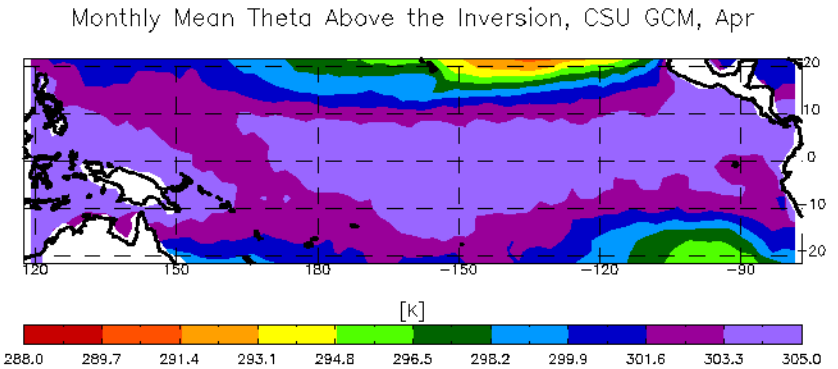

Figure 3.4: Monthly mean potential temperature just above the PBL top

The moisture and potential temperature fields as shown in Fig. 3.1 through Fig. 3.4 show moist, warm air over the west Pacific and in the equatorial region in the central and east Pacific. The air becomes drier and cooler towards the poles, both in the mixed layer and above it. It is particularly cool and dry off the Chilean and Californian coasts, as would be expected in regions of subsidence over the cold ocean. The average value for the water vapor mixing ratio above the PBL top lies around 13 $g\,kg^{-1}$. Measurements (e.g. radiosonde profiles) suggest that this value should be in the single digits. The domain averaged water vapor mixing ratio jump over the PBL top is only about 4.2 $g\,kg^{-1}$, and the domain averaged potential temperature jump about 3 K.

The surface evaporation (Fig. 3.5) has a pronounced maximum of about 10 mm/ day just off the Mexican coast. The evaporation is particularly low along the Chilean coast and the cold tongue (~3 $mm\,day^{-1}$). Over the rest of the domain it lies roughly between 4 and 7 mm/day with larger values in the central north Pacific and along the SPCZ, lower values in the north-west and south-east of the domain.

The monthly mean surface sensible heat flux (Fig. 3.6) is rather small over most of the domain, ranging between -10 $W\,m^{-2}$ and 10 $W\,m^{-2}$. It is negative in large portions of the domain, including the west and south-central part of the domain, as well as along the Equator from the date line to the American coasts and along the coasts to 20° N and 20° S. The sensible heat flux is largest in the central Pacific around 20° N with values up to 50 $W\,m^{-2}$.

The radiative cooling (Fig. 3.7) is strongest (~60 $W\ m^{-2}$) in the south-east quarter of the domain where we would expect extensive stratus decks, and it is smallest (~10 $W\ m^{-2}$) in regions where we would expect deep convection: the warm pool, the SPCZ and off the Mexican coast. When divided by the depth of the PBL to calculate the radiative cooling factor γ (Fig. 3.8), the field retains its maximum in the eastern subtropical Pacific, but the center of the warm pool shows up as another maximum (~0.06 $W\ m^{-3}$). This is due to the low PBL depth over the warm pool. The rest of the domain has a relatively uniform radiative cooling factor of 2 to 3 $W\ m^{-3}$.

The only significant stratiform rain, as classified by the GCM's precipitation scheme, (Fig. 3.10) falls along 5° N from 150° W to the American coast and around the Hawaiian Islands with maximum values of about 7 mm/day. The majority of rain falls from convective systems in the warm pool, along the south Pacific convergence zone (SPCZ) and off the Mexican coast and, to a lesser amount, along the ITCZ. It should be noted that the SPCZ is oriented almost parallel to the Equator, with only a small tilt towards the south. Nature does show a tendency towards a double ITCZ in the northern spring, but the SPCZ's orientation may also be due, at least in part, to a tendency in the GCM to produce an unrealistic double ITCZ.

The incidence of PBL stratus clouds (Fig. 3.11) as recognized by the GCM is high in the north-east and south-east parts of the domain, as well as over the cold tongue. The incidence is somewhat lower along 10° S in this area. There is a minimum off the Mexican

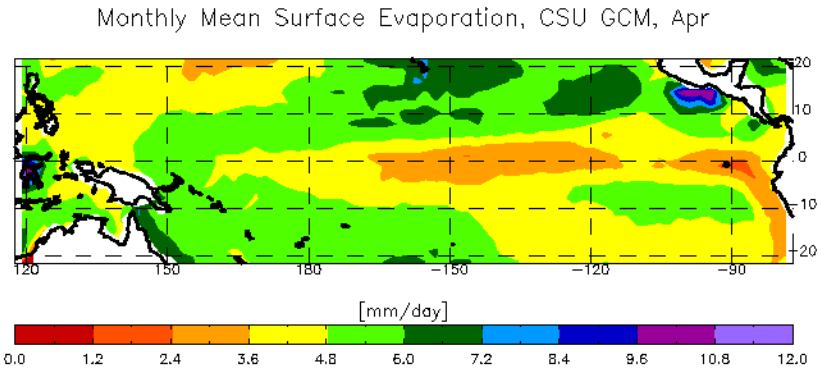

Figure 3.5: Monthly mean surface evaporation plus dry convective adjustment correction term and a hole fill correction term. The last two terms are small compared to the evaporation.

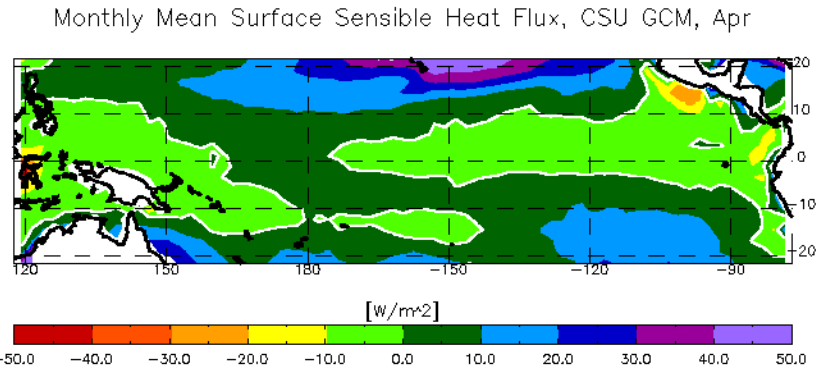

Figure 3.6: Monthly mean surface sensible heat flux plus dry convective adjustment correction term. The correction term is small compared to the sensible heat flux.

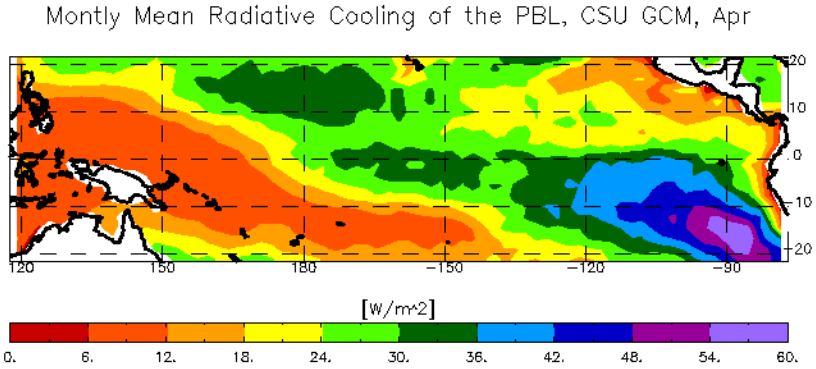

Figure 3.7: Monthly mean radiative cooling applied to the PBL

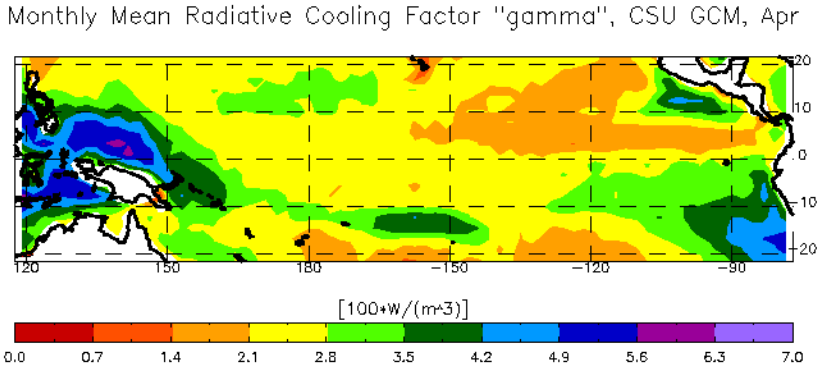

Figure 3.8: Radiative cooling factor γ calculated from the monthly mean radiative cooling and monthly mean PBL depth as given by the GCM.

coast where the convective rain has a maximum. The incidence of PBL stratus clouds in the western half of the domain is small. The areas of stratiform clouds do not match up very well with the regions of stratiform precipitation. As mentioned before, all precipitation in the GCM originates above the PBL. Hence, it should not be surprising, that the incidence of PBL clouds does not match the (above PBL) stratiform precipitation.

The divergence of the 10 m wind shows convergence in the ITCZ, SPCZ and in part of the warm pool area. The strongest divergence occurs off the Chilean coast. Over most of the domain, the divergence ranges between -1 and $1\times10^{-5}s^{-1}$.

The cumulus mass flux (Fig. 3.13) very closely follows the structure of the convective precipitation with maximum velocities around 1 $\mathrm{cm\,s^{-1}}$. Convective precipitation and cumulus mass flux velocity scale almost linearly with 10 mm/day precipitation corresponding to 1 $\mathrm{cm\,s^{-1}}$ cumulus mass flux velocity. A close relationship between those two properties should be expected, of course.

The entrainment velocity (Fig. 3.14) has maxima around 2.5 $\mathrm{cm\,s^{-1}}$ in the stratocumulus regions: off the south American and Californian coasts. In the warm pool region and along parts of the SPCZ, the entrainment velocity is close to zero. Right along the coasts, it is negative (~ -0.4 $\mathrm{cm\,s^{-1}}$), resulting in a net upward velocity. This means, as the PBL collapses, the PBL top “falls” through the air, and boundary layer air is crossing the PBL top into the free atmosphere. Since the GCM uses an upstream scheme, the air

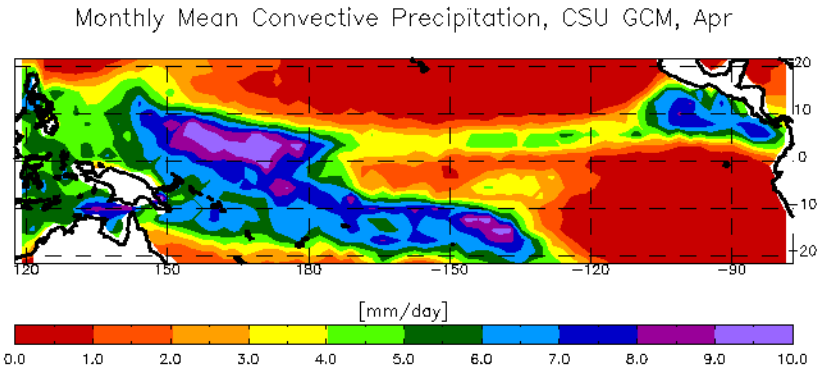

Figure 3.9: Monthly mean convective precipitation

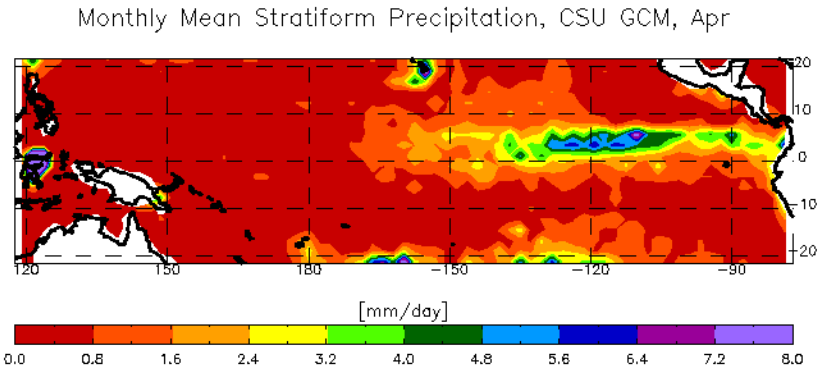

Figure 3.10: Monthly mean stratiform precipitation

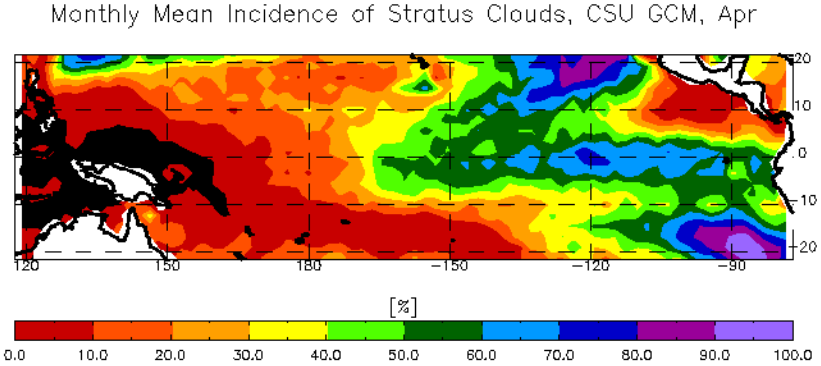

Figure 3.11: Monthly mean incidence of PBL stratus clouds in %. Black indicates areas of 0% incidence.

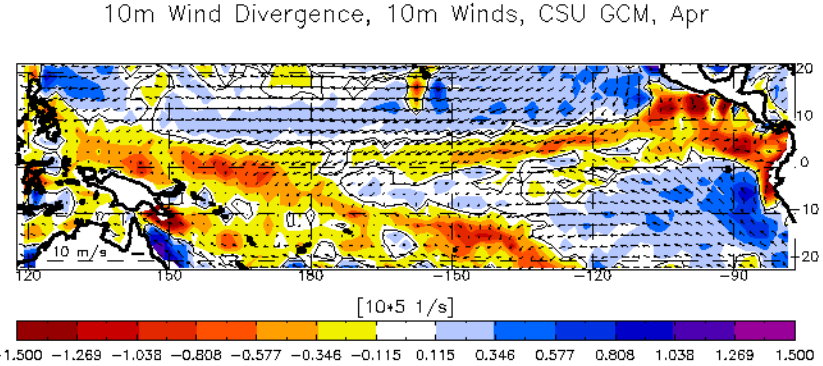

Figure 3.12: Monthly mean 10 m wind divergence and 10 m winds. Zero contour in black.

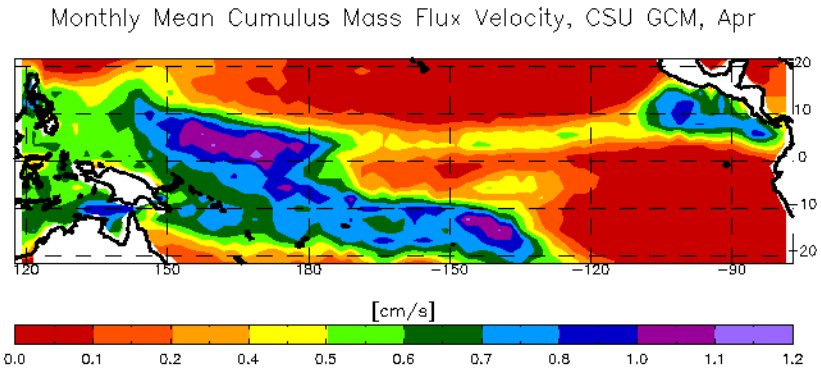

Figure 3.13: Monthly mean cumulus mass flux velocity

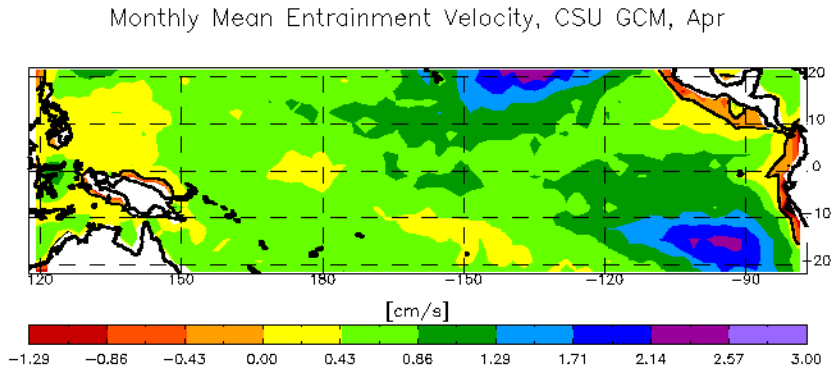

Figure 3.14: Monthly mean entrainment velocity. Zero contour in white.

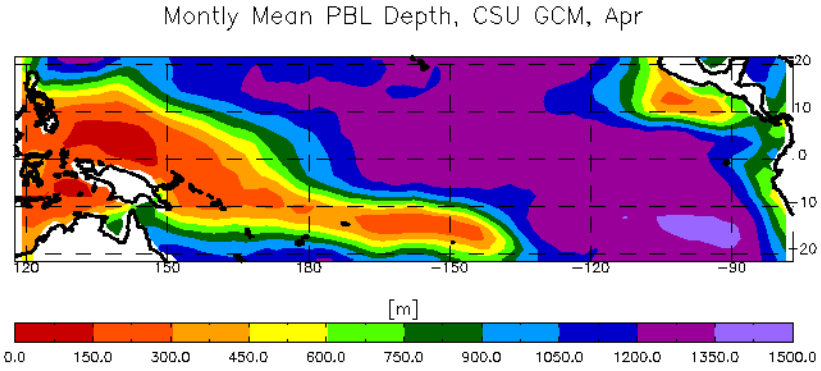

Figure 3.15: Monthly mean PBL depth

rising out of the PBL has PBL properties. The MLM does not use the upstream scheme. Hence, a negative entrainment velocity in the MLM would transport air out of the PBL that has the properties of above-PBL air. Since this case is non-physical anyway, and indicates that the MLM does not work properly in this particular region, we are not too concerned with the characteristics of the air transported by such negative entrainment. The entrainment velocity in the GCM should never be negative either. A short discussion of a possible explanation for this behavior follows in Chapter (4-C).

The monthly mean PBL depth (Fig. 3.16) is low over the warm pool and along the SPCZ, as well as along the South American coast and off Mexico. Since all rain falls from above the PBL, the PBL corresponds most closely to the subcloud layer in those regions. The central and south-east Pacific area has a uniform PBL depth of about 1200 m. There is no indication of the ITCZ in the PBL depth field.

3-A-1 Summary

Two fields that don't agree with general observations very well are the above-PBL-top water vapor mixing ratio (too moist), and the surface sensible heat flux, which is negative over large areas of the domain. The GCM does produce a very nice and smooth PBL depth of reasonable magnitude and structure. It is a little surprising that, even though most fields clearly show a signature of the ITCZ, there is no indication of the ITCZ in the PBL depth. Although the GCM is run for April, a month in which a southern hemispheric ITCZ can often be observed in the eastern Pacific, there is no indication of a double ITCZ east of 120° W in any of the fields. However, the SPCZ is rather parallel to the Equator.

The entrainment velocity is largest in the stratocumulus regions and small in deep convective regions. Unfortunately, it is negative close to the continental coasts.

Overall, the GCM seems to do a good job of describing the PBL over the tropical Pacific. This is fortunate, as, lacking large coverage observational data, we want to use the GCM output for comparison with the more simplified MLM.

The monthly mean of the GCM fields for sensible heat, evaporation, radiative cooling, water vapor mixing ratio and dry static energy calculated from the GCM potential temperature will be used as input for the MLM in the next section. These fields will be referred to as 'GCM data input' for the MLM run. They are not, however, input for the GCM run, but are output from the GCM run.

3-B: MLM results with GCM data input

Fig. 3.16 to Fig. 3.19 show the PBL depth, entrainment and cumulus mass flux velocities of the MLM run with the monthly mean GCM fields for sensible heat, evaporation, radiative cooling, water vapor mixing ratio and dry static energy calculated

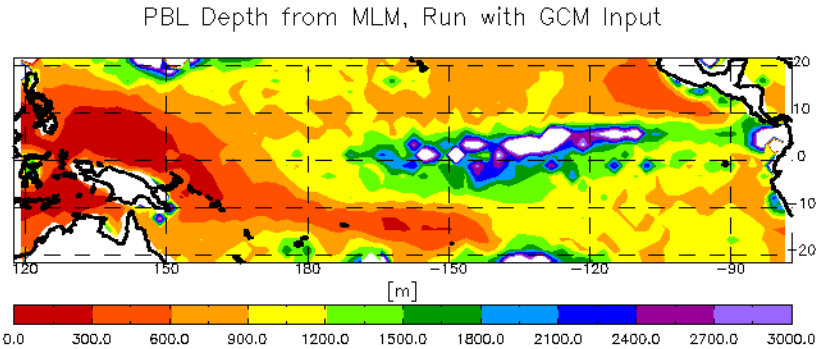

Figure 3.16: PBL depth calculated by MLM from GCM input. White areas (other than continents) indicate above-scale values.

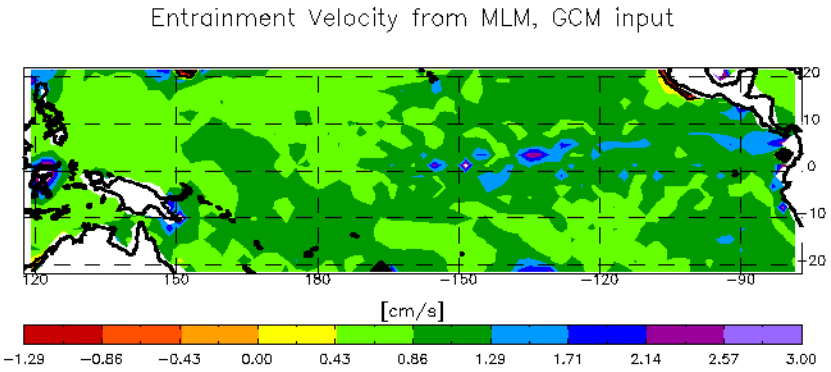

Figure 3.17: Entrainment velocity calculated by MLM from GCM input. White areas (other than continents) indicate above-scale values. Same scale as in Fig. 3.14.

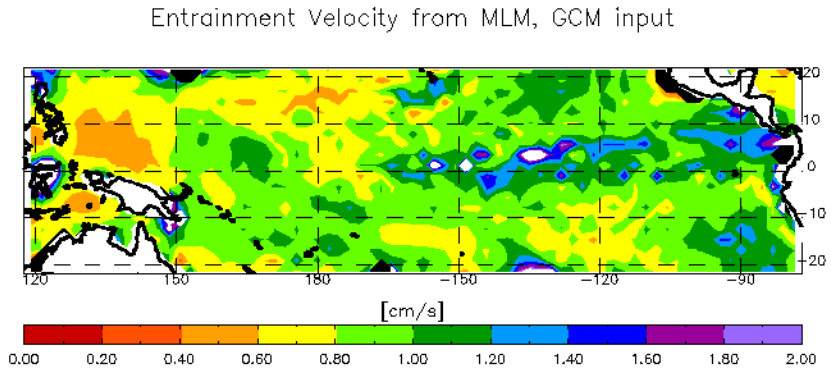

Figure 3.18: Same entrainment velocity as in Fig. 3.17, but on a different scale to show more detail.

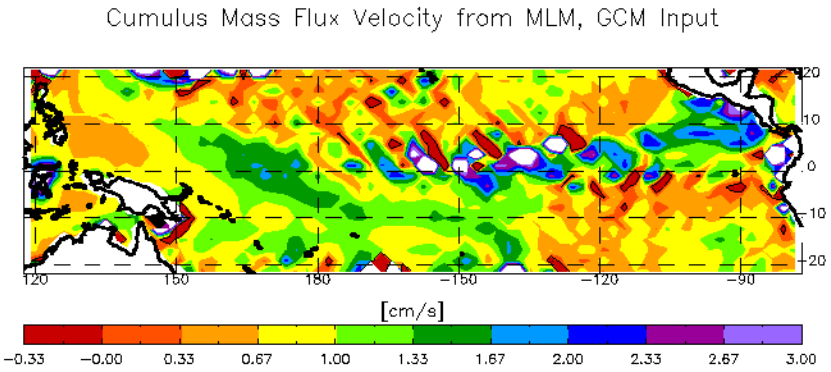

Figure 3.19: Cumulus massflux as calculated by the MLM from GCM input fields. White areas (other than continents) indicate above-scale values.

from the GCM potential temperature.

Comparing the PBL depth as predicted by the GCM (Fig. 3.15) to the PBL depth calculated by the MLM (Fig. 3.16) reveals some important differences. Right along the American coast line, the PBL depth calculated by the MLM has several local maxima. In the central and south-east Pacific, the PBL depth lies around 900 m rather than the 1200 m predicted by the GCM. Most importantly, the MLM produces a pronounced ridge along the ITCZ that is absent in the GCM.

The MLM produces an all positive entrainment velocity with a maximum along the ITCZ and minima in the west and north-west areas of the domain. The magnitude of the entrainment in the MLM is more uniform over the domain than that of the GCM, as is illustrated in Fig. 3.17. The entrainment velocity in the MLM ranges mostly between 0.4 and 1.3 $\mathrm{cm\,s^{-1}}$, compared to a range of -0.8 to 2.5 $\mathrm{cm\,s^{-1}}$ in the GCM. The spatial distribution of maxima and minima has not changed much (compare Fig. 3.14 to Fig. 3.18), with the exception of large entrainment velocities along the ITCZ in the MLM coincident with large PBL depths in the MLM. It should be noted that the radiative cooling used to calculate the entrainment velocity in the MLM depends linearly on the PBL depth. A deeper PBL leads to stronger radiative cooling, which in turn leads to stronger entrainment. This relationship is consistent with the theory that radiative cooling at the top of the PBL drives more vigorous turbulence in the PBL, which in turn enhances entrainment and deepens the PBL. Building this linear dependence into the model equations was essential for the MLM to produce positive entrainment velocities.

Most, but not all, of the structure in the cumulus mass flux velocity plot (Fig. 3.13) from the GCM has been lost in the MLM (Fig. 3.19). The cumulus mass flux velocity is largest along the ITCZ and off the coast of Mexico, with a secondary maxima along the SPCZ and in the warm pool. The maximum values are approximately double those of the GCM cumulus mass flux velocity (3 $\mathrm{cm\,s^{-1}}$ vs. 1.5 $\mathrm{cm\,s^{-1}}$). While in the GCM, areas without convective precipitation correspond to areas without cumulus mass flux, this is not the case in the MLM. Here, the cumulus mass flux is small, but positive in areas without convective precipitation. This may be interpreted to mean that shallow convection without significant precipitation is occurring. The noise, including the small areas of negative cumulus mass flux velocities in Fig. 3.19, are presumably a result of the finite differencing scheme used to calculate the cumulus mass flux velocity in the MLM. As discussed in Chapter 2, the cumulus mass flux velocity is calculated last from the mass conservation equation, using the PBL depth and entrainment velocity that were just diagnosed:

$$w_C = w_E - \nabla_h \cdot (\mathbf{v}_{hB} H) \tag{3.3}$$

The horizontal gradient is approximated by a centered difference:

$$w_C(i,j) = w_E(i,j) - \frac{u_B(i+1,j)H(i+1,j) - u_B(i-1,j)H(i-1,j)}{2\Delta x(j)} - \frac{v_B(i,j+1)H(i,j+1) - v_B(i,j-1)H(i,j-1)}{2\Delta y} \tag{3.4}$$

w_C is calculated on a domain one grid point smaller at each boundary to avoid boundary conditions. A very steep gradient in PBL depth (as along the ITCZ, for example) in combination with a low entrainment velocity will therefore lead to negative cumulus mass flux velocities. Also, any small-scale variability in the PBL depth will lead to a highly varying ("noisy") mass flux velocity.

3-B-1 Summary

One of the MLM's improvements over the GCM's output is the all-positive entrainment velocity. This is due to the introduction of a linear dependence of radiative cooling on PBL depth in the MLM. Prior to the introduction of this functionality, both PBL depth and entrainment velocity were negative over parts of the domain.

Surprisingly, the MLM's PBL depth agrees best with the GCM's PBL depth in the warm pool region. Overall, the MLM tends to underestimate the PBL depth over most of the domain, the exception being the ITCZ, where the PBL depth is extremely large. The weakest field out of the MLM output is the cumulus mass flux velocity field. It is strongly influenced by noise from the finite-difference scheme. On the positive side, the cumulus mass flux velocity is negative over only very small regions for the MLM run with GCM data input. As discussed later, this is not always the case when the MLM is run with NCEP re-analysis input.

The next section will explore the influence of the steady state assumption made in the MLM on the differences between the PBL properties (depth, entrainment and cumulus

mass flux velocity) of the GCM run and the MLM run with GCM data input.

3-C: Sensitivity of the MLM to the steady state assumption

The MLM from Chapter 2 is based on the assumption that the time-rate-of-change terms disappear, and that all covariances are zero. It replaces all variables in the three conservation equations by monthly means and assumes steady state. Comparison with the GCM gives us a chance to assess how good these assumptions are. As Fig. 3.16 to Fig. 3.19 show, the MLM does not perform all that well when applied to the monthly mean GCM data. This section will further explore which assumptions and simplifications are primarily responsible for these differences.

The residuals of the full monthly mean terms as they appear in equation (3.1) and the corresponding terms calculated from time-averaged variables have been given names (see Table (3.1)) and, when included in the PBL model equations as corrective constants, reproduce the 'perfect' set of equations (3.1):

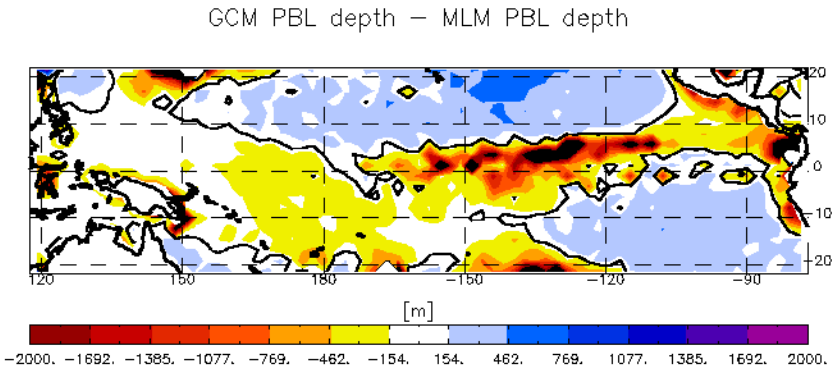

Figure 3.20: Difference plot: GCM PBL depth minus MLM PBL depth. Black indicates areas of below-scale values.

$$
\begin{aligned}
m1 &= -\nabla\cdot(\bar{\pi}\overline{\mathbf{v}_{hB}}) - m2 + \bar{E} - \bar{M} \\
q1 &= -(\bar{\pi}\overline{\mathbf{v}_{hB}}\cdot\nabla\overline{q_B}) - q2 + \bar{E}(\overline{q_H} - \overline{q_B}) + q3 + \overline{EVP} \\
\theta 1 &= -(\bar{\pi}\overline{\mathbf{v}_{hB}}\cdot\nabla\overline{\theta_B}) - \theta 2 + \bar{E}(\overline{\theta_H} - \overline{\theta_B}) + \theta 3 + \overline{SH} - \overline{RC}
\end{aligned}
\tag{3.5}
$$

Table 3.1: Correcti ve terms: covariances and time - rate - of - change terms

		direct effect if term > 0	Comments
$m1$	$\overline{\frac{\partial\pi}{\partial t}}$	increases H	disappears for a long term average
$m2$	$\overline{\nabla\cdot(\pi\mathbf{v}_{hB})} - \nabla\cdot(\bar{\pi}\overline{\mathbf{v}_{hB}})$	reduces H	small
$q1$	$\overline{\pi\frac{\partial}{\partial t}(q_B)}$	moistens PBL	$\approx \overline{\pi'\left(\frac{\partial q_B}{\partial t}\right)'}$, small
$q2$	$\overline{(\pi\mathbf{v}_{hB}\cdot\nabla q_B)} - (\bar{\pi}\overline{\mathbf{v}_{hB}}\cdot\overline{\nabla q_B})$	dries PBL	
$q3$	$\overline{\bar{E}(q_H - q_B)} - \bar{E}(\overline{q_H} - \overline{q_B})$	moistens PBL	
$\theta 1$	$\overline{\pi\frac{\partial}{\partial t}(\theta_B)}$	warms PBL	$\approx \overline{\pi'\left(\frac{\partial \theta_B}{\partial t}\right)'}$, small
$\theta 2$	$\overline{(\pi\mathbf{v}_{hB}\cdot\nabla\theta_B)} - (\bar{\pi}\overline{\mathbf{v}_{hB}}\cdot\overline{\nabla\theta_B})$	cools PBL	
$\theta 3$	$\overline{\bar{E}(\theta_H - \theta_B)} - \bar{E}(\overline{\theta_H} - \overline{\theta_B})$	warms PBL	

By setting the residual terms to zero, singly or in combination, we can test the sensitivity of the MLM to those terms. Neglecting all terms leads to a low PBL depth in

regions where little or no convection is expected, and to an excessively deep PBL in regions of convection (Fig. 3.16), as described in the previous section. Fig. 3.20 is a difference plot of GCM and MLM PBL depths.

Looking at the individual terms that contribute to this result, we find that the terms from the mass equation, $m1$ and $m2$, do not contribute much (on the order of meters) and can be neglected. The time-rate-of-change terms $q1$ and $\theta 1$ are completely neglected in the MLM. Using Reynolds averaging, it becomes more apparent that neglecting these terms really corresponds to a combination of two assumptions.

$$q1 = \bar{\pi}\overline{\frac{\partial q_B}{\partial t}} + \overline{\pi'\left(\frac{\partial q_B}{\partial t}\right)'} \tag{3.6}$$

$$\theta 1 = \bar{\pi}\overline{\frac{\partial \theta_B}{\partial t}} + \overline{\pi'\left(\frac{\partial \theta_B}{\partial t}\right)'} \tag{3.7}$$

We assume that the time-rates-of-change of q_B and s_B are small in the monthly mean *and* that the covariance of PBL depth π and the time-rate-of-change is small. In fact, the covariance terms dominate the expressions for $\theta 1$ and $q1$. Knowing that the PBL depth has a well developed diurnal cycle, especially over land, is an indication that the covariances are probably not negligible.

As it turns out, when both $q1$ and $\theta 1$ are neglected in the MLM, their effects on the PBL depth tend to cancel each other in most areas of the model domain. The most

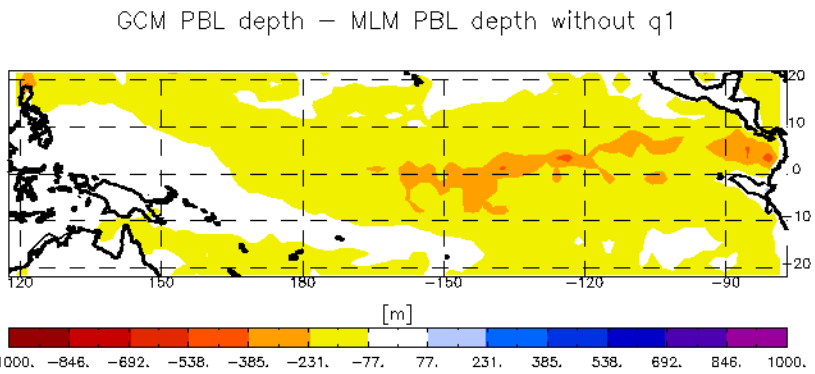

Figure 3.21: Difference plot of GCM PBL depth minus MLM PBL from model equations including all corrective terms except $q1$.

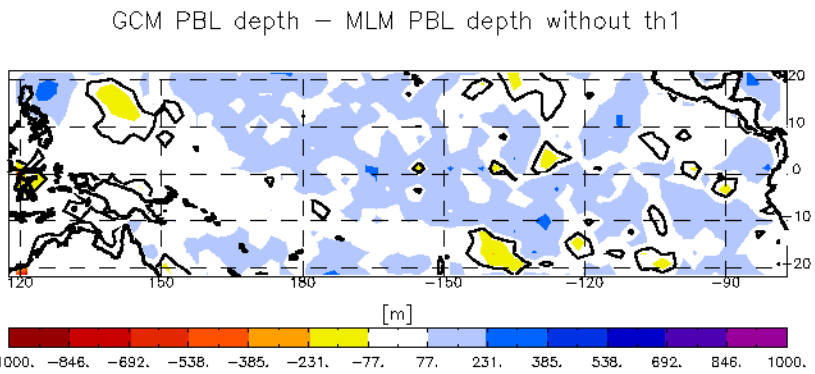

Figure 3.22: Difference plot of GCM PBL depth minus MLM PBL depth from model equations including all corrective terms except $\theta 1$.

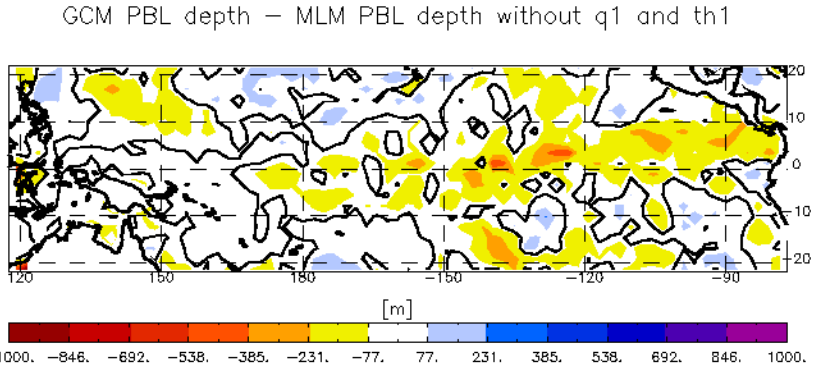

Figure 3.23: Difference plot of GCM PBL depth minus MLM PBL depth from model equations including all corrective terms except $\theta 1$ and $q1$.

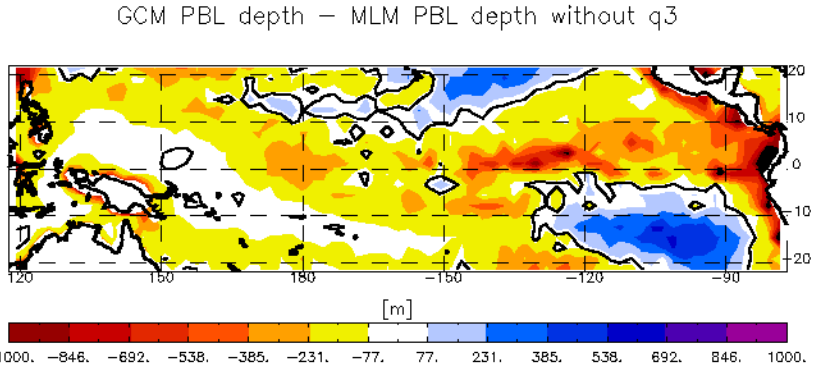

Figure 3.24: Difference plot of GCM PBL depth minus MLM PBL depth from model equations including all corrective terms except $q3$. Black indicates areas of below-scale values. The black solid line is the zero contour. Notice: Scale has changed.

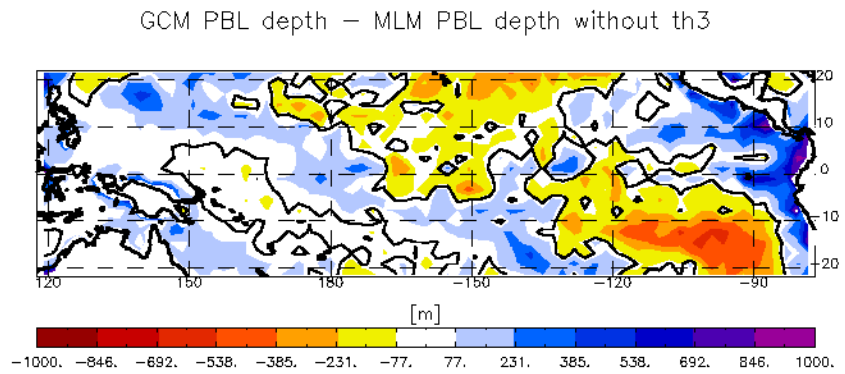

Figure 3.25: Difference plot of GCM PBL depth minus MLM PBL depth from model equations including all corrective terms except $\theta 3$. The black solid line is the zero contour. White along the ITCZ indicates above scale values. Notice: Scale has changed.

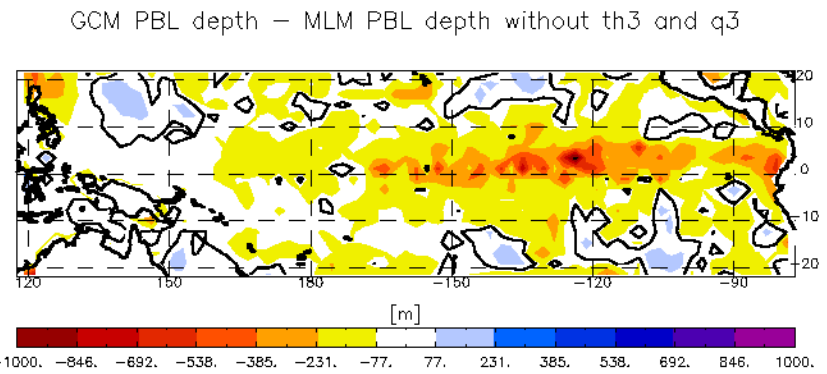

Figure 3.26: Difference plot of GCM PBL depth minus MLM PBL depth from model equations including all corrective terms except $\theta 3$ and $q3$. The black solid line is the zero contour.

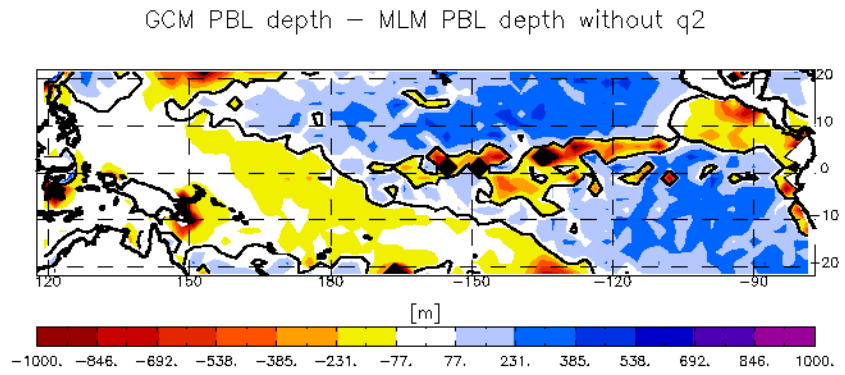

Figure 3.27: Difference plot of GCM PBL depth minus MLM PBL depth from model equations including all corrective terms except $q2$. Black indicates areas of below-scale values. The black solid line is the zero contour.

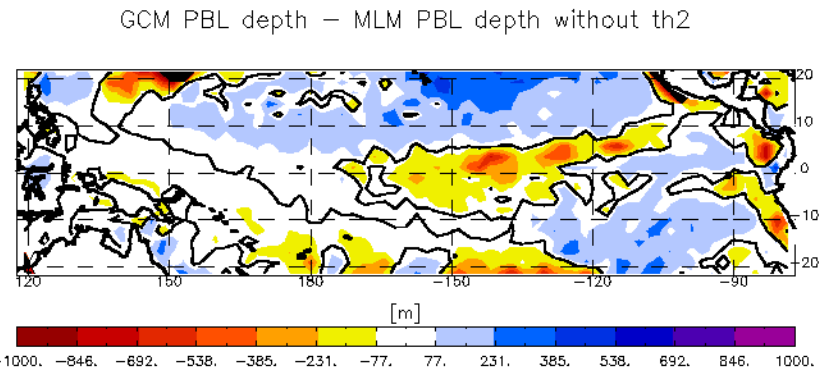

Figure 3.28: Difference plot of GCM PBL depth minus MLM PBL depth from model equations including all corrective terms except $\theta 2$. Black indicates areas of below-scale values. The black solid line is the zero contour.

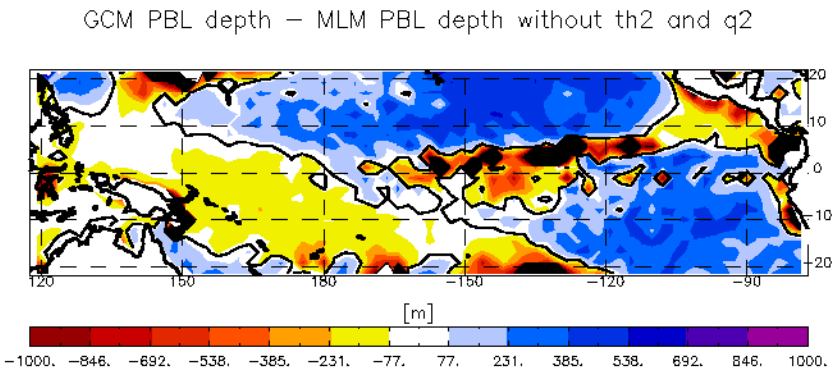

Figure 3.29: Difference plot of GCM PBL depth minus MLM PBL depth from model equations including all corrective terms except $q2$ and $\theta 2$. Black indicates areas of below-scale values. The black solid line is the zero contour.

notable exception is the ITCZ, where neglecting the both of the terms leads to a deepening of the PBL on the order of several hundred meters (Fig. 3.21 to Fig. 3.23). This suggests a high temporal variability in this region.

Similarly, the effect on the PBL depth of neglecting terms $q3$ and $\theta 3$ tend to cancel each other (Fig. 3.26), with a net effect of deepening the PBL by about 100 m over most of the domain, and strongly deepening the PBL along the ITCZ. However, the separate contributions from $q3$ and $\theta 3$ are very large, if of opposite sign (Fig. 3.24 and Fig. 3.25). $q3$ is negative over most of the domain, and positive in the stratocumulus regions, $\theta 3$ positive most of the domain and negative in the stratocumulus regions. The exceptions are the warm pool and the SPCZ, where both terms are close to zero. This means that larger than normal entrainment fluxes coincide with smaller than normal jumps of moisture and potential temperature across the top of the PBL in the stratocumulus regions, and larger than normal entrainment fluxes coinciding with larger than normal jumps of moisture and potential temperature over the rest of the domain, in particular over

and near the continents.

In Fig. 3.30 a) and b), the terms $q3$ and $\theta 3$ are plotted against the monthly mean entrainment velocity for all ocean grid points. The figures show a linear relationship between the covariances and the monthly mean entrainment velocity. In the GCM's entrainment parameterization, a small (large) PBL top jump in θ favors large (small) entrainment. It is harder, so to speak, to entrain air through a very stable PBL top marked by a large PBL top jump. In Fig. 3.30, large entrainment coincides with large positive $q3$ and large negative $\theta 3$, small entrainment coincides with large negative $q3$ and small negative $\theta 3$. This illustrates the fact that the terms $\overline{w_E(q_H - q_B)}$ and $\overline{w_E(\theta_H - \theta_B)}$ vary less over the domain than $\overline{w_E}(\overline{\theta_H} - \overline{\theta_B})$ and $\overline{w_E}(\overline{q_H} - \overline{q_B})$. A theory as to why this is the case is as follows:

In the stratocumulus regime, the general setup of the circulation, consistent with

a) b)

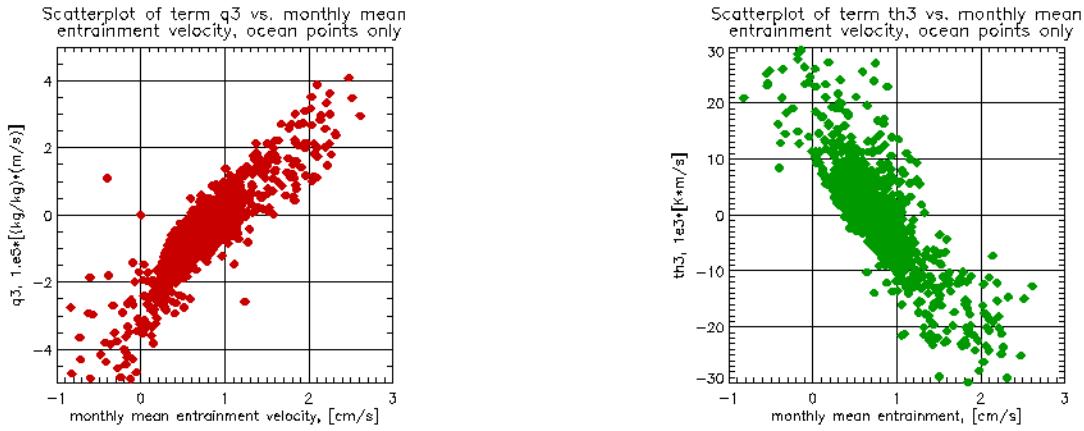

Figure 3.30: Scatterplots of a) $q3$ vs. the monthly mean entrainment velocity and b) $\theta 3$ vs. the monthly mean entrainment velocity, only grid points over the ocean are included

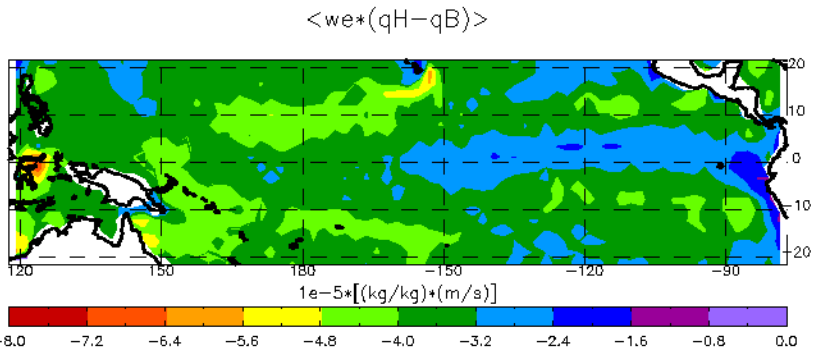

Figure 3.31: $\overline{w_E(q_H - q_B)}$

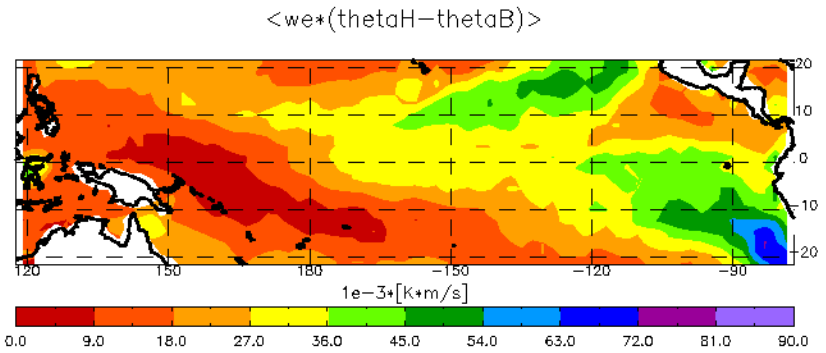

Figure 3.32: $\overline{w_E(\theta_H - \theta_B)}$

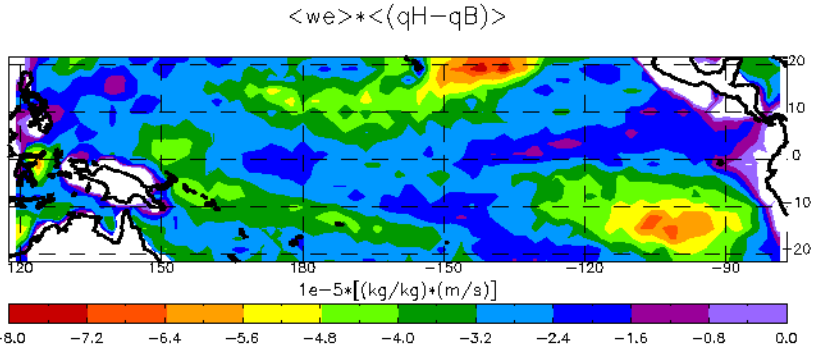

Figure 3.33: $\overline{w_E}(\overline{q_H} - \overline{q_B})$

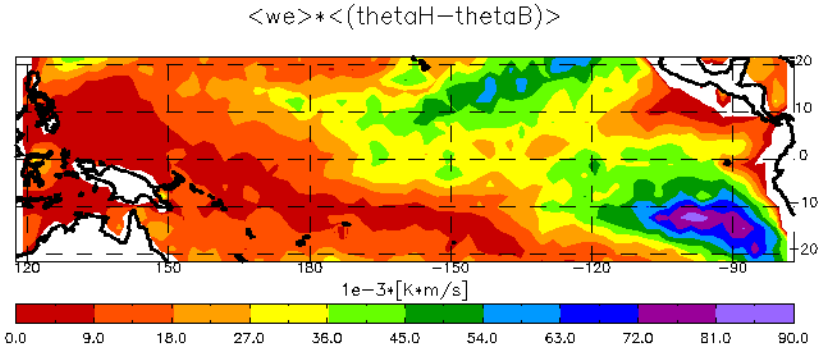

Figure 3.34: $\overline{w_E}(\overline{\theta_H} - \overline{\theta_B})$

the monthly mean fields, is such that large entrainment through a PBL top with large jumps in potential temperature and moisture is balanced by strong divergence in the PBL. The covariances in this region act to restore balance in this system: when the jumps in q and θ are larger than average, smaller-than-average entrainment is sufficient to supply the PBL with sufficient dry and warm air to maintain balance. When the jump across the PBL top is smaller than average, larger entrainment is needed to maintain balance. In regions with low monthly mean entrainment, the majority of the entrainment has to occur through "eddies", i.e. the time-varying part of the entrainment. This is most effective when a large entrainment velocity coincides with large jumps in q and θ across the PBL top.

This theory may answer the question of why the covariances have opposite signs in regions with large entrainment vs. regions with small entrainment, but it does not answer the question of why same-type covariances for q and θ have opposite effects on PBL depth.

Looking at the MLM equations, we see that the mixed-layer values q_B and θ_B are fixed input parameters. The combination larger-than-average PBL top jump and smaller-than-average entrainment effectively moistens and cools the PBL compared to the case without covariances. In the potential temperature equation, this is straight-forward: The PBL cools and entrainment is reduced, hence the PBL becomes shallower. In the moisture equation however, things are not as simple. Even though entrainment decreases here as well, the PBL deepens. This is the result of the fixed mixed-layer water vapor mixing ratio.

Since the PBL also becomes moister, and the mixing ratio cannot change, the PBL depth has to increase. The fact that the effects of $q3$ and $\theta 3$ cancel in this particular setup is a direct result of the MLM's formulation and has no true physical interpretation. In the GCM, where changes in the water vapor mixing ratio are possible at every time step, this should not be the case.

The corrections to the advective terms ($q2$ and $\theta 2$), i.e., the time-varying advections, seem to account for most of the discrepancy between the GCM's PBL depth and the MLM model's output in the non-convective regions. Taken separately, their effect on the PBL depth is not as striking as that of $q3$ and $\theta 3$, but $q2$ and $\theta 2$ both act in the same direction, and neglecting them decreases the PBL top significantly over the non-convective regions, and increases it over the convective regions, particularly along the ITCZ (Fig. 3.28). Both terms $q2$ and $\theta 2$ are positive in the ITCZ, SPCZ and warm pool, and negative in the non-convective regions. The zero contours are virtually identical with the ones in Fig. 3.27 and Fig. 3.28, but the colors are reversed. The terms $q2$ and $\theta 2$ have the effect of cooling and drying the PBL in the convective regions, and moistening and warming the PBL in the non-convective regions. As discussed above, a moistening of the PBL, all other things being equal, leads to an increase in the PBL depth due to the fixed PBL water vapor mixing ratio. Similarly, a warming of the PBL increases the PBL depth. Hence, both terms $q2$ and $\theta 2$ act to deepen the PBL in the non-convective regions, and reduce the PBL depth in the convective regions.

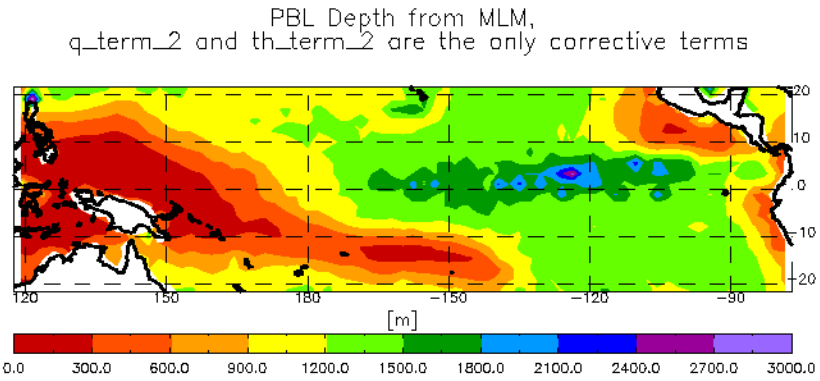

Figure 3.35: MLM PBL depth, only corrective terms in model equations are q_term_2 and th_term_2.

A closer look at $q2$ and $\theta 2$ reveals that those two terms are actually made up of several covariances.

$$q2 = \underbrace{\overline{(\pi \mathbf{v}_{hB} \cdot \nabla q_B)}}_{\text{q\_term\_0}} - \underbrace{(\bar{\pi}\overline{\mathbf{v}_{hB}} \cdot \nabla \overline{q_B})}_{\text{q\_term\_1}} = \underbrace{(\bar{\pi}\overline{\mathbf{v}_{hB}' \cdot \nabla q_B'})}_{\text{q\_term\_2}} + \underbrace{(\overline{\pi' \mathbf{v}_{hB}'} \cdot \nabla \overline{q_B})}_{\text{q\_term\_3}} + \underbrace{(\overline{\mathbf{v}_{hB}} \cdot \overline{\pi' \nabla q_B'})}_{\text{q\_term\_4}} + \underbrace{(\overline{\pi' \mathbf{v}_{hB}' \nabla q_B'})}_{\text{q\_term\_5}} \tag{3.8}$$

$$\theta 2 = \underbrace{\overline{(\pi \mathbf{v}_{hB} \cdot \nabla \theta_B)}}_{\text{th\_term\_0}} - \underbrace{(\bar{\pi}\overline{\mathbf{v}_{hB}} \cdot \nabla \overline{\theta_B})}_{\text{th\_term\_1}} = \underbrace{(\bar{\pi}\overline{\mathbf{v}_{hB}' \cdot \nabla \theta_B'})}_{\text{th\_term\_2}} + \underbrace{(\overline{\pi' \mathbf{v}_{hB}'} \cdot \nabla \overline{\theta_B})}_{\text{th\_term\_3}} + \underbrace{(\overline{\mathbf{v}_{hB}} \cdot \overline{\pi' \nabla \theta_B'})}_{\text{th\_term\_4}} + \underbrace{(\overline{\pi' \mathbf{v}_{hB}' \nabla \theta_B'})}_{\text{th \_term\_5}} \tag{3.9}$$

Not all of these covariances contribute equally to $q2$ and $\theta 2$. Including q_term_2 and th_term_2 together as only corrective terms can improve the PBL depth significantly (compare Fig. 3.35 to Fig. 3.16). In particular, the PBL depth in the non-convective region

is now reasonably deep. Since all the covariances contribute strongly to the PBL depth along the convergence line, it appears that fluctuations on shorter time scales than a month in all variables become important.

3-C-1 Summary

It appears that the steady state assumption is not so bad, but neglecting the covariances, especially q_term_2 and th_term_2, can influence the PBL depth rather drastically, at least for this particular version of the GCM, and for this sample month. Including these two covariance terms increases the PBL depth by several hundred meters and brings the MLM's PBL depth closer to the GCM's PBL depth. Since entrainment and the cumulus mass flux velocity are calculated using the PBL depth, they improve also when the covariances are included. Whether this is a characteristic of the MLM that is independent of the input data, or an attribute of the GCM data input, will be addressed in Chapter 4.

Chapter 4: The MLM Run with NCEP Re-analysis Data

4-A: NCEP re-analysis input vs. GCM input

In Chapter 3, the monthly mean fields from the GCM run were used as input for the MLM run. In this chapter, the MLM is run with four months of monthly mean NCEP re-analysis input data, which is shown in Fig. 4.1 through Fig. 4.10. The output fields for PBL depth, cumulus mass flux velocity and entrainment velocity are shown in Fig. 4.11 to Fig. 4.13.

The GCM input fields are the result of a GCM run for prescribed climatological SST of the month April. This GCM input is therefore expected to differ from the NCEP re-analysis input for the months January, April, July and October of 2001, and a direct comparison of the MLM output from the GCM input run with the output from the NCEP re-analysis April 2001 run should be approached very cautiously. Rather, what we have learned about the characteristics of the MLM in comparison to the GCM in Chapter 3 should be used when interpreting the MLM runs with NCEP re-analysis input. This section discusses the NCEP re-analysis input, in particular how the GCM input differs from the NCEP April 2001 input, and will attempt to put those differences in perspective to differences in the PBL properties diagnosed by the MLM.

The monthly mean surface evaporation for April 2001 compares relatively well to

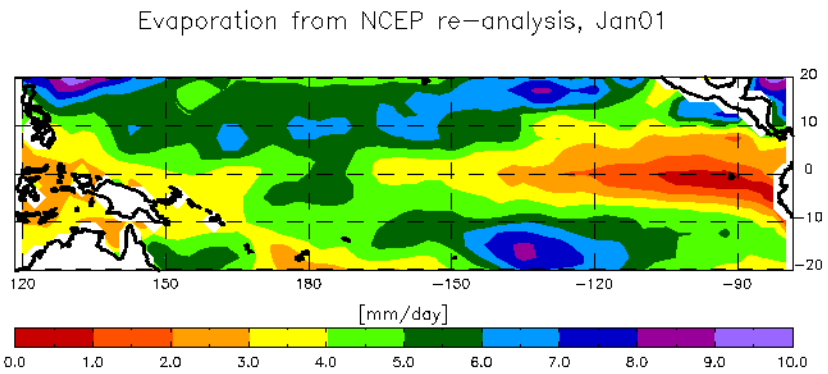

Figure 4.1: a) Monthly Mean Surface evaporation from NCEP re-analysis for January 2001

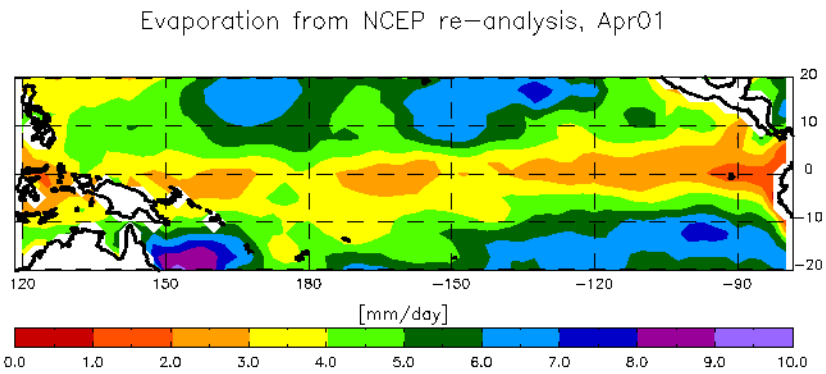

Figure 4.1: b) Same as a) for April 2001

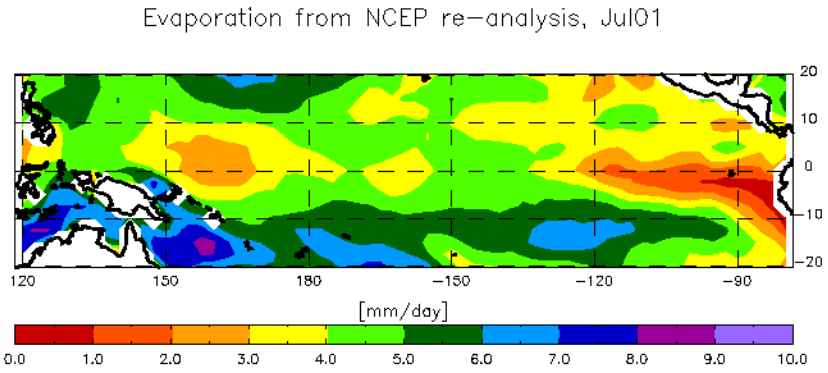

Figure 4.1: c) Same as a) for July 2001

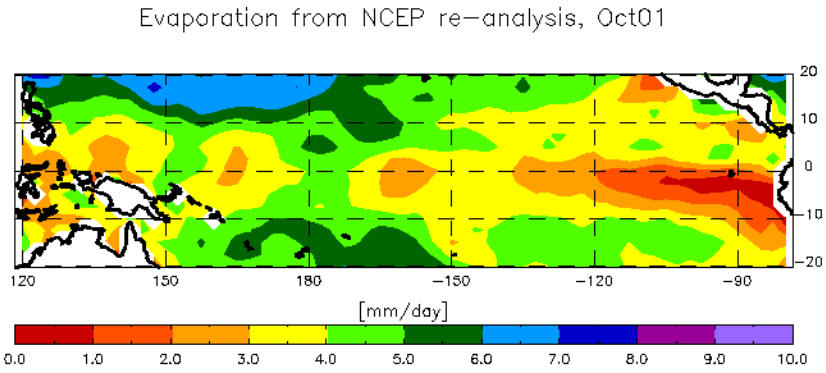

Figure 4.1: d) Same as a) for October 2001

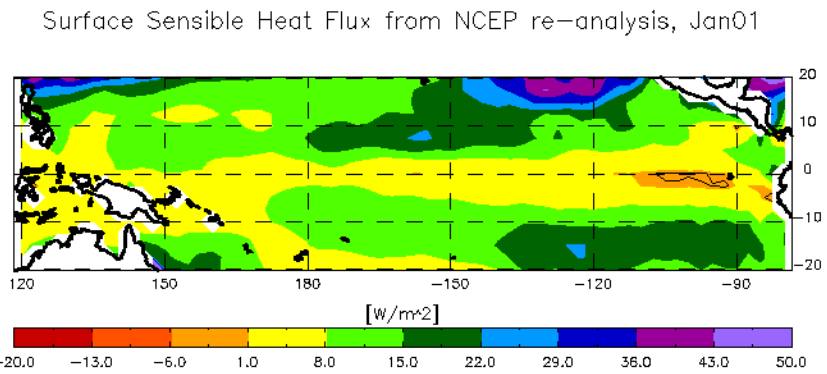

Figure 4.2: a) Monthly mean surface sensible heat flux from NCEP re-analysis for January 2001

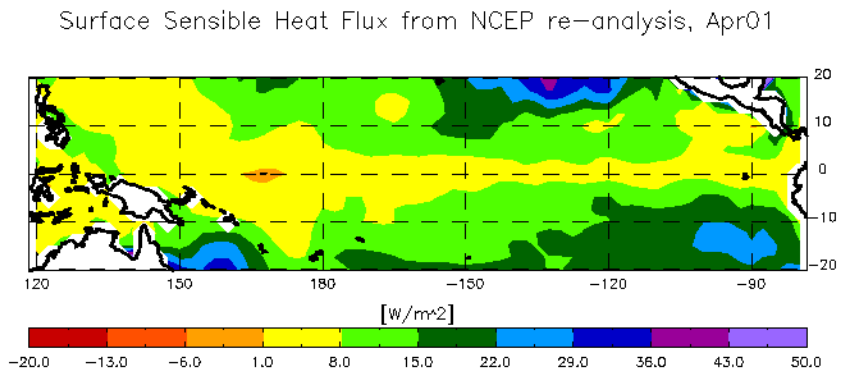

Figure 4.2: b) Same as a) for April 2001

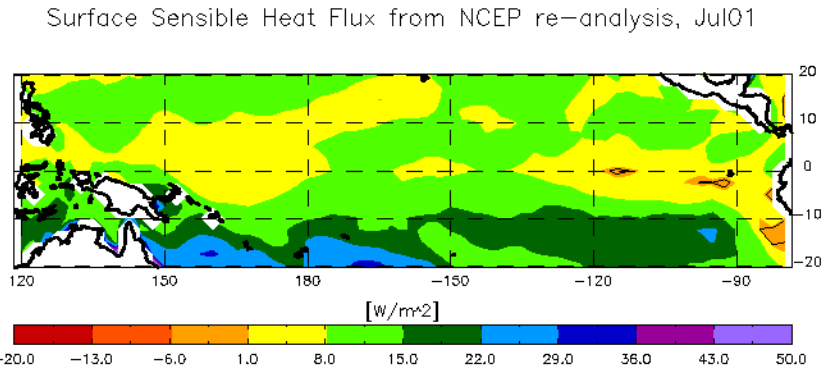

Figure 4.2: c) Same as a) for July 2001

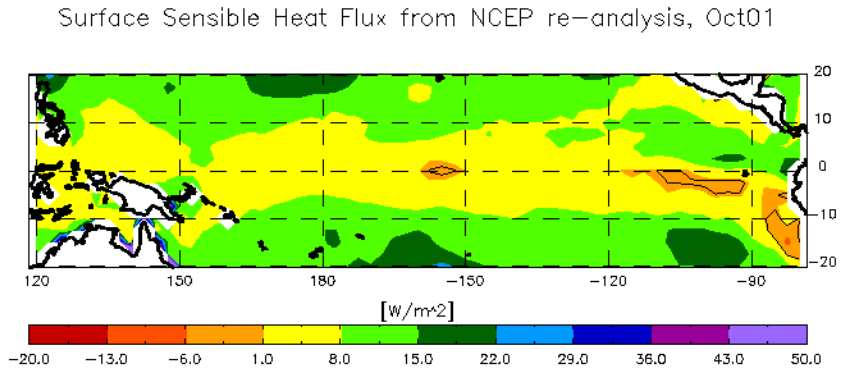

Figure 4.2: d) Same as a) for October 2001

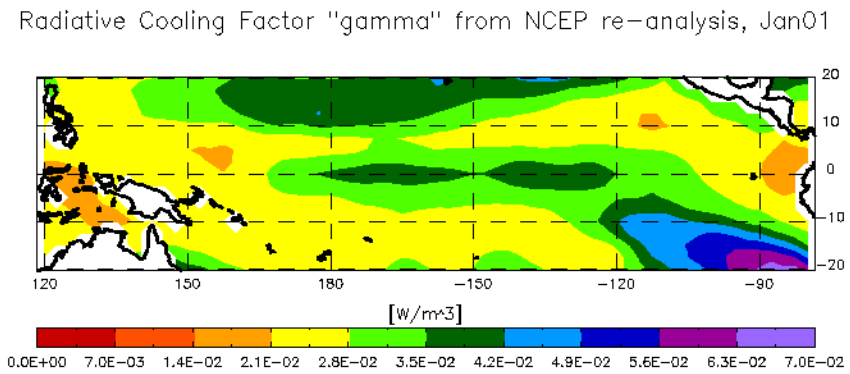

Figure 4.3: a) Monthly mean radiative cooling factor from NCEP re-analysis for January 2001

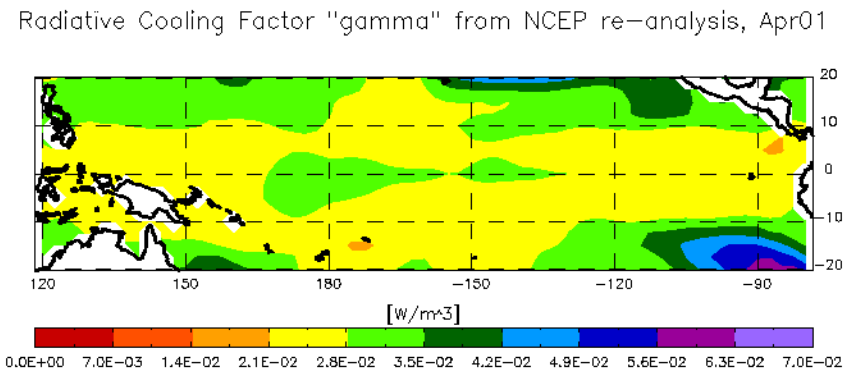

Figure 4.3: b) Same as a) for April 2001

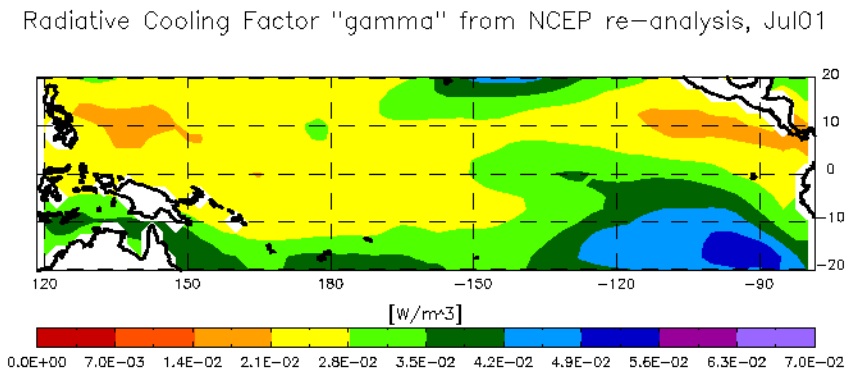

Figure 4.3: c) Same as a) for July 2001

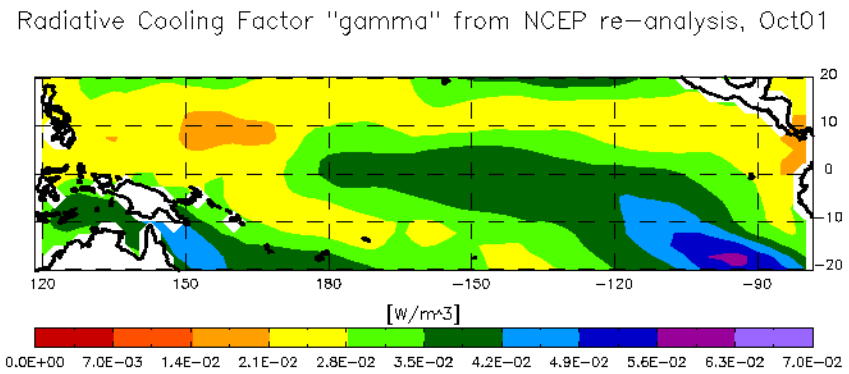

Figure 4.3: d) Same as a) for October 2001

the GCM's climatological April evaporation in magnitude as well as in the basic structure: Low evaporation over the cold tongue in the upwelling regions off the coast of South America, higher evaporation to the north and the south. The north-south gradient of evaporation is somewhat steeper in January and April than in July and October.

While the surface sensible heat flux of the GCM is negative over approximately a third of the domain, it is positive almost everywhere in the NCEP re-analysis, the exception being very small regions over the cold tongue and off the coast of Chile. The GCM's sensible heat flux ranged primarily between -10 $\mathrm{W\,m^{-2}}$ and 10 $\mathrm{W\,m^{-2}}$. In the NCEP re-analysis data, it ranges mostly between 0 and 15 $\mathrm{W\,m^{-2}}$. The highest fluxes can be found in the central north and south-east regions of the domain. Again, the north-south gradient of the flux is somewhat steeper for January and April than for July and October.

The choice of the radiative cooling factor γ works out rather well when compared to the GCM. The overall range of magnitude of γ is the same in the GCM and the NCEP re-analysis data. The distribution of gamma is also very similar, with the highest values in regions where we expect extensive areas of low clouds: off the South American and Californian coasts. In contrast to the GCM's γ, there is no maximum in the warm pool. Rather, γ is very low in this region. Intuitively, this makes more sense than a high γ, since the cirrus clouds associated with deep convection generally reduce the radiative cooling of the atmosphere.

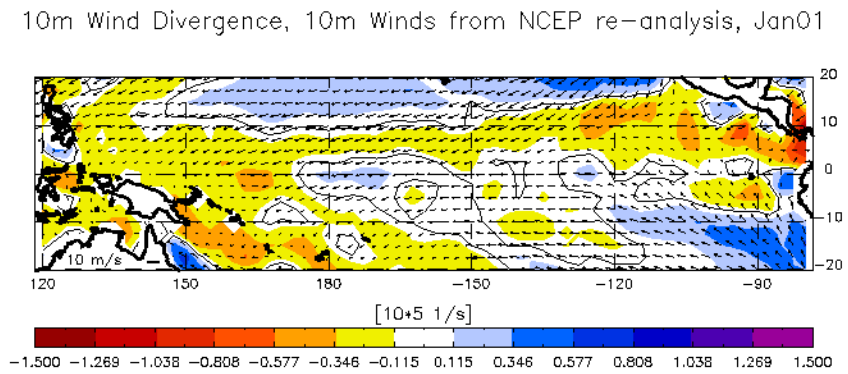

Figure 4.4: a) Shaded contours: Monthly mean 10 m wind divergence, zero contour in black. Arrows: Monthly mean10 m wind vectors. Data from NCEP re-analysis for January 2001

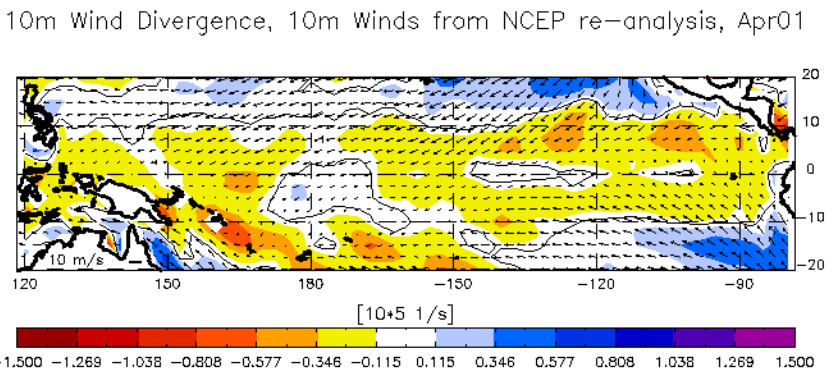

Figure 4.4: b) Same as a) for April 2001

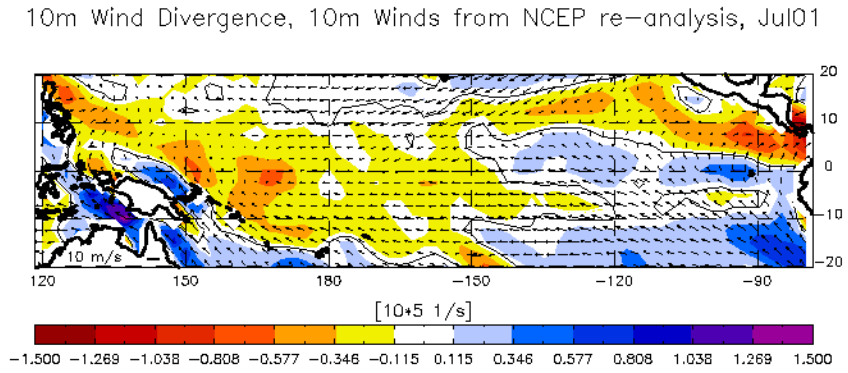

Figure 4.4: c) Same as a) for July 2001

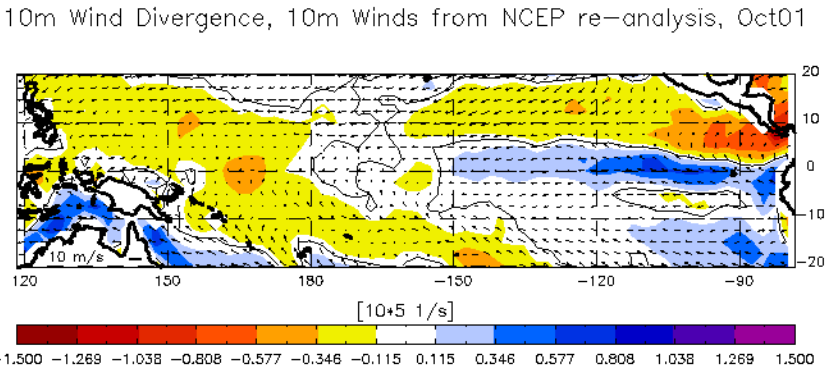

Figure 4.4: d) Same as a) for October 2001

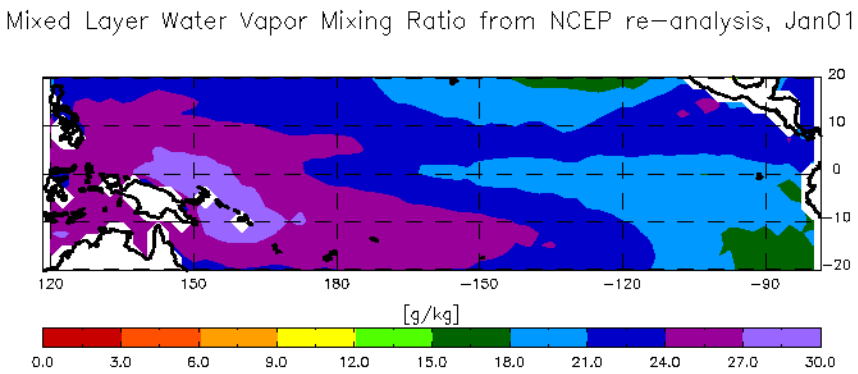

Figure 4.5: a) Monthly mean water vapor mixing ratio of the mixed PBL from NCEP re-analysis for January 2001

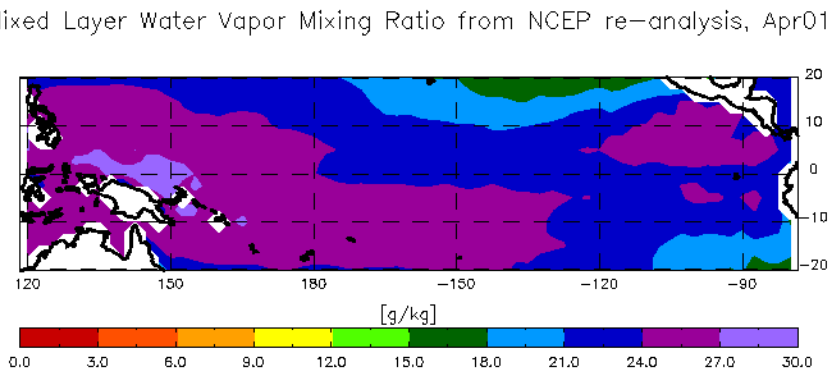

Figure 4.5: b) Same as a) for April 2001

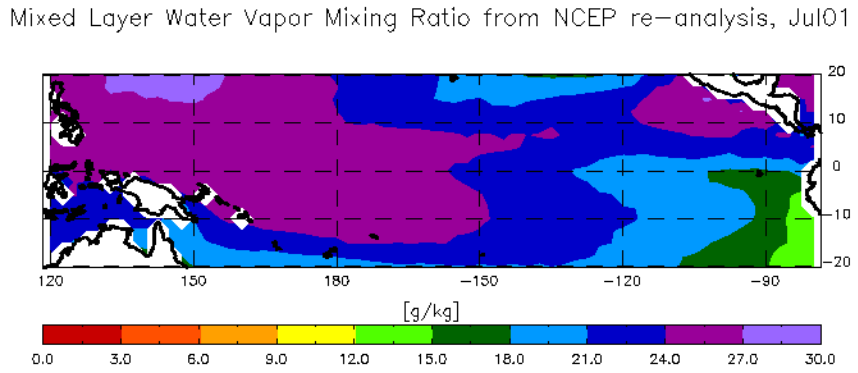

Figure 4.5: c) Same as a) for July 2001

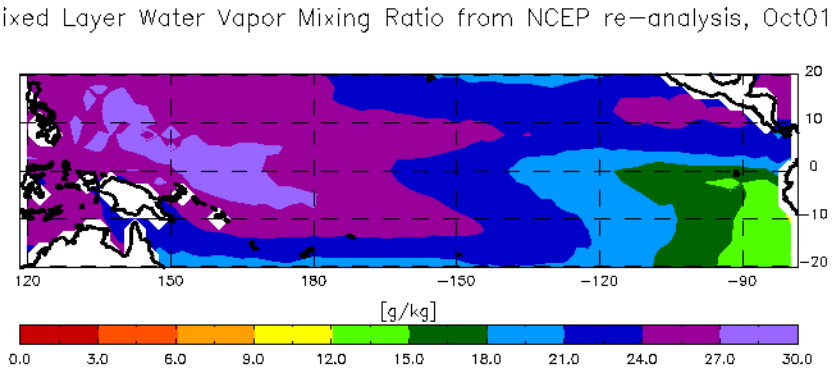

Figure 4.5: d) Same as a) for October 2001

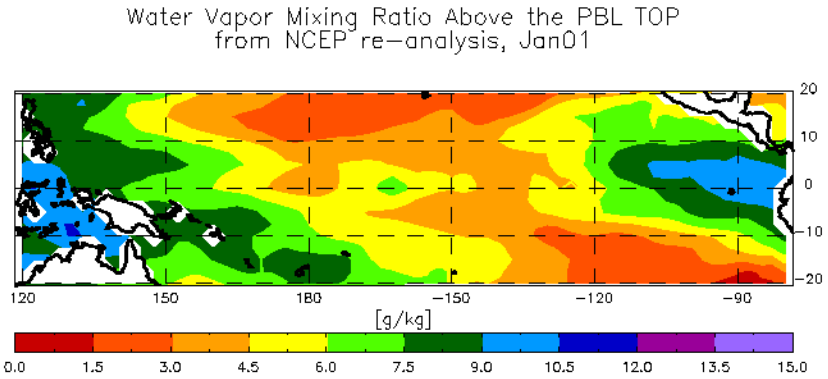

Figure 4.6: a) Monthly mean water vapor mixing ratio above the PBL top from NCEP re-analysis for January 2001

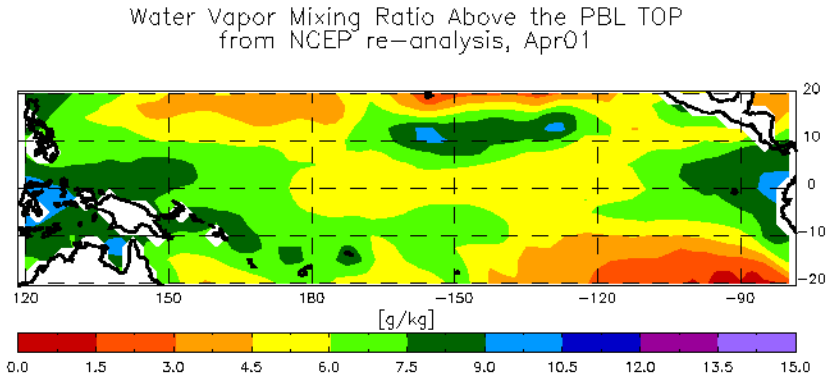

Figure 4.6: b) Same as a) for April 2001

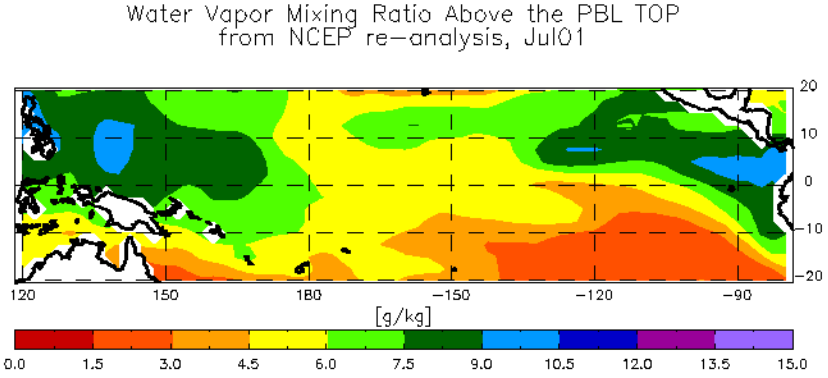

Figure 4.6: c) Same as a) for July 2001

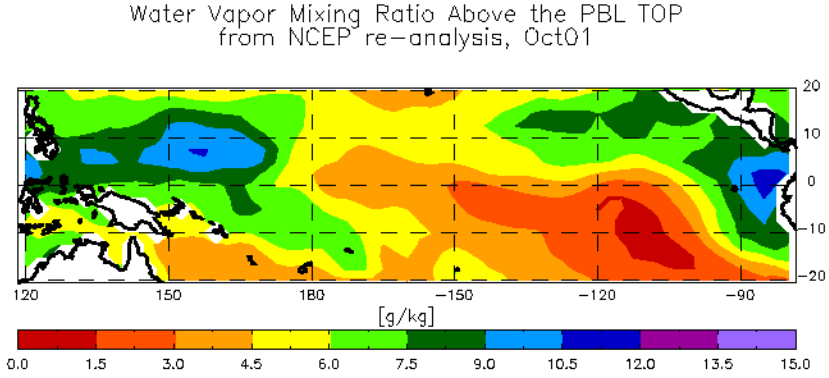

Figure 4.6: d) Same as a) for October 2001

The 10 m wind divergence ranges mostly between values of $1\times10^{5}s^{-1}$ and $-1\times10^{5}s^{-1}$ in all four sample months. Rather broad bands and regions of convergence mark the ITCZ and SPCZ, as well as the warm pool. In April, the data show a pronounced double ITCZ with only slightly stronger convergence in the northern hemisphere. There is a weaker southern convergence zone from 90W to 120W, roughly along 7S in all three other sample months. The 10 m winds are weak in the warm pool and stronger in the eastern half of the basin. Compared to the GCM's mixed layer wind divergence, the 10m wind divergence from the NCEP re-analysis is overall somewhat weaker and the convergence lines are broad, more like wide bands. Note the GCM's mixed layer winds are not the exact equivalent of the 10 m winds as in the NCEP data. Also, there is no clear indication of a southern hemispheric convergence zone in the GCM.

The mixed layer water vapor mixing ratio from the NCEP re-analysis data is about $5\ \mathrm{g\,kg^{-1}}$ higher over the warm ocean regions than in the GCM, but is approximately the same over the cold ocean regions. The north-south moisture gradient is a little steeper in the GCM.

Above the inversion, the GCM's water vapor mixing ratio is an almost uniform 13 $\mathrm{g\,kg^{-1}}$. In the NCEP re-analysis, it is in the single digits almost everywhere, with larger values over the cold tongue and the warm pool.

The dry static energy calculated from NCEP re-analysis data follow the sea-surface temperature's structure very closely. It is high over warm ocean and low over the

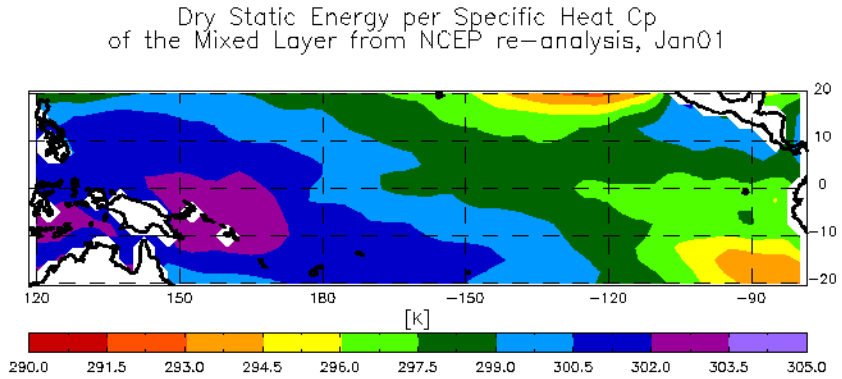

Figure 4.7: a) Monthly mean dry static energy per specific heat at constant pressure (c_p) of the mixed PBL from NCEP re-analysis for January 2001

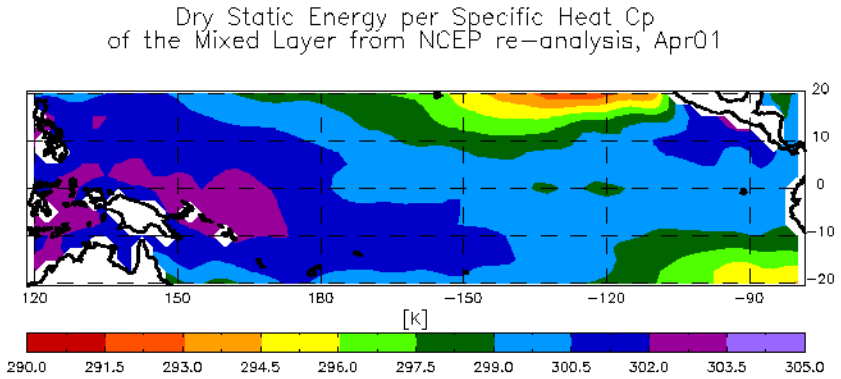

Figure 4.7: b) Same as a) for April 2001

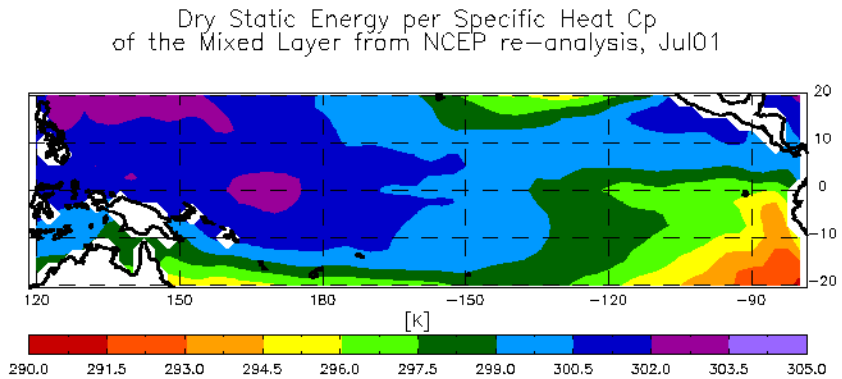

Figure 4.7: c) Same as a) for July 2001

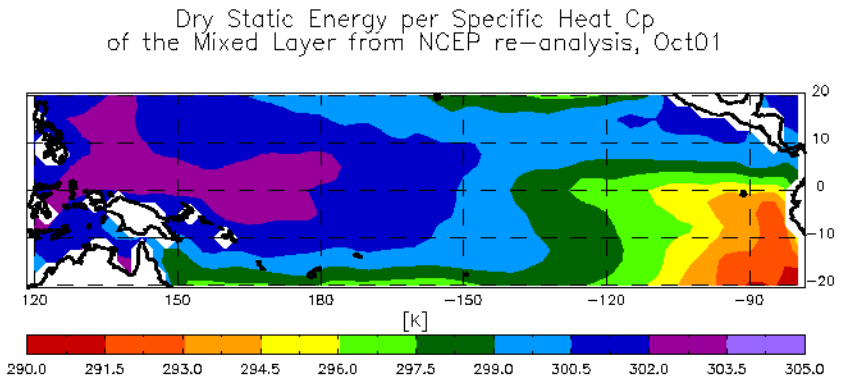

Figure 4.7: d) Same as a) for October 2001

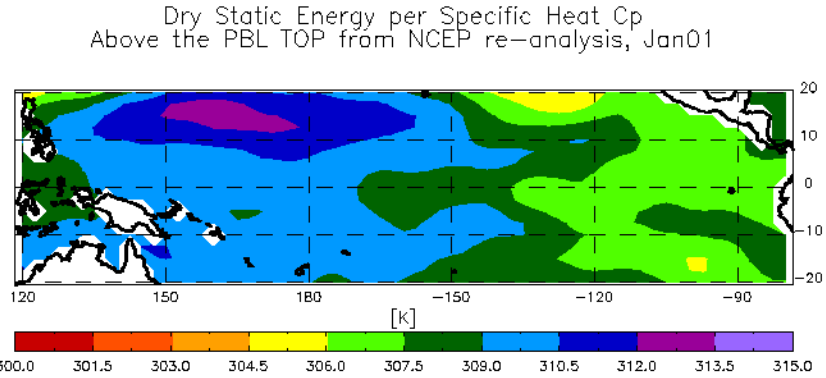

Figure 4.8: a) Monthly mean dry static energy per specific heat at constant pressure (c_p) above the PBL top from NCEP re-analysis for January 2001

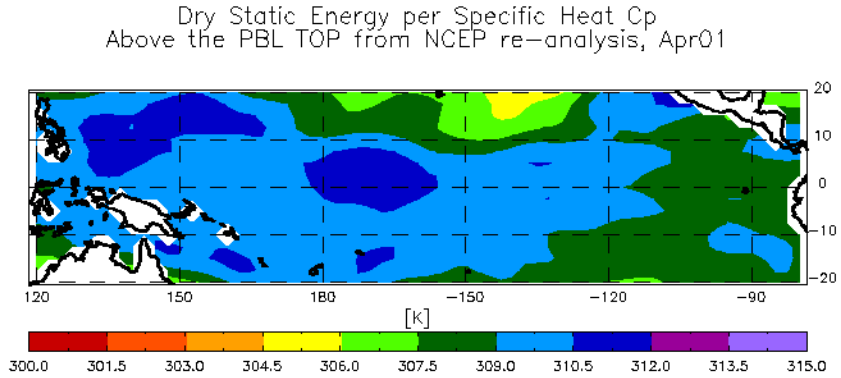

Figure 4.8: b) Same as a) for April 2001

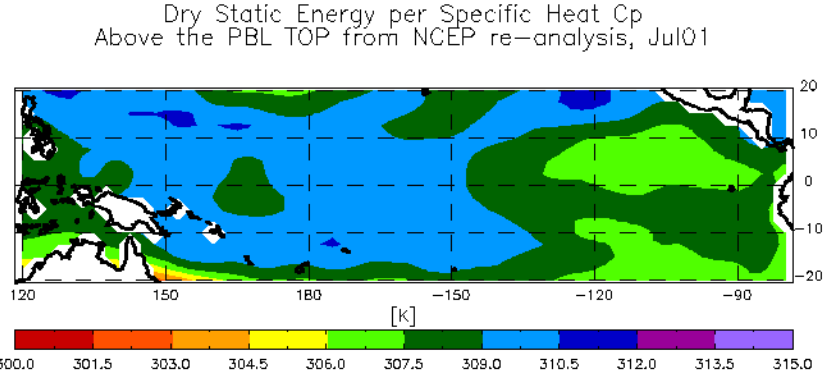

Figure 4.8: c) Same as a) for July 2001

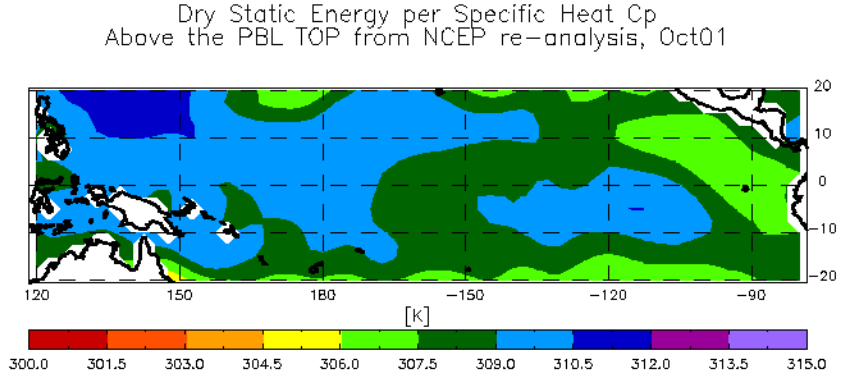

Figure 4.8: d) Same as a) for October 2001

cold ocean. The dry static energy per specific heat varies by ~10 K over the domain in all four sample months. The strong double ITCZ signature is reflected in the April dry static energy.

Above the PBL top, the dry static energy per specific heat is much more spatially uniform. It varies only by 5 to 6 K over the whole domain, in all four months. The clear warm-ocean signature has been lost, and while the western half of the domain has generally higher dry static energies than the eastern, there is very little indication of an ITCZ-like feature in the eastern half.

4-A-1 Summary

One of the main differences between the GCM data input and the NCEP re-analysis for April 2001 is that the jumps across the PBL top for water vapor mixing ratio and potential temperature/ dry static energy are larger in the NCEP data than in the GCM data. Also, the energy that the PBL gains through the surface sensible heat flux is significantly larger in the re-analysis data than in the GCM data. To compensate for the smaller PBL top jumps and less energy supplied at the surface, we should expect the entrainment velocity to be larger in the GCM data, all other things being equal, in particular in those areas where the surface sensible heat flux in the GCM data is very low compared to the re-analysis' sensible heat flux (roughly along the equator in the eastern half of the domain). On the other hand, an upward sensible heat flux strengthens the turbulence which in turn favors stronger entrainment.

The situation over in the warm pool is similar, except for the radiative cooling

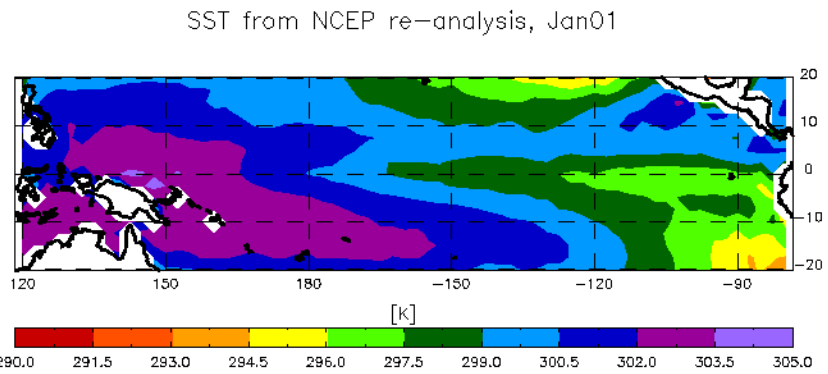

Figure 4.9: a) Monthly mean sea-surface temperature from NCEP re-analysis for January 2001

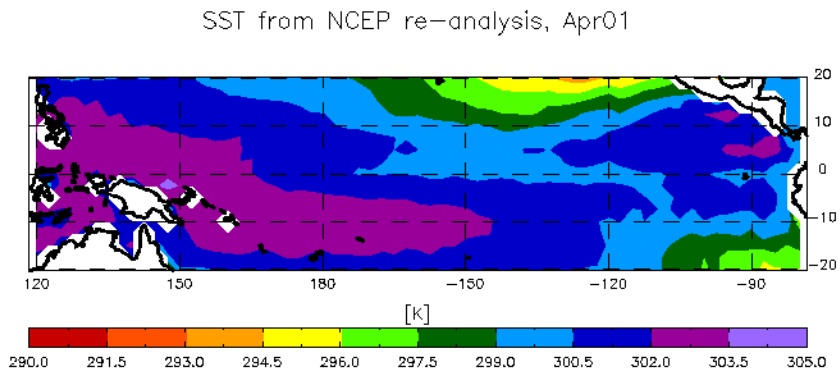

Figure 4.9: b) Same as a) for April 2001

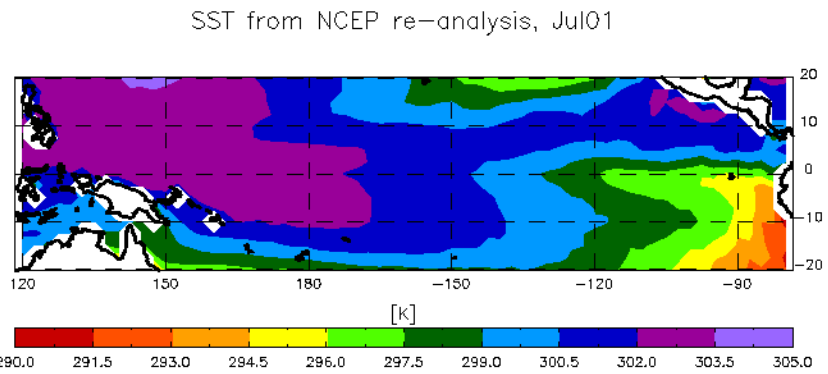

Figure 4.9: c) Same as a) for July 2001

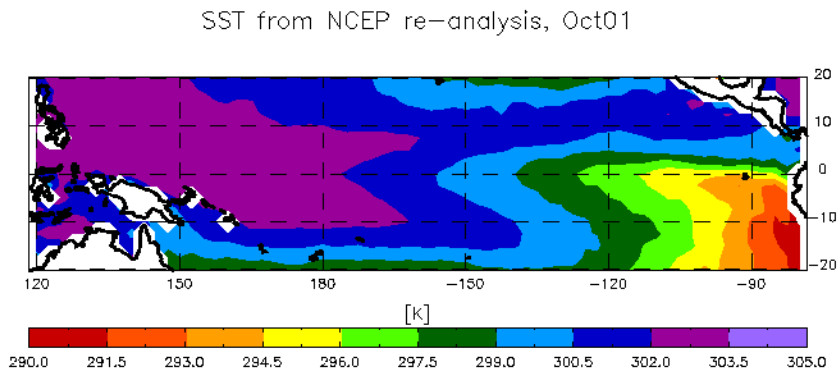

Figure 4.9: d) Same as a) for October 2001

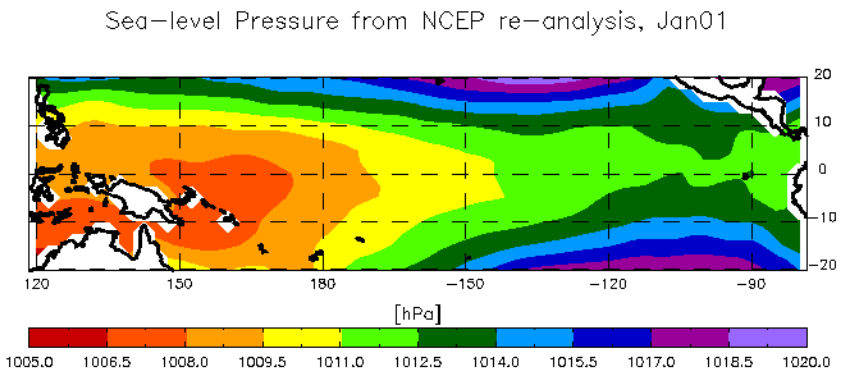

Figure 4.10: a) Monthly mean sea-level pressure from NCEP re-analysis for January 2001

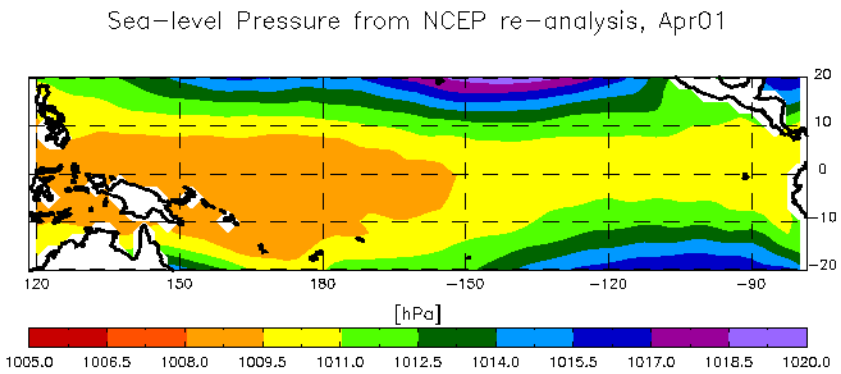

Figure 4.10: b) Same as a) for April 2001

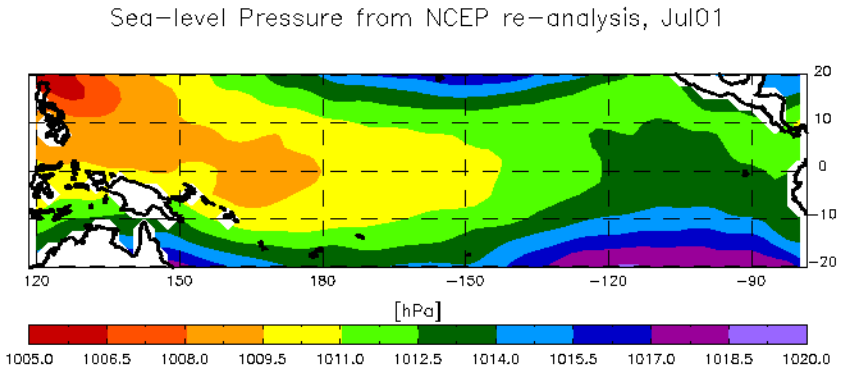

Figure 4.10: c) Same as a) for July 2001

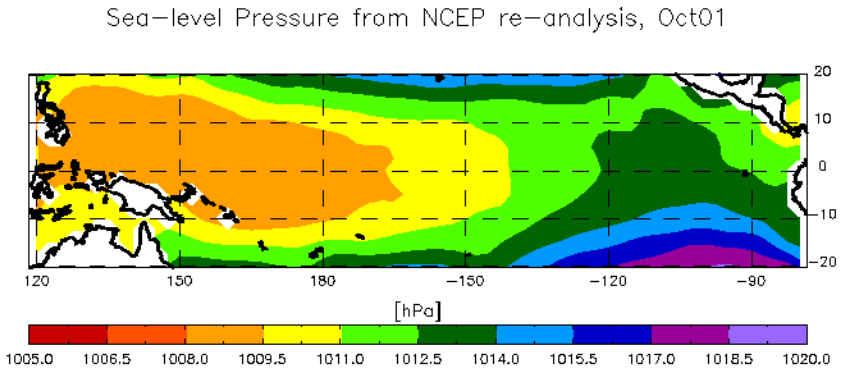

Figure 4.10: d) Same as a) for October 2001

factor γ. While γ is similar in the east Pacific for the GCM and NCEP data, this is not the case in the warm pool. Here, the GCM γ is almost three times as large as in the NCEP γ. This means that the radiative cooling is stronger in the GCM for a given PBL depth, or, following the MLM's order of solving the model equations, a shallower PBL depth is sufficient in the GCM to produce the radiative cooling needed to balance the conservation equations. This may indicate that the GCM does not produce sufficient cirrus clouds in the deep convective regions.

Another difference between GCM data and NCEP re-analysis data is the lack of a double ITCZ feature in the east Pacific in any of the GCM data fields. Hence, we should not expect to see any double ITCZ features in the MLM run with GCM data input. The double ITCZ is evident in most of the NCEP re-analysis fields for April 2001, in particular in the 10 m wind divergence field, the radiative cooling factor and the mixed-layer dry static energy. In fact, the 10 m winds converge south of the equator in the east Pacific in all sample months.

4-B: Model results with NCEP re-analysis input

The MLM produces a PBL depth around 800 m over most of the domain in all four sample months. The PBL depth typically has a pronounced maximum along the ITCZ and SPCZ, where depths of 1500 m to more than 3000 m can be reached. On the other hand, there is a minimum over the cold tongue and extending along the equator, where the PBL depth can be as small as 300 m. The PBL shows a strong double ITCZ signature in April, marked by two bands of deep PBL depths, to the point where the southern hemisphere's

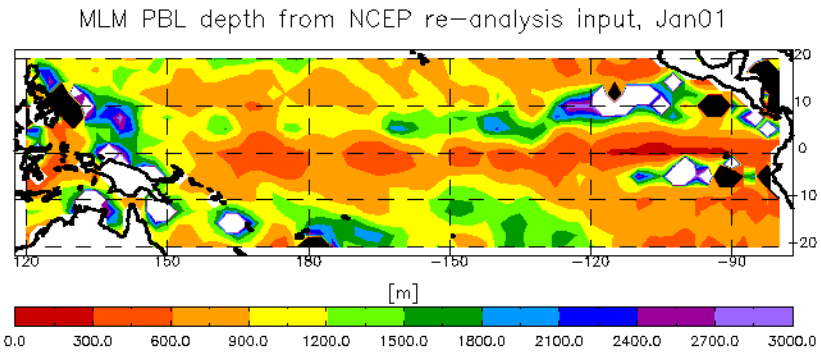

Figure 4.11: a) MLM PBL depth from NCEP re-analysis input for January 2001. White areas indicate above-scale values, black areas indicate below-scale values

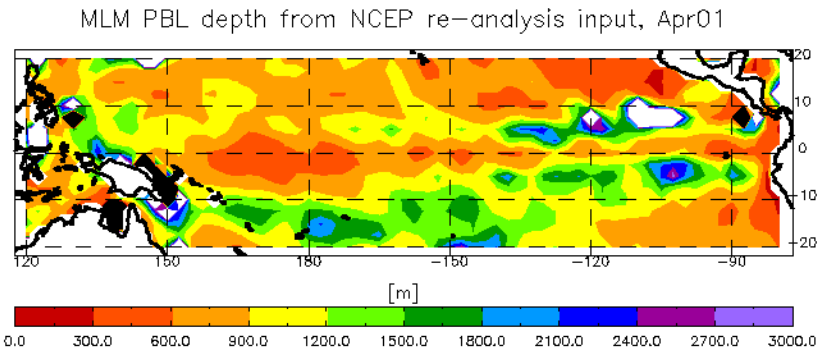

Figure 4.11: b) Same as a) for April 2001

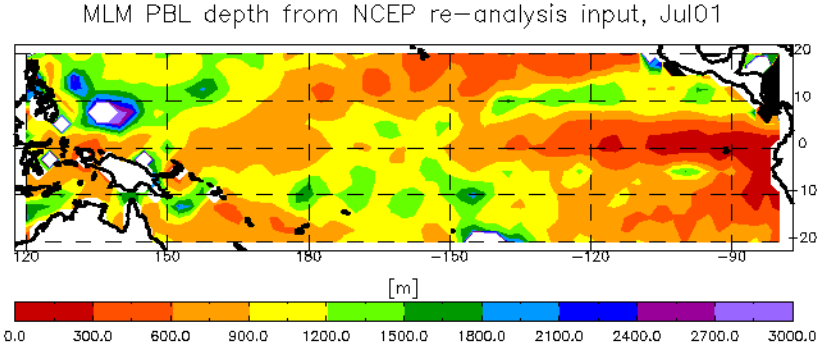

Figure 4.11: c) Same as a) for July 2001

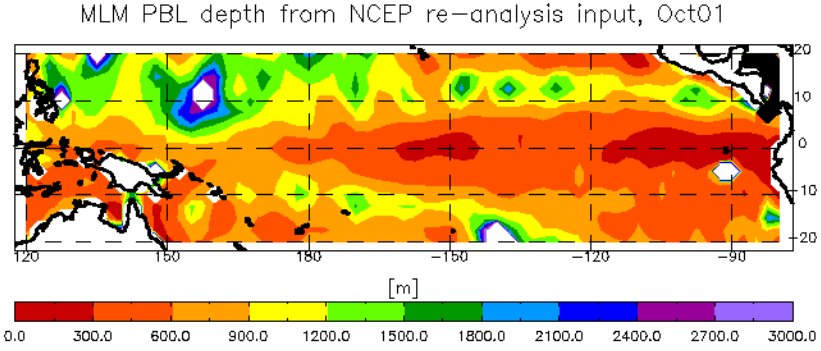

Figure 4.11: d) Same as a) for October 2001

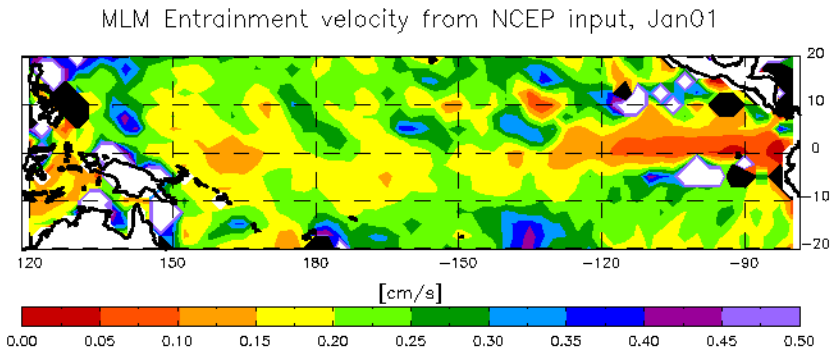

Figure 4.12: a) MLM entrainment velocity from NCEP re-analysis input for January 2001. White areas indicate above-scale values, black areas indicate below-scale values.

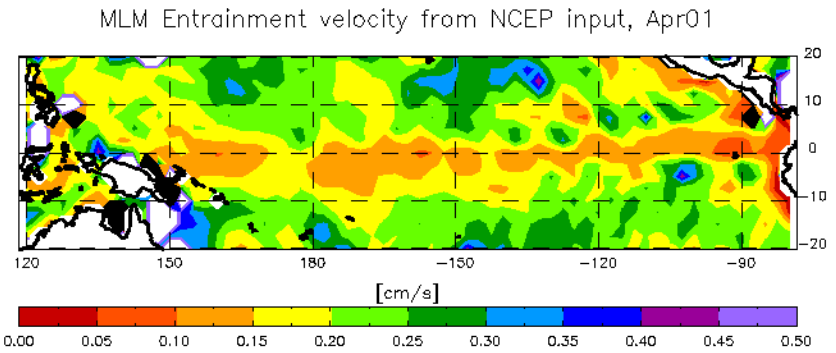

Figure 4.12: b) Same as a) for April 2001

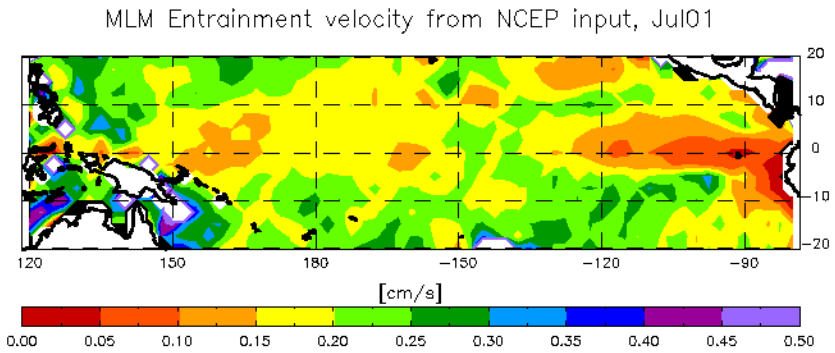

Figure 4.12: c) Same as a) for July 2001

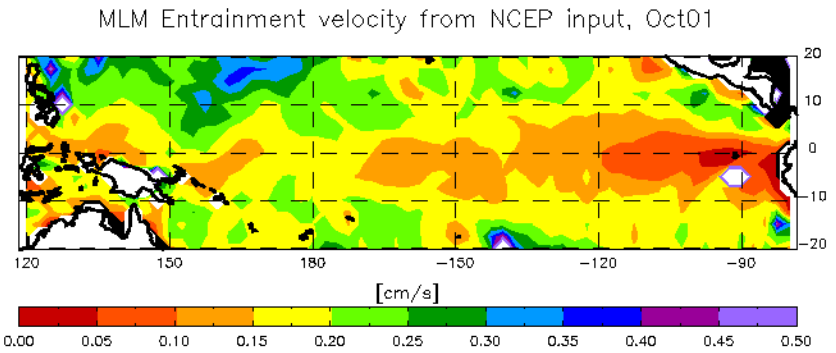

Figure 4.12: d) Same as a) for October 2001

ITCZ appears to be stronger than the northern hemisphere's. Since the double ITCZ is evident in most of the April input data, we should expect it to be present in the output fields also. In the month of January, a double ITCZ east of 120° W is evident as well. In all four months, the SPCZ is rather parallel to the equator, extending to 120° W at 20° S. Overall, the variability of the PBL in the NCEP re-analysis data as interpreted by the MLM is larger than for the CSU GCM.

To an extent, the entrainment co-varies with the PBL depth: it is small over the cold tongue and along the equator, and larger towards the poles. In the MLM, this is due at least in part, to the radiative cooling varying linearly with PBL depth. Since entrainment introduces more mass into the PBL, strong entrainment should make the PBL deeper, unless mass is removed from the PBL another way (wind divergence, cumulus mass flux). Apart from the basic structure of low entrainment over the cold tongue/equator and large entrainment away from it, the field is rather unstructured. The entrainment velocity is positive and its magnitude lies roughly in the range of up to half a centimeter per second. This is a significantly smaller entrainment rate than the one found in the GCM. We anticipated a somewhat smaller entrainment velocity based on the NCEP re-analysis input data.

The cumulus massflux velocity is very noisy and often negative. This is bad, as it is defined in such a way as to be positive in convective regions and zero elsewhere. w_C is the last of the parameters to be diagnosed and is calculated as $w_C = w_E - \nabla_h \cdot (\mathbf{v}_{hB} H)$. We

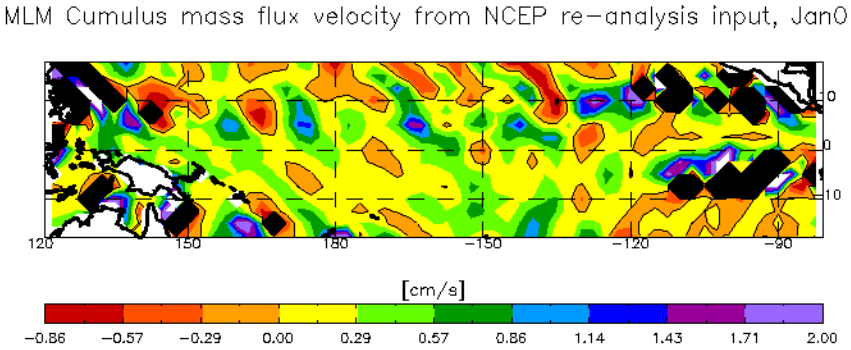

Figure 4.13: a) MLM cumulus mass flux velocity from NCEP re-analysis input for January 2001. White areas indicate above-scale values, black areas indicate below-scale values. Zero contour in black.

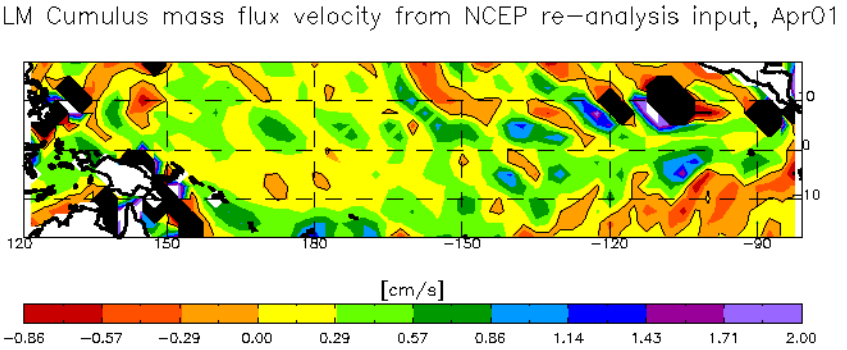

Figure 4.13: a) MLM cumulus mass flux velocity from NCEP re-analysis input for April 2001. White areas indicate above-scale values, black

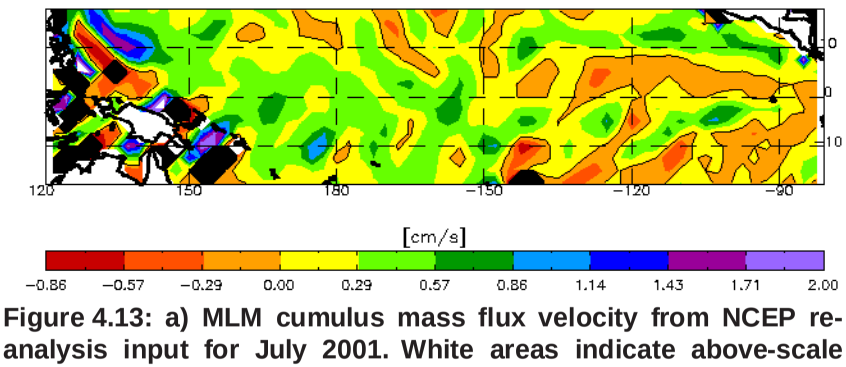

Figure 4.13: a) MLM cumulus mass flux velocity from NCEP re-analysis input for July 2001. White areas indicate above-scale values, black

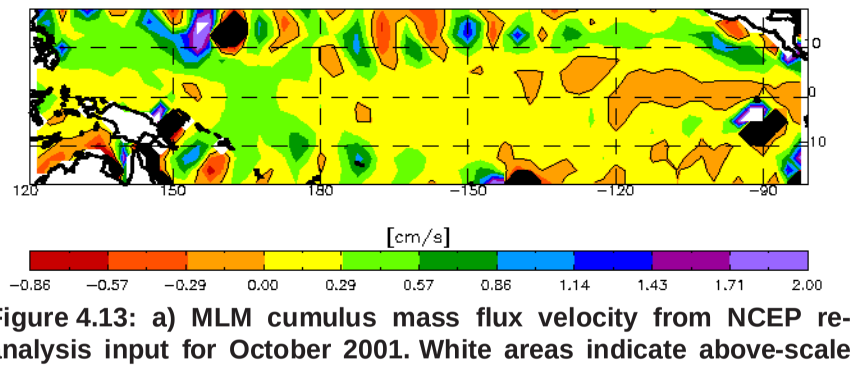

Figure 4.13: a) MLM cumulus mass flux velocity from NCEP re-analysis input for October 2001. White areas indicate above-scale values, black

have seen that w_E is fairly small, and that the PBL depth's spatial variability is larger than we would expect from the GCM or observations (for discussion of observations, see Chapter 5). The large gradient of the PBL depth and the weak entrainment together lead to areas of negative cumulus massflux velocity. With the strong noise, it is hard to say anything about an underlying structure. Contrasting the months October and April, one might say that for the month of October, w_C is larger along the ITCZ and SPCZ than over the south-east part of the domain. In April, where other fields show a southern ITCZ as strong as the northern ITCZ, w_C is larger between 10N and 10S in the east Pacific than polewards of those latitudes.

4-B-1 Summary

Overall, the MLM does a good job predicting the sign of both the PBL depth and the entrainment velocity. The magnitude of these two properties is also reasonable, although the PBL depth tends to be very small over the cold tongue, and very large in other regions, mostly where we'd expect convection. The PBL depth generally increases towards the warm pool and ITCZ, which is in contrast to the GCM's PBL depth, which is smallest over the warm pool. The entrainment velocity has a minimum over the cold tongue as well. Since there are fewer observations of the entrainment velocity available, it is hard to say how well the MLM compares to reality, as we observe it.

A look at the moisture and dry static energy equations may explain why the PBL is deep in the convective regions:

$$0 = -(H\mathbf{v}_{hB} \cdot \nabla_h q_B) + w_E(q_H - q_B) + \frac{EVP}{\rho_0} \tag{4.1}$$

$$0 = -(H\mathbf{v}_{hB} \cdot \nabla_h s_B) + w_E(s_H - s_B) + \frac{SH - \gamma H}{\rho_0} \tag{4.2}$$

In the stable regions, for example, where subsidence and surface divergence are dominant, moisture and dry static energy are advected out of the region, i.e. the advective terms in (4.1) and (4.2) are positive (negative including the minus sign). Evaporation is positive over all of the domain and radiative cooling, particularly in the stratocumulus regions, is large. Hence, in the moisture equation, evaporation will largely balance the drying due to moisture advection out of the region and the entrainment velocity (for a fixed PBL-top jump $q_H - q_B$) must be small. In the dry static energy equation, both advection and radiative cooling reduce the PBL dry static energy. To maintain balance, entrainment (for a fixed PBL-top jump $s_H - s_B$) must be large. To illustrate this argument, we have calculated the entrainment velocity from the moisture and dry static energy equation separately, assuming a uniform PBL depth of 1000m over the domain:

$$w_E^q = \frac{1000\ \mathrm{m}(\mathbf{v}_{hB} \cdot \nabla_h q_B) - \dfrac{EVP}{\rho_0}}{(q_H - q_B)} \tag{4.3}$$

$$w_E^s = \frac{1000\ \mathrm{m}(\mathbf{v}_{hB} \cdot \nabla_h s_B) - \dfrac{SH - \gamma(1000\ \mathrm{m})}{\rho_0}}{(s_H - s_B)} \tag{4.4}$$

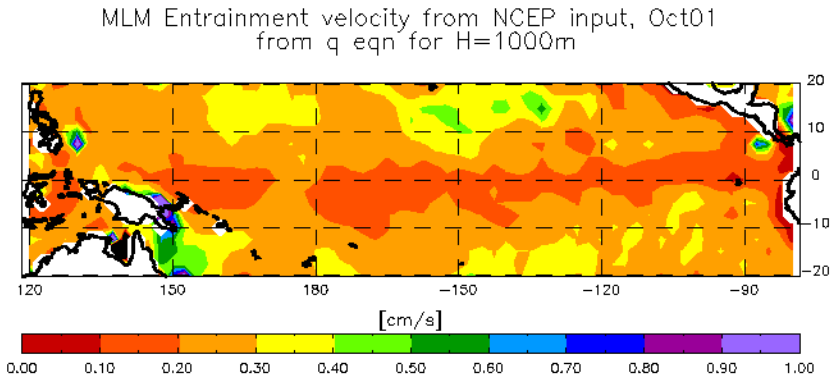

Figure 4.14: w_E^q **calculated from the moisture equation only, assuming uniform PBL depth of 1000 m.**

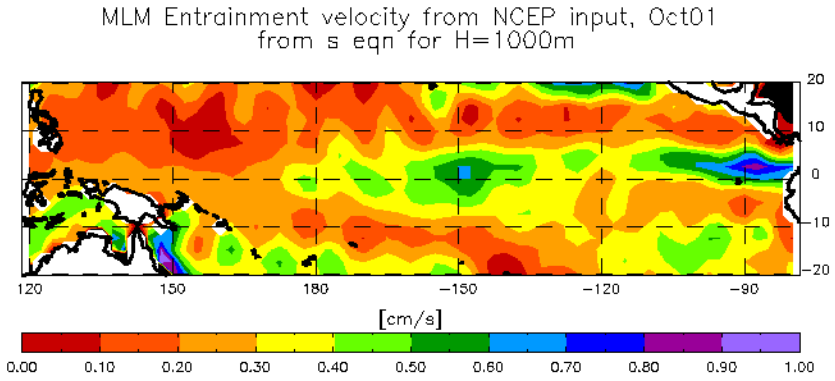

Figure 4.15: w_E^s **calculated from the dry static energy equation only, assuming uniform PBL depth of 1000 m.**

Fig. 4.14 and Fig. 4.15 show the two entrainment velocities. As expected, w_E^q is small in the non-convective regions (particularly along the Equator). w_E^s on the other hand is large in the non-convective regions.

The diagnosed entrainment velocity must satisfy both equations, but only the dry static energy equation has the ability to adjust through the variable radiative cooling term. The moisture equation "wins" and determines w_E in the MLM (compare Fig. 4.14 and Fig. 4.12 d), observe the different color scales). Since w_E is small in the non-convective

regions, the dry static energy equation adjusts by making the radiative cooling (and therefore H) very small in order for the warming from the surface sensible heat flux to balance the cooling due to advection. This results in a very low PBL depth in the stratocumulus region.

The opposite is the case in the convective regions. Here, moisture and dry static energy are advected into the convective regions. In the moisture equation, a large w_E must balance the moistening through advection and evaporation. The dry static energy balanced this additional heating of the PBL through entrainment by increasing the radiative cooling (and therefore H). As it turns out, the moisture equation determines the entrainment velocity, and the dry static energy determines the PBL depth.

A solution to this problem would be a modification of the model equations such that both equations can reconcile their requirements for entrainment without adjusting the radiative cooling, and with it the PBL depth, in such a drastic way. Adjustable PBL-top jumps in q and s would allow a modification of the heating and drying through entrainment by increasing or decreasing the dry static energy and water vapor mixing ratio of the entrained air rather than the entrainment rate itself. A more physical modification could be achieved by letting the cumulus mass flux help dry the PBL in the convective regions by lifting air out of the PBL that is moister than the regular PBL water vapor mixing ratio. However, both of these approaches complicate the model formulation and may make it impossible to solve the set of equations analytically.

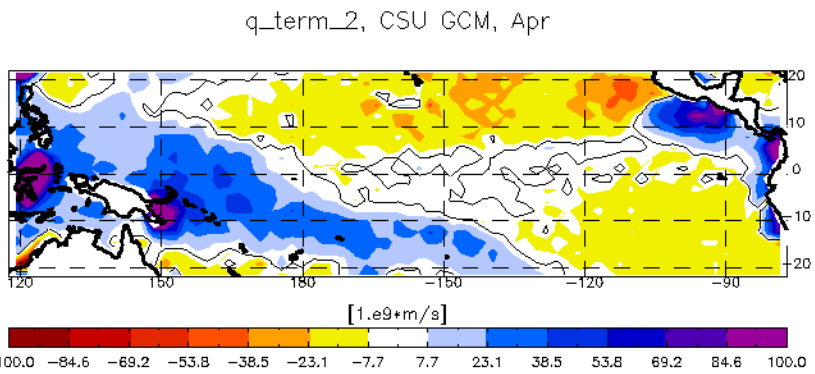

Figure 4.16: a) Covariance $\overline{\mathbf{v}' \cdot \nabla q'}$ from the GCM run for data every 200s.

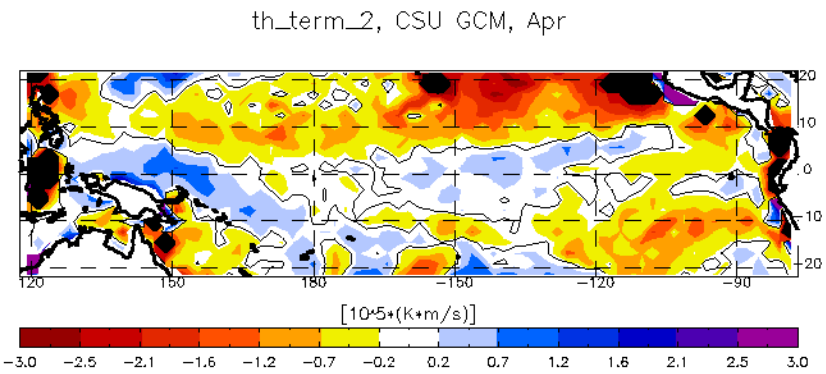

Figure 4.16: b) Covariance $\overline{\mathbf{v}' \cdot \nabla \theta'}$ from the GCM run for data every 200s.

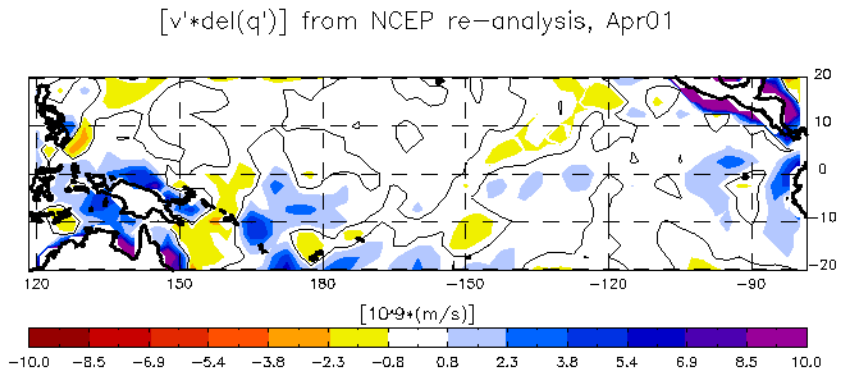

Figure 4.17: a) Covariance $\overline{\mathbf{v}' \cdot \nabla q'}$ from the MLM run with NCEP re-analysis input for April 2001, four times daily.

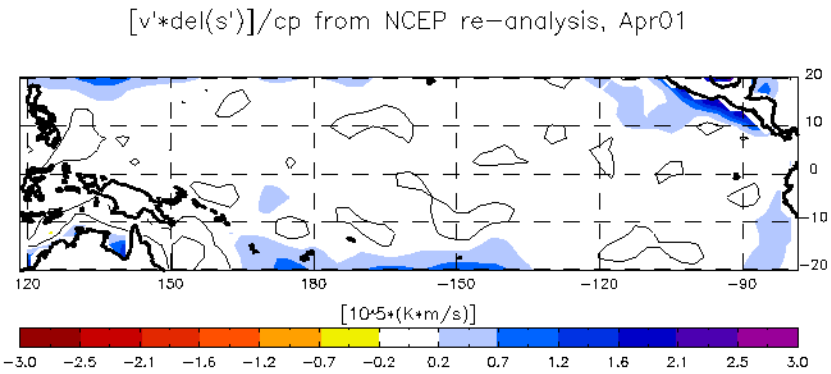

Figure 4.17: b) Covariance $\overline{\mathbf{v}' \cdot \nabla \theta}$ from the MLM run with NCEP re-analysis for April 2001, four times daily.

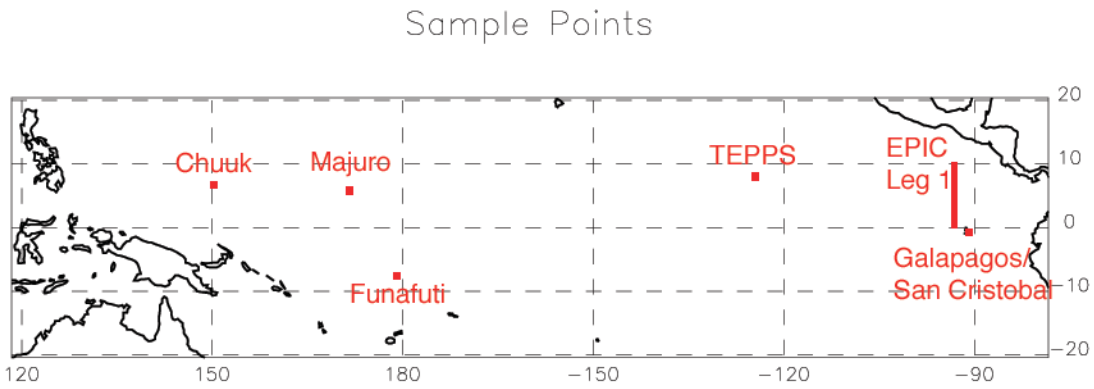

Figure 4.18: Locations of the radiosonde observations

The NCEP re-analysis' boundary layer scheme is a local-Richardson number based diffusion scheme. In theory, the PBL can extend through all 28 σ layers of the model, but typically only the five levels closest to the surface are effected (up to $\sigma = 0.856$). The model's shallow convection scheme requires the cloud base of shallow convective clouds to lie in either layer two ($\sigma = 0.981$) or layer three ($\sigma = 0.960$). I. e. the subcloud layer's top cannot be higher than $\sigma = 0.960$, which corresponds roughly to 450 m. The top of the shallow convection cannot extend above layer six ($\sigma = 0.884$, ~1000 m). This constrains the PBL top, though not an explicit parameter in the re-analysis, to fairly low atmospheric layers in regions with shallow convection. That being the case, he low PBL depths produced by the MLM may in fact do a fairly good job at reproducing the re-analysis' PBL depth. The parameterization for deep convection is a simplified Arakawa-Schubert scheme.

The cumulus mass flux is the variable that the MLM has the most trouble diagnosing. The absolute magnitude of the cumulus mass flux velocity is on the order of 1

$\mathrm{cm\ s^{-1}}$, which agrees with the GCM's cumulus mass flux velocity. The noise in the field and the negative velocities are a problem, though.

In Chapter 3, when the MLM was run with the GCM input data, the diagnosed variables improved significantly (compared to the GCM's PBL depth, entrainment velocity and cumulus mass flux velocity) when temporal covariances were taken into account. The next section will look at the role of covariances for the NCEP re-analysis run of the MLM.

4-C: The steady state assumption, covariances and variability

When the PBL model is used with NCEP re-analysis data, the entrainment velocity, cumulus mass flux velocity and PBL depth are truly unknown, and we cannot calculate the covariances that involve those three variables as was done for the GCM in Chapter 3. The only covariances that can be calculated from the four-times daily re-analysis product are $\overline{\mathbf{v}_{hB}'\nabla q_B'}$ and $\overline{\mathbf{v}_{hB}'\nabla s_B'}$. The corresponding terms in the GCM where the ones mainly responsible for increasing the PBL depth over the non-convective regions to reasonable values. However, compared to the same covariances from the GCM run, these terms are small and have little effect on the PBL depth when included in the model equations (Fig. 4.16 a) to Fig. 4.17 b)).

It should be noted that the covariances calculated from the four times daily NCEP re-analysis data can at best capture fluctuations on the time scales of the diurnal cycle, while the GCM has a time step on the order of minutes and captures variances on time

Table 4.1: Observations

Location name	Location in coordinates	Measure-ment mission	Type of observation	# of sound-ings	# of measurements used for calculation			Time frame
EPIC Gal-apagos	(89.61W,0.9S)	EPIC	radiosonde	77	q 438	s 438	$\|\mathbf{v}\|$ 426	09/01/01 to 10/15/01
San Cris-tobal (all)	(89.61W,0.9S)	local station	radiosonde	469	q 4193	s 4193	$\|\mathbf{v}\|$ 4116	09/01/98 to 12/16/00
San Cris-tobal (April)	(89.61W,0.9S)	local station	radiosonde	30	q 263	s 263	$\|\mathbf{v}\|$ 256	04/01/99 to 04/30/99 and 04/01/00 to 04/30/00
EPIC 0N	~95W, lat<1N	EPIC	radiosonde & dropsonde	7	q 408	s 411	$\|\mathbf{v}\|$ 323	09/03/01 to 10/07/00
EPIC 2N	~95W, 1N<lat<3N	EPIC	radiosonde & dropsonde	18	q 1018	s 1020	$\|\mathbf{v}\|$ 613	09/03/01 to 10/07/00
EPIC 4N	~95W, 3N<lat<5N	EPIC	radiosonde & dropsonde	18	q 1050	s 1050	$\|\mathbf{v}\|$ 707	09/03/01 to 10/07/00
EPIC 6N	~95W, 5N<lat<7N	EPIC	radiosonde & dropsonde	19	q 1066	s 1066	$\|\mathbf{v}\|$ 636	09/03/01 to 10/07/00
EPIC 8N	~95W, 7N<lat<9N	EPIC	radiosonde & dropsonde	24	q 1371	s 1377	$\|\mathbf{v}\|$ 873	09/03/01 to 10/07/00
EPIC 10N	~95W, 9N<lat<11N	EPIC	radiosonde & dropsonde	134	q 6760	s 6762	$\|\mathbf{v}\|$ 5517	09/03/01 to 10/07/00

Table 4.1: Observations

Location name	Location in coordinates	Measure-ment mission	Type of observation	# of sound-ings	# of measurements used for calculation			Time frame
TEPPS point	(125W, 7.8N)	TEPPS	radiosonde	80	q 3437	s 3437	$\|\mathbf{v}\|$ 3350	08/10/97 to 08/23/97
Chuuk	(151.8E, 7.4N)	TOGA/ COARE	radiosonde	502	q 8435	s 8435	$\|\mathbf{v}\|$ 7366	10/31/92 to 02/28/93
Majuro	(171.4E, 7.1N)	TOGA/ COARE	radiosonde	256	q 4018	s 4025	$\|\mathbf{v}\|$ 3748	10/31/92 to 02/28/93
Funafuti	(179.2E, 8.5S)	TOGA/ COARE	radiosonde	222	q 1394	s 1394	$\|\mathbf{v}\|$ 19	10/31/92 to 02/11/93

Table 4.2: a) Mixed layer water vapor mixing ratio from sondes and the GCM

q in g kg^{-1}	location coordinates	Sonde measurements			GCM		
		mean	Σ	**Σ / mean [%]**	mean	Σ	**Σ / mean [%]**
EPIC Galapagos	(89.61W,0.9S)	11.6723	0.623599	**5.34**			
San Cristobal (all)	(89.61W,0.9S)	12.8139	1.96931	**15.37**			
San Cristobal (April)	(89.61W,0.9S)	14.8569	1.11229	**7.49**	17.2393	1.43258	**8.31**
EPIC 0N	(95W, 0N)	11.3365	0.552456	**4.87**	16.4925	1.19698	**7.26**
EPIC 2N	(95W, 2N)	12.4674	0.848899	**6.81**	16.7468	1.40419	**8.38**
EPIC 4N	(95W, 4N)	15.0099	1.17107	**7.80**	18.0374	1.17273	**6.50**
EPIC 6N	(95W, 6N)	16.8470	0.865294	**5.14**	18.6514	1.62604	**8.72**
EPIC 8N	(95W, 8N)	17.5507	1.37628	**7.84**	18.6472	1.71899	**9.22**
EPIC 10N	(95W, 10N)	17.7358	1.05075	**5.92**	18.7946	1.64247	**8.74**
TEPPS point	(125W, 7.8N)	16.4428	1.10506	**6.72**	17.2062	1.26463	**7.35**
Chuuk	(151.8E, 7.4N)	18.1406	1.47276	**8.12**	19.2255	1.74404	**9.07**
Majuro	(171.4E, 7.1N)	18.4480	1.62473	**8.81**	19.0528	1.02780	**5.39**
Funafuti	(179.2E, 8.5S)	16.9829	2.51911	**14.83**	18.6839	2.02659	**10.85**

Table 4.2: b) Mixed layer water vapor mixing ratio from the NCEP re-analysis

q in g kg^{-1}	NCEP re-analysis					
	q^*_{SST} mean	q^*_{SST} Σ	Σ / **mean [%]**	q_{1000} mean	q_{1000} Σ	Σ / **mean [%]**
EPIC Galapagos						
San Cristobal (all)						
San Cristobal (April)	24.7681	0.991238	**4.00**	17.1908	0.640302	**3.72**
EPIC 0N	24.9076	0.955385	**3.84**	17.1421	0.642354	**3.75**
EPIC 2.5N	25.1826	1.24894	**4.96**	17.3369	0.564874	**3.26**
EPIC 5N	25.4703	2.25008	**8.83**	17.6852	0.748288	**4.23**
EPIC 7.5N	25.0078	3.09689	**12.38**	18.0457	0.841863	**4.67**
EPIC 10N	25.7536	3.64739	**14.16**	17.1819	0.961935	**5.60**
TEPPS point	21.6948	1.43783	**6.63**	17.6983	0.728225	**4.11**
Chuuk	25.2100	0.343845	**1.36**	19.1620	0.512668	**2.68**
Majuro	24.6951	0.853186	**3.45**	18.5035	0.572546	**3.09**
Funafuti	26.2539	0.729096	**2.78**	18.4000	0.788957	**4.29**

Table 4.3: Mixed layer dry static energy per specific heat

$\frac{s}{c_P}$ in K	location coordinates	Sonde measurements			GCM			NCEP re-analysis			
		mean	Σ	Σ / **mean [%]**	mean	Σ	Σ / **mean [%]**	latitude	mean	Σ	Σ / **mean [%]**
EPIC Galapagos	(89.61W,0.9S)	293.168	0.761	**0.26**							
San Cristobal (all)	(89.61W,0.9S)	296.718	2.703	**0.91**							
San Cristobal (April)	(89.61W,0.9S)	299.605	1.113	**0.37**	300.303	0.818	**0.27**		299.709	0.513	**0.17**
EPIC 0N	(95W, 0N)	292.629	0.396	**0.14**	300.354	0.850	**0.28**	0N	299.408	0.522	**0.17**
EPIC 2N	(95W, 2N)	294.566	0.962	**0.33**	300.780	0.812	**0.27**	2.5N	299.850	0.441	**0.15**
EPIC 4N	(95W, 4N)	296.981	0.772	**0.26**	301.922	0.566	**0.19**				
EPIC 6N	(95W, 6N)	298.798	0.597	**0.20**	302.250	0.767	**0.25**	5N	300.455	0.555	**0.18**
EPIC 8N	(95W, 8N)	299.593	0.906	**0.30**	302.451	0.789	**0.26**	7.5N	300.828	0.525	**0.17**
EPIC 10N	(95W, 10N)	300.556	0.957	**0.32**	303.064	0.843	**0.28**	10N	300.960	0.680	**0.23**
TEPPS point	(125W, 7.8N)	300.852	0.719	**0.24**	300.551	0.659	**0.22**		299.082	0.613	**0.20**
Chuuk	(151.8E, 7.4N)	300.903	0.646	**0.21**	301.857	0.722	**0.24**		301.568	0.491	**0.16**
Majuro	(171.4E, 7.1N)	300.982	0.814	**0.27**	300.834	0.664	**0.22**		301.049	0.539	**0.18**
Funafuti	(179.2E, 8.5S)	302.048	0.844	**0.28**	302.506	0.648	**0.21**		301.520	0.516	**0.17**

Table 4.4: Mixed layer wind speed

$\|\mathbf{v}\|$ in $m\ s^{-1}$	location coordinates	Sonde measurements (all winds between 100 m and 500m)			GCM (mixed layer wind speed)			NCEP re-analysis (10 m wind speed)			
		mean	Σ	**Σ / mean [%]**	mean	Σ	**Σ / mean [%]**	latitude	mean	Σ	**Σ / mean [%]**
EPIC Galapagos	(89.61W,0.9S)	7.65731	2.10950	**27.55**							
San Cristobal (all)	(89.61W,0.9S)	5.67671	2.66565	**46.96**							
San Cristobal (April)	(89.61W,0.9S)	3.44961	1.86910	**54.18**	5.29451	1.63331	**30.85**		2.14917	1.15640	**53.81**
EPIC 0N	(95W, 0N)	7.05511	1.59779	**22.65**	5.31770	1.37186	**25.80**	0N	2.78891	1.10351	**39.57**
EPIC 2N	(95W, 2N)	7.56444	2.01400	**26.62**	5.16715	1.28676	**24.90**	2.5N	2.31852	1.13703	**49.04**
EPIC 4N	(95W, 4N)	7.79886	1.26579	**16.23**	5.93701	1.47298	**24.81**				
EPIC 6N	(95W, 6N)	6.36321	2.29888	**36.13**	7.16511	1.90613	**26.6**	5N	2.26367	1.07877	**47.66**
EPIC 8N	(95W, 8N)	5.48499	2.38296	**43.45**	6.95519	1.92839	**27.73**	7.5N	3.83604	1.55629	**40.57**
EPIC 10N	(95W, 10N)	5.74013	2.77966	**48.43**	6.89431	1.93145	**28.02**	10N	5.06772	1.65854	**32.73**
TEPPS point	(125W, 7.8N)	4.03188	2.64877	**65.70**	9.05330	1.50545	**16.63**		5.60506	1.30874	**23.35**
Chuuk	(151.8E, 7.4N)	8.44834	2.9937	**35.44**	7.33600	1.90217	**25.93**		6.05715	1.19698	**19.76**
Majuro	(171.4E, 7.1N)	8.79354	3.09957	**35.25**	9.69260	1.38733	**14.31**		7.09575	1.30392	**18.38**
Funafuti	(179.2E, 8.5S)	9.42632	2.61531	**27.74**	4.90052	1.31773	**26.89**		3.76970	1.38447	**36.73**

scales from minutes to weeks. Could it be that the variabilities on time scales shorter than the diurnal cycle are important in the GCM?

To provide a partial answer to this question, we have made an attempt to assess how well the GCM and the NCEP re-analysis capture the variability of the atmosphere as measured by radiosondes. Frequent radiosonde measurements are rare and often limited to short time periods. We have picked eleven points in the domain for which radiosonde measurements exist. Most of those measurements were made in the wrong season (i.e. fall or winter instead of April) and the number of samples is limited. Therefore, the variability obtained from those measurements should be considered to be only a very loose constraint on what we can expect from the models.

As a measure of variability, the standard deviation (Σ, to avoid confusion with the vertical coordinate σ) of the mixed layer water vapor mixing ratio q, dry static energy per specific heat s/c_p and wind speed $|\mathbf{v}|$ has been calculated at the thirteen sample points:

$$\Sigma = \sqrt{\overline{(x-\bar{x})^2}} \tag{4.5}$$

Table (4.1) lists the latitude and longitude, time period and number of radiosondes of each location. To obtain a somewhat representative mixed layer value for q, s/c_p and $|\mathbf{v}|$ from the soundings, all measurements between 100 m and 500 m above ground are included in

the sample. The actual number of measurements from all soundings for each of the variables is also listed in Table (4.1). Since some of those measurements are from neighboring layers of the same sounding, not all of the measurements are independent.

The mixed layer dry static energy for the NCEP re-analysis is calculated from temperature and geopotential height at 1000 hPa. The 10 m winds are taken as mixed layer winds. For the water vapor mixing ratio, both q calculated from relative humidity and temperature at 1000 hPa and the saturation mixing ratio at SST are considered. They are denoted by q_{1000} and q^*_{SST} respectively. Since the NCEP re-analysis data is saved every six hours, there are 120 measurements per variable and location. The GCM saved the variables every hour, so the sample size is 720 for each variable and location.

During the East Pacific Investigation of Climate (EPIC), the ship Ronald H. Brown stayed for about a week at (95° W, 10° N) and then traveled along the 95° W median south to the Galapagos Islands (Leg 1). At the same time, radiosondes where dropped from an aircraft along the 95° W median from the equator to 10° N. All sondes, ship-launched and dropped from the aircraft, were divided into two-degree latitude bins and compared to closest GCM cells at 0° N, 2° N, 4° N, 6° N, 8° N and 10° N. The re-analysis data comes on a 2.5° x 2.5° grid, so the points at 0° N, 2.5° N, 5° N, 7.5° N and 10° N were picked for the NCEP data.

Both models have too coarse a resolution to resolve small scale disturbances, such as gust fronts. Therefore, we should expect the sonde variability to be somewhat larger

than the models' variability. Considering the uncertainties in the observations, both models do fairly well.

The largest variability of q can be found at San Cristobal for all soundings spanning over two years. This should not be surprising, since the soundings range over seasons and years. The subset for April 1999 and 2000 varies only half as much. q_{1000} from the NCEP re-analysis has slightly lower ratio of standard deviation to mean than the observations. q^*_{SST} varies a lot in the ITCZ (EPIC Leg1), but is otherwise rather quiet.

The standard deviation of s/c_p is in the same range for the GCM and the observations. The NCEP re-analysis gives slightly smaller values, again. All locations have similar variabilities.

Comparing wind speeds from sondes, the GCM and the re-analysis is problematic. The wind can change significantly over short vertical distances in the PBL, and the winds compared here are not necessarily representative of the actual mixed layer winds. For the re-analysis, the 10 m winds were used, the GCM gives us the mixed-layer winds as calculated by its own routines, and the winds from the radiosonde measurements contain all winds between 100 m and 500, above ground. Keeping this caveat in mind, the mean wind speeds of the GCM and the observations lie mostly between $5\ \mathrm{m\,s^{-1}}$ and $9\ \mathrm{m\,s^{-1}}$. The re-analysis' mean wind speeds range primarily between $2\ \mathrm{m\,s^{-1}}$ and $7\ \mathrm{m\,s^{-1}}$. The standard deviation is largest for the observations (above $2\ \mathrm{m\,s^{-1}}$ at almost all locations)

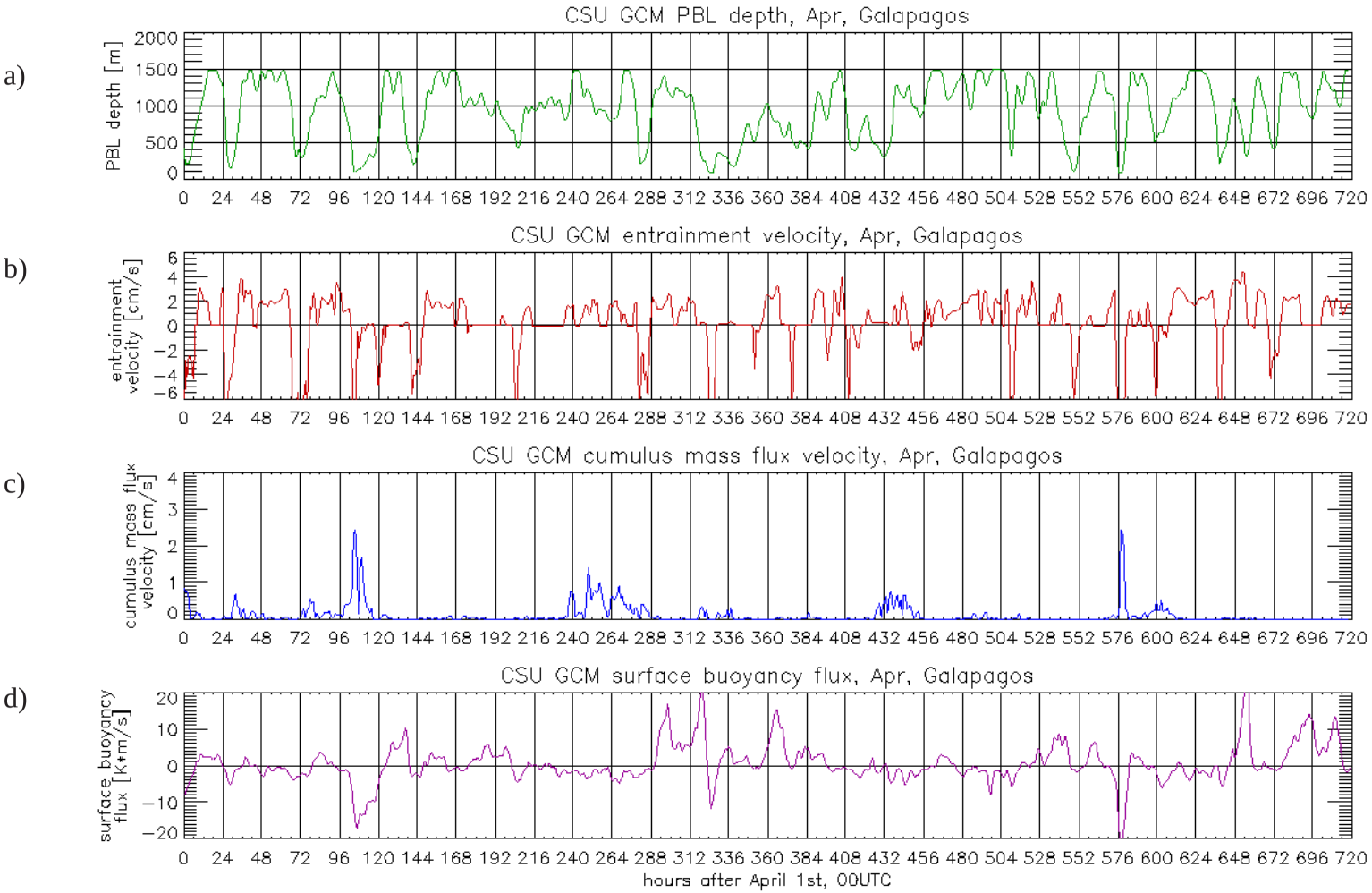

Figure 4.19: Time series of GCM a) entrainment velocity, b) cumulus mass flux velocity, c) PBL depth and d) surface buoyancy flux at the Galapagos location (~90W,1S) for the sample month. The vertical lines are 24 hour markers at 00 UTC.

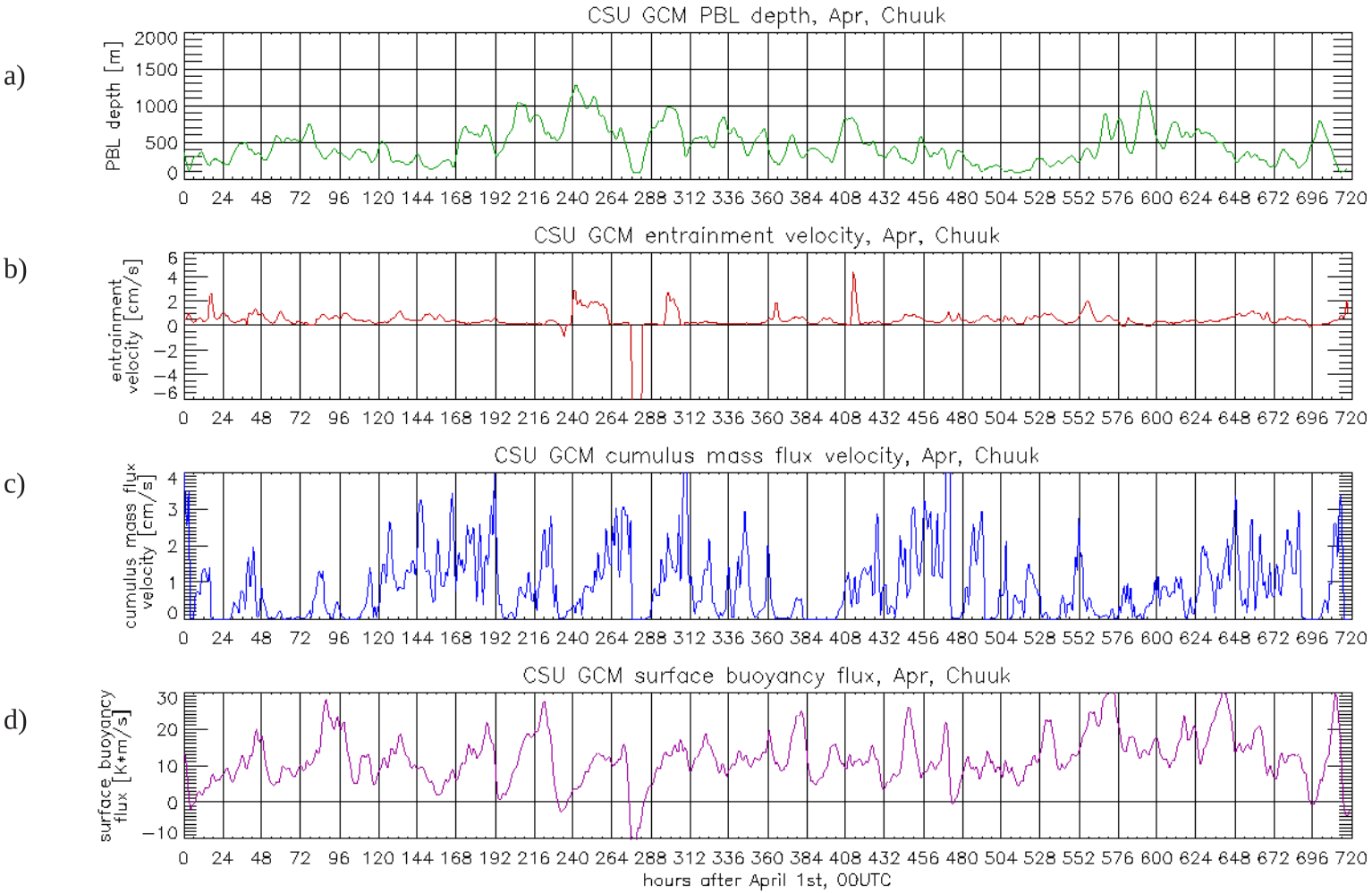

Figure 4.20: Time series of GCM a) entrainment velocity, b) cumulus mass flux velocity, c) PBL depth and d) surface buoyancy flux at the Chuuk location (~152E,7N) for the sample month. The vertical lines are 24 hour markers at 00 UTC.

and smallest for the re-analysis (around 1.5 $m\ s^{-1}$) with the GCM in the middle (around 1.8 $m\ s^{-1}$).

Overall, the re-analysis seems to slightly underestimate the variability of all three fields compared to both the observations and the GCM. However, as mentioned above, we'd expect the models to have somewhat lower variabilities than can be found in the observations. The GCM, having variabilities comparable to the observations, might therefore have a tendency for too large variability. On the other hand, the GCM can capture more variability on short time periods than the re-analysis. Spectral analysis can help determine at what time scales most of the variability lies.

The power spectra (not shown) show that most of the variables (water vapor mixing ratio and potential temperature in the mixed layer and above the PBL top, mixed layer wind speed, PBL depth, entrainment velocity) have generally high power at low frequencies (time periods longer than six hours) and low power at high frequencies. There are no systematically preferred frequencies (i.e. peaks). The exception is the cumulus mass flux, which shows significant spectral peaks around 7.2 hours, 5.2 hours and 3.5 hours in most of the locations in convective regions. This may well have to do with the convective scheme's time scale. Overall it appears as though the GCM's power lies mostly in time scales that can be resolved in the NCEP re-analysis data. Therefore, the larger variabilities of the GCM compared to the re-analysis are likely not due to the difference in time resolution.

a)

b)

c)

d)

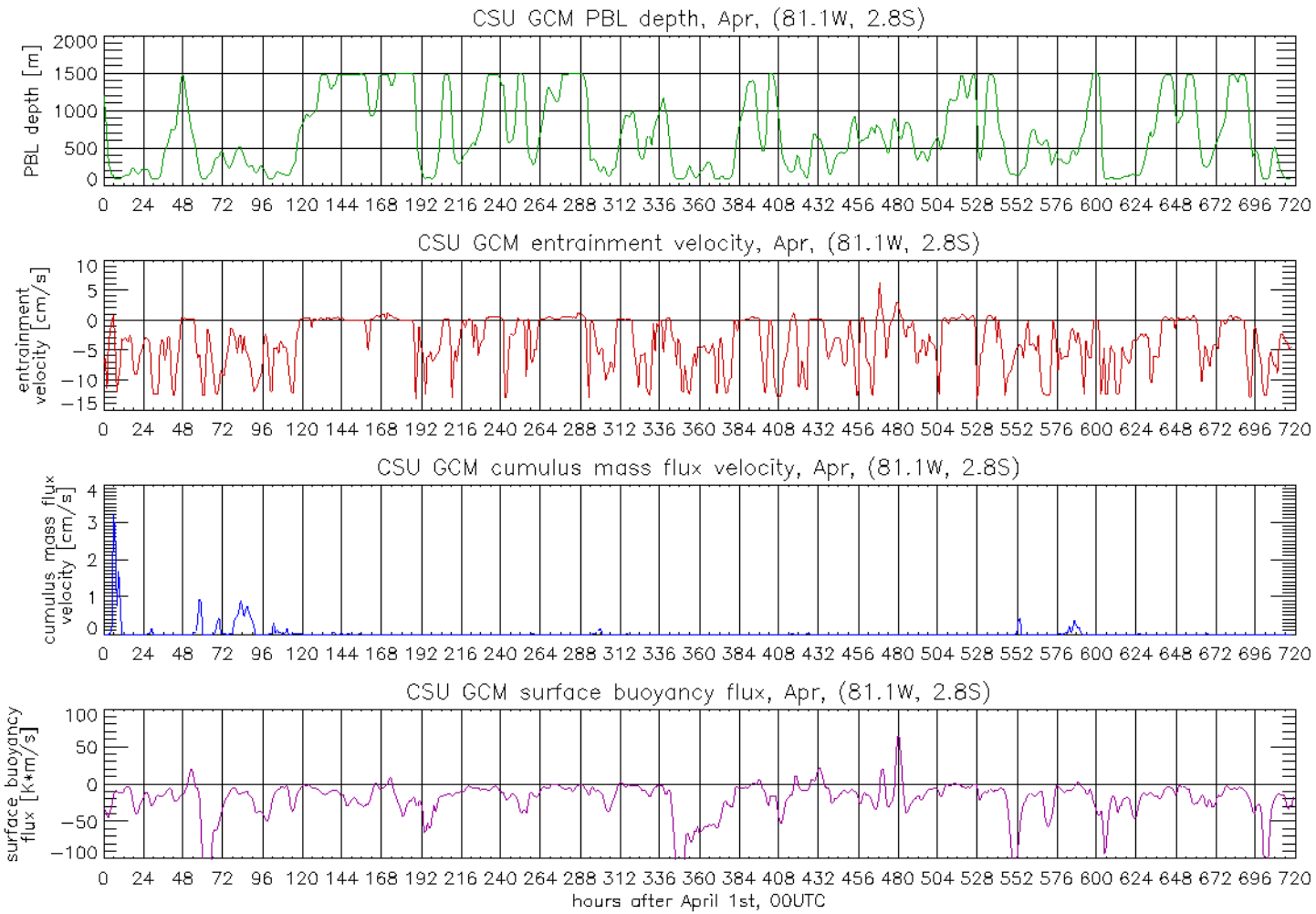

Figure 4.21: Time series of GCM a) entrainment velocity, b) cumulus mass flux velocity, c) PBL depth and d) surface buoyancy flux at the coastal location (81.1W, 2.8S) for the sample month. The vertical lines are 24 hour markers at 00 UTC.

A look at the actual time series of entrainment velocity, cumulus mass flux velocity and PBL depth shows a lot of variability in all three variables. Fig. 4.19 and Fig. 4.20 show the Galapagos and Chuuk locations, Fig. 4.21 a location at a GCM grid cell center one cell removed from the south American coast at 81.1° W, 2.8° S. The Galapagos and Chuuk plots are good representatives of all non-convective and convective locations, respectively. The third location is chosen in an area with negative entrainment velocity. The GCM predicts the PBL top, i.e. the top of the turbulent layer. We should keep in mind that the definition used to determine the PBL top from soundings, where the base of the temperature inversion is taken to be the top of the PBL, is different. The PBL depth at the Galapagos location shows large variations on time scales of a day or so. A distinct signature of a diurnal cycle can only be found for some days and is not prevalent over the whole month. The PBL depth varies by as much as 1300 m in 12 hours. This is much more than can be found in the soundings of the EPIC cruise, Leg 2. Here, the PBL depth varies by approximately 300 m over the same time period (see Chapter 5). However, it is possible that the turbulent mixing might collapse while the temperature inversion persists. This would not show up in the PBL depth as analyzed from the soundings, but the GCM would respond with a collapse of the PBL.

The cumulus mass flux is overall small at the Galapagos islands, as should be expected. There are four larger convective events over the sample month. While the PBL depth tends to be shallow during those events, the PBL is also shallow during periods without convection.

The entrainment velocity varies a lot and is frequently negative, up to -6 cm s^{-1}. A possible explanation for this behavior is the following: When warm, moist air is advected over the cold ocean, the surface buoyancy flux becomes smaller or even negative and the turbulence in the PBL collapses to whatever turbulence the wind shear can support. Since the PBL top in the GCM is defined as the top of the turbulent layer, the PBL has to become shallower. If no convection takes place, the cumulus mass flux is unable to remove mass from the PBL. The entrainment mass flux facilitates the deflation of the PBL. At the Galapagos location, the surface buoyancy flux is close to zero most of the time, and frequently negative. The larger negative peaks in the buoyancy flux always coincide with large negative entrainment velocities. This supports the mechanism outlined above. However, the entrainment velocity is strongly negative also in some cases where the surface buoyancy flux is close to zero.

At the Chuuk location, the PBL is overall shallower. The cumulus mass flux velocity is larger, mostly up to 3 cm s^{-1}. The entrainment velocity is rather small, around 1 cm s^{-1}, but positive most of the time. Overall, the mass flux velocities seem to be more physically representative in the convective regions. Here, convection takes place almost all the time and the cumulus mass flux deflates the PBL whenever necessary. The entrainment is mostly positive and therefore describes actual entrainment, not a collapse of the PBL. The one large negative peak in entrainment velocity around hour 275 coincides with a large negative surface buoyancy flux.

At the coastal location (81.1° W, 2.8° S), the PBL depth often hits the upper and lower limits set by the GCM's PBL scheme. Almost no convection takes place, hence the entrainment mass flux deflates the PBL. In the timeseries, every major collapse of the PBL is accompanied by a significantly negative entrainment velocity. There are time periods however, when the entrainment mass flux keeps deflating the PBL even though the PBL top is very low (e.g. hours 336 through 384). The surface buoyancy flux is also negative and very large throughout most of the month and can be loosely linked, as in the Galapagos location, with a collapse of the PBL. It seems the surface buoyancy flux is the more important problem here. The PBL scheme can hardly be expected to work properly when the surface buoyancy flux is strongly negative.

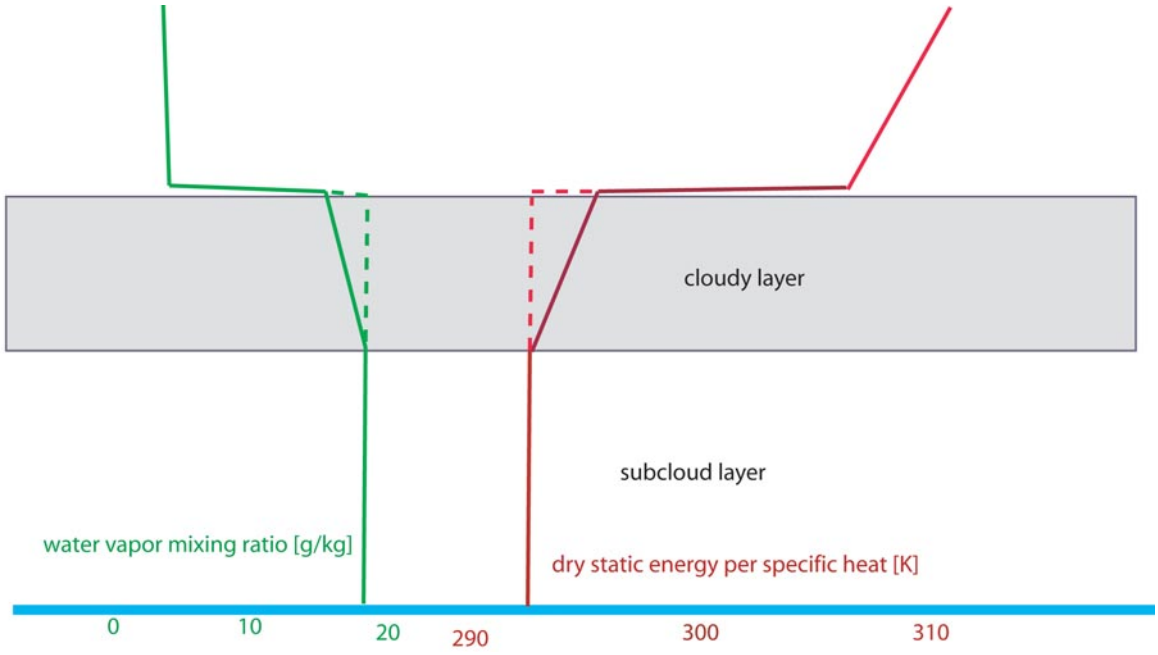

Figure 4.22: Schematic of water vapor mixing ratio (green) and dry static energy per specific heat (red) profiles for a stratocumulus topped PBL. Dashed lines indicate the profiles for the mixed layer assumption. Solid lines show actual profile.

4-C-1 Summary

The comparison of the mixed layer scheme as implemented in the GCM with the application of the MLM to monthly mean re-analysis data shows that the monthly mean and steady state assumptions certainly contribute to the discrepancies between PBL properties of the GCM and the MLM, but are likely not the only factors responsible. While covariances contribute significantly to the PBL properties in the GCM, particularly along the ITCZ, covariances in the NCEP re-analysis runs are rather small and have little impact on the PBL properties. The only slightly larger variabilities in the GCM don't seem to be significant enough to account for the strong impact that the covariances have in the GCM compared to the MLM.

4-D: Sensitivity to the formulation of the dry static energy and water vapor mixing ratio jump at the top of the PBL

What other factors impact the performance of the mixed layer scheme, and how could the MLM be further improved? The MLM assumes that dry static energy and water vapor mixing ratio are well mixed throughout the boundary layer. In fact, those two variables are not truly conserved in a stratocumulus-topped boundary layer.

While moist static energy and total water vapor mixing ratio are conserved in the subcloud as well as the cloud layer of the PBL, the dry static energy increases in the cloud layer due to the formation of cloud water droplets. The water vapor mixing ratio decreases for the same reason (Fig. 4.21). The model originally proved to be rather insensitive to the exact choice of pressure levels on which dry static energy and water vapor mixing ratio

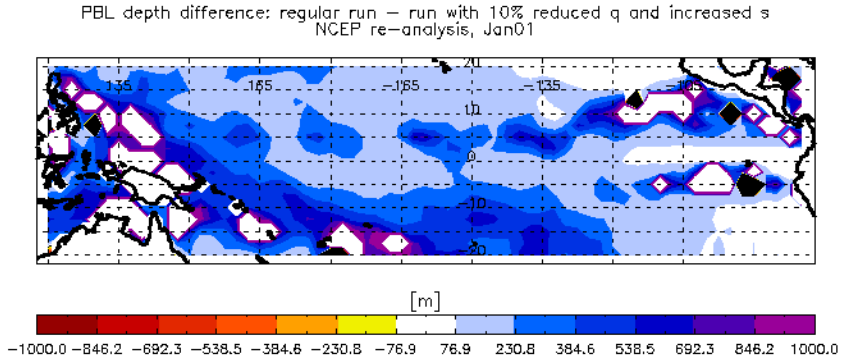

Figure 4.23: a) Difference in PBL depth between regular MLM run with monthly mean input from NCEP re-analysis data for January 2001 and a run where the mixed layer value of q is reduced by 10% and the mixed layer value of s is increased by $L_C \cdot 0.1 q_B$. Regions with above-scale values are white.

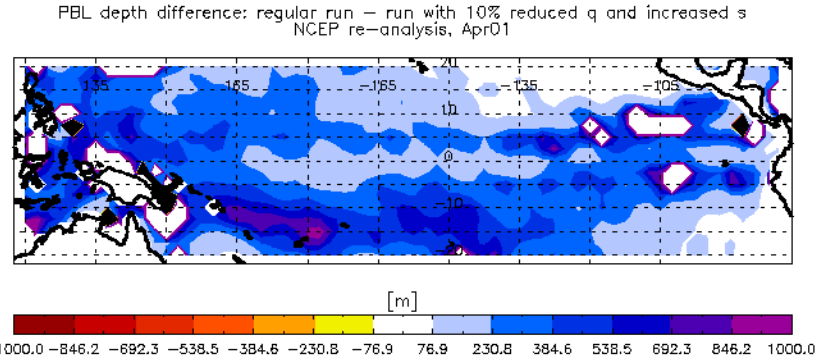

Figure 4.23: b) Same as in a) for April 2001

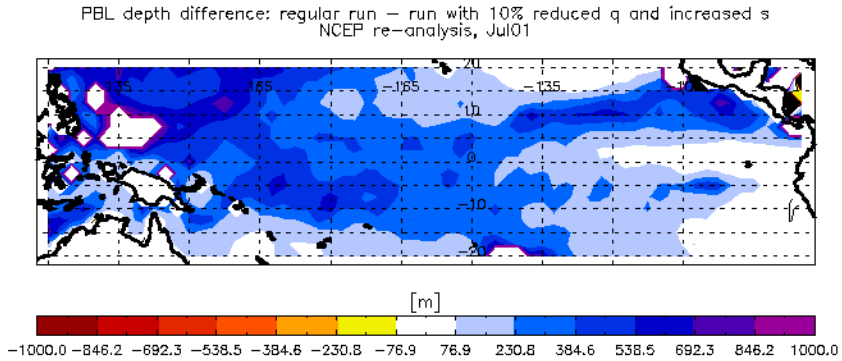

Figure 4.23: c) Same as in a) for July 2001

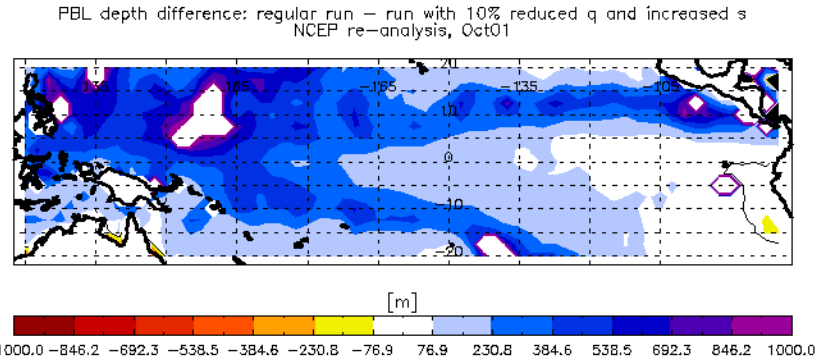

Figure 4.23: d) Same as a) for October 2001

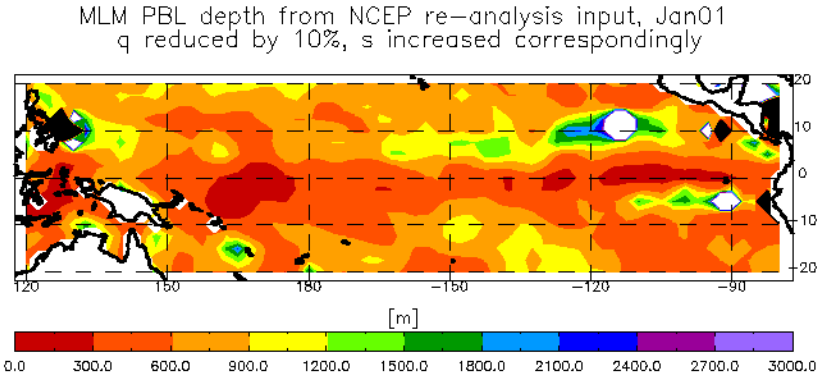

Figure 4.24: a) PBL depth from MLM run with monthly mean input from NCEP re-analysis data for January 2001. The mixed layer value of q is decreased by 10% and the mixed layer value of s is increased by $L_C \cdot 0.1 q_B$. Regions with above-scale values are white, with below-scale values are black.

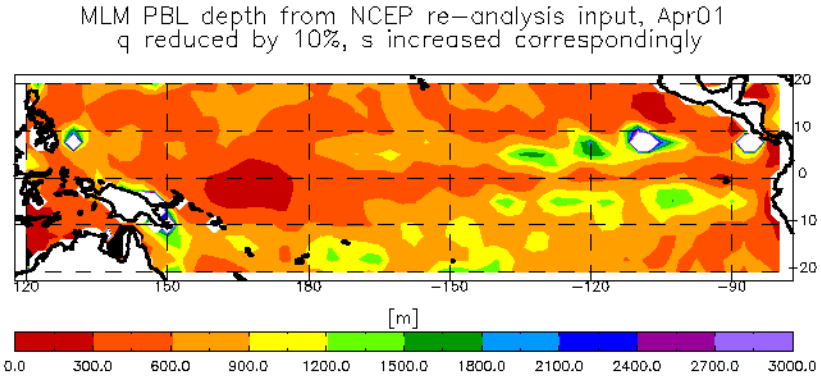

Figure 4.24: b) Same as a) for April 2001

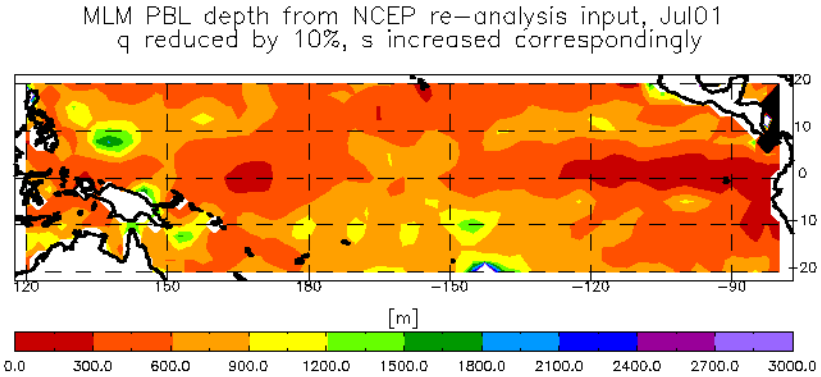

Figure 4.24: c) Same as a) for July 2001

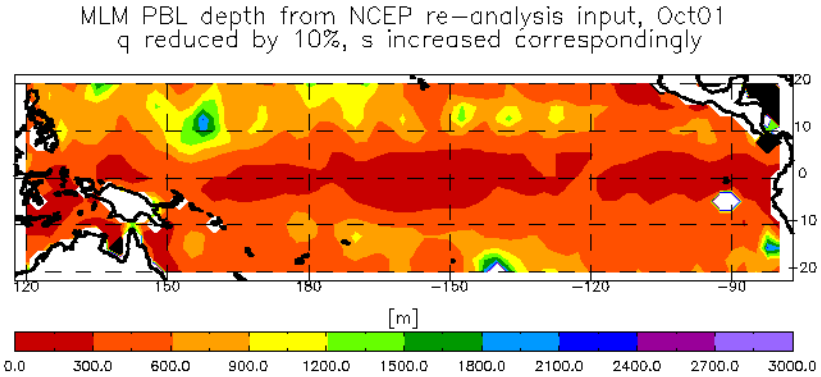

Figure 4.24: d) Same as a) for October 2001

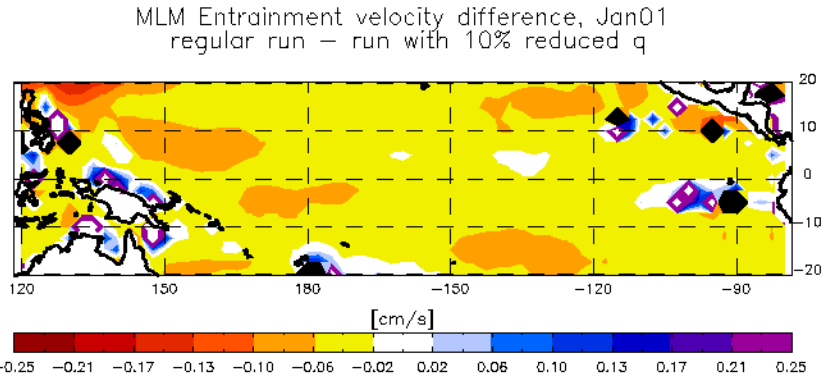

Figure 4.25: a) Difference in entrainment velocity between regular MLM run with monthly mean input from NCEP re-analysis data for January 2001 and a run where the mixed layer value of q is reduced by 10% and the mixed layer value of s is increased by $L_C \cdot 0.1 q_B$. Regions with above-scale values are white.

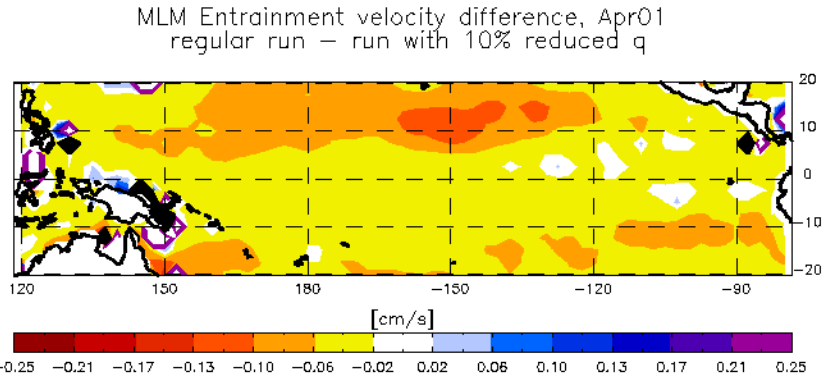

Figure 4.25: b) Same as a) for April 2001

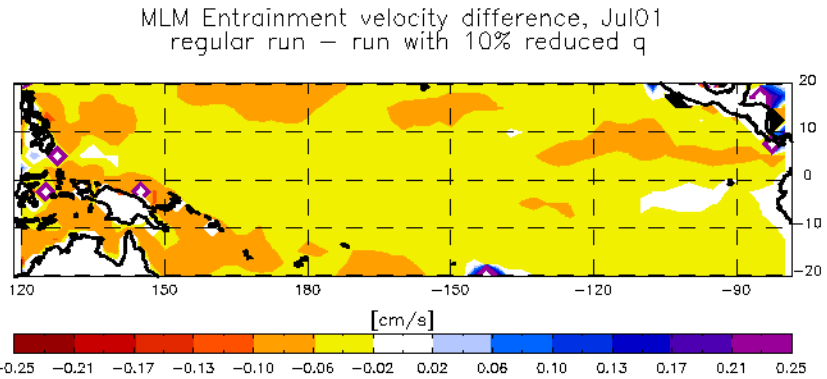

Figure 4.25: c) Same as a) for July 2001

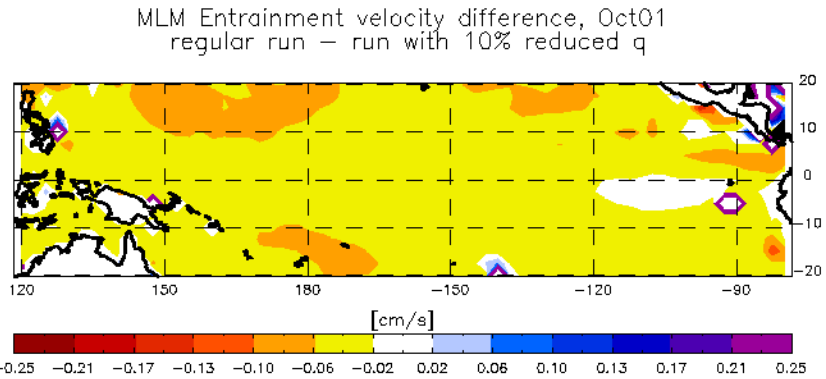

Figure 4.25: d) Same as a) for October 2001

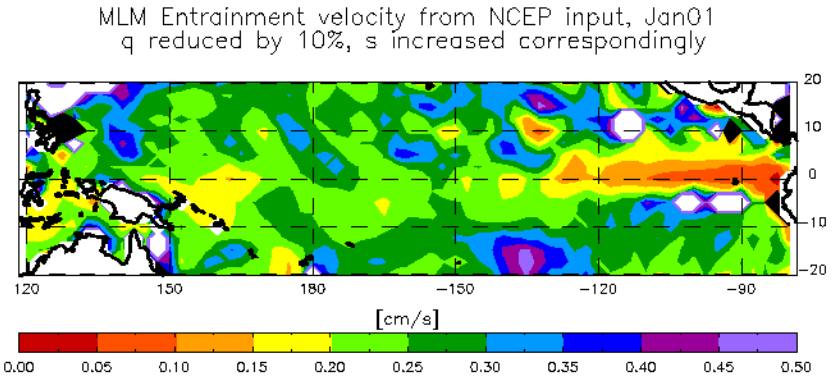

Figure 4.26: a) Entrainment velocity from MLM run with monthly mean input from NCEP re-analysis data for January 2001. The mixed layer value of q is decreased by 10% and the mixed layer value of s is increased by $L_C \cdot 0.1 q_B$. Regions with above-scale values are white, with below-scale values are black.

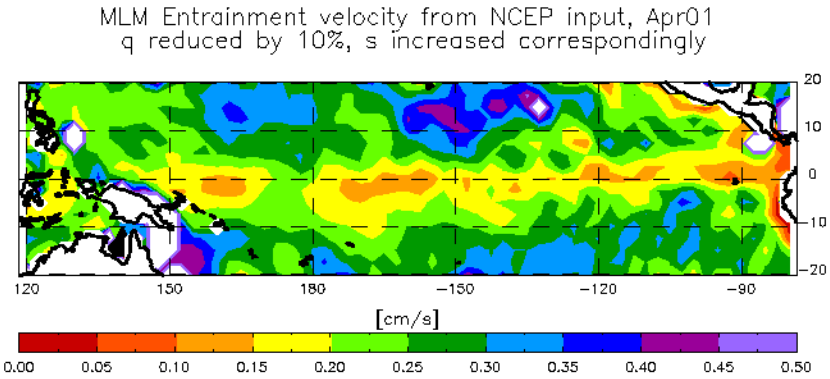

Figure 4.26: b) Same as a) for April 2001

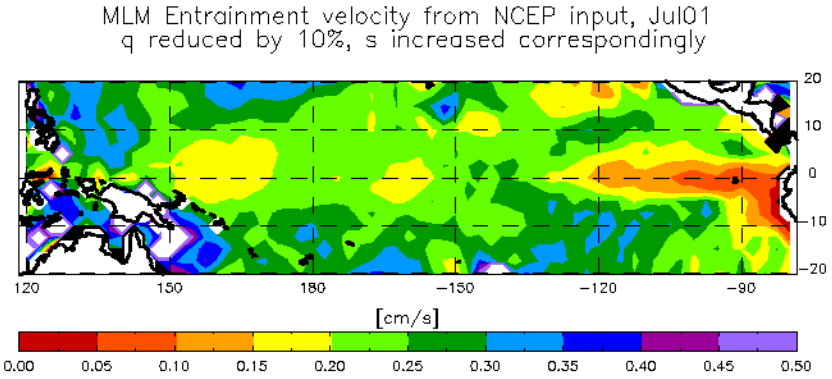

Figure 4.26: c) Same as a) for July 2001

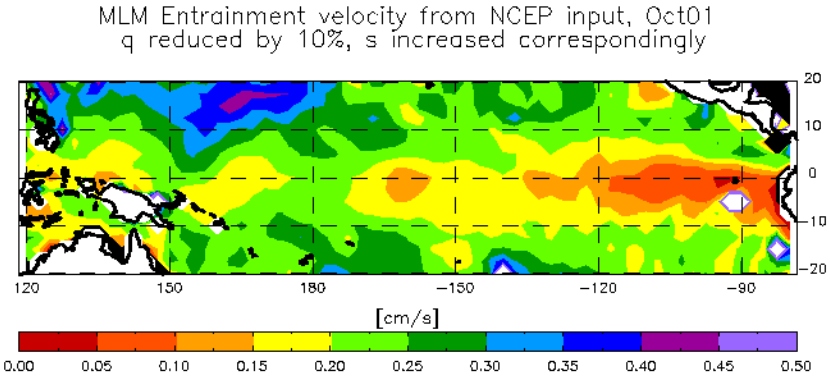

Figure 4.26: d) Same as a) for October 2001

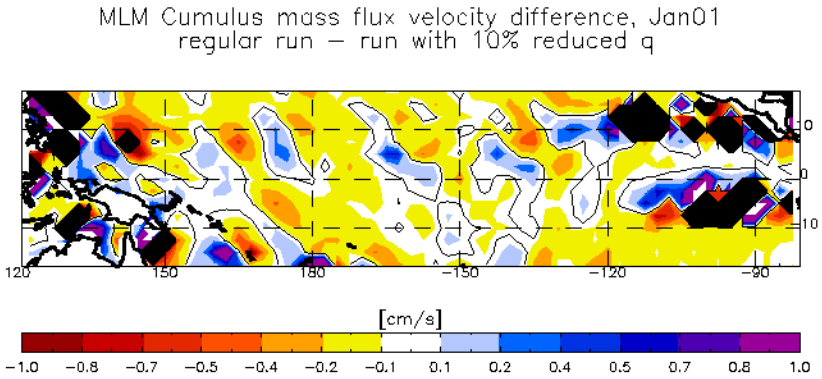

Figure 4.27: a) Difference in cumulus mass flux velocity between regular MLM run with monthly mean input from NCEP re-analysis data for January 2001 and a run where the mixed layer value of q is reduced by 10% and the mixed layer value of s is increased by $L_C \cdot 0.1 q_B$. Regions with above-scale values are white, with below-scale values are black.

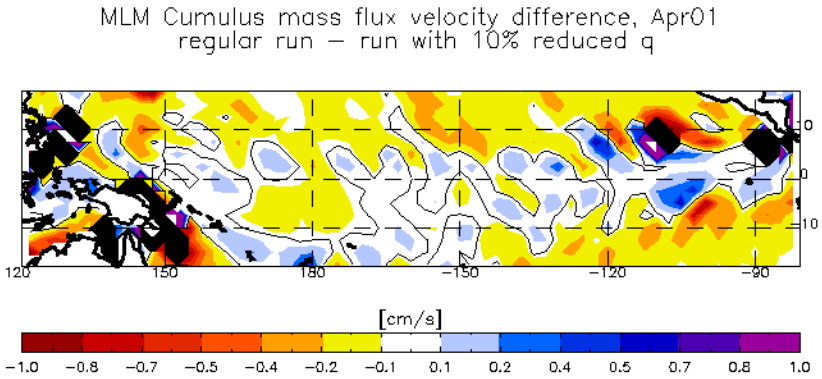

Figure 4.27: b) Same as a) for April 2001

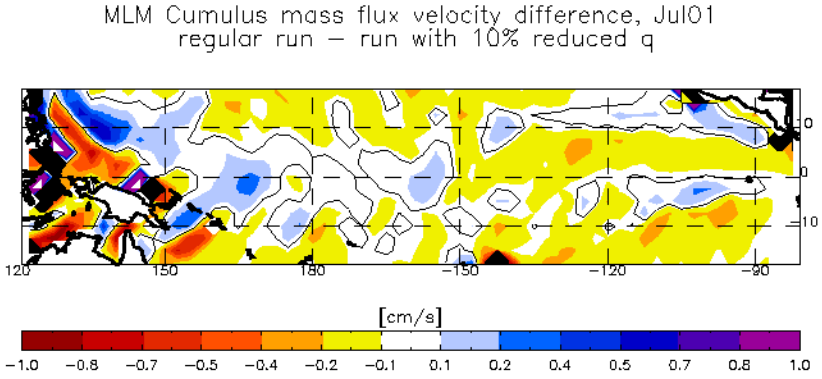

Figure 4.27: c) Same as a) for July 2001

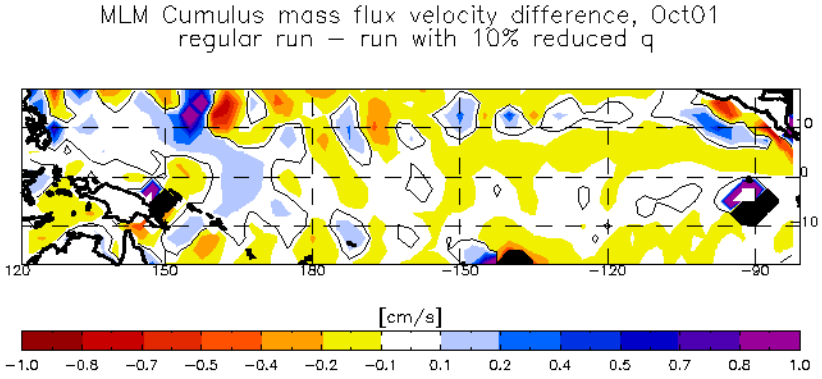

Figure 4.27: d) Same as a) for October 2001

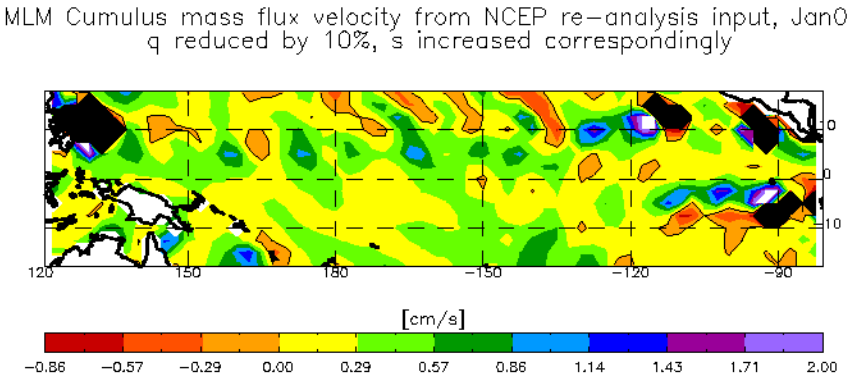

Figure 4.28: Cumulus mass flux velocity from MLM run with monthly mean input from NCEP re-analysis data for January 2001. The mixed layer value of q is decreased by 10% and the mixed layer value of s is increased by $L_C \cdot 0.1 q_B$. Regions with above-scale values are white, with below-scale values are black.

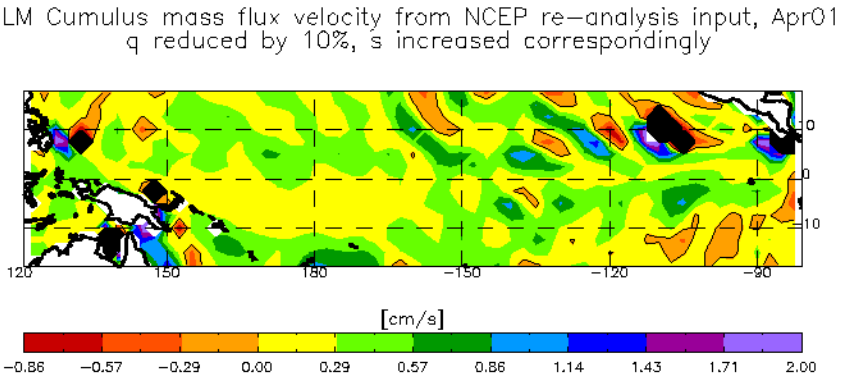

Figure 4.28: Same as a) for April 2001

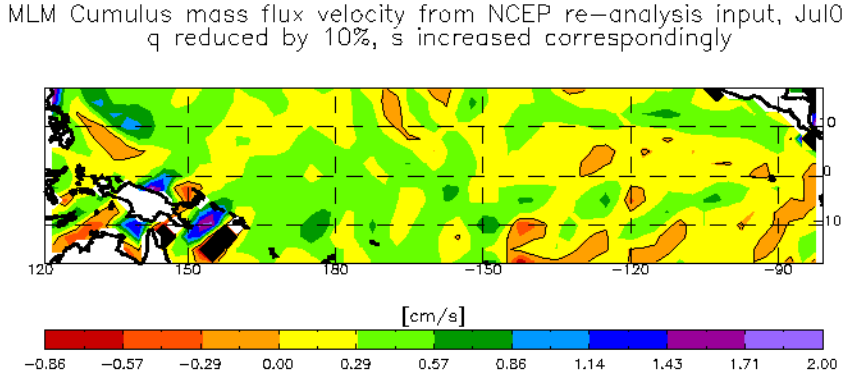

Figure 4.28: c) Same as a) for July 2001

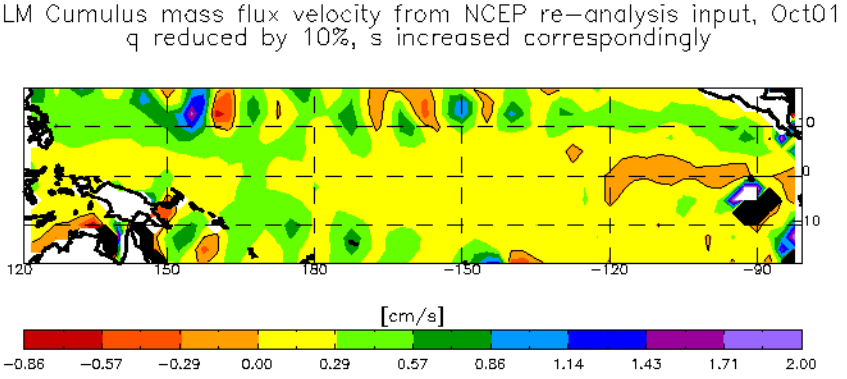

Figure 4.28: d) Same as a) for October 2001

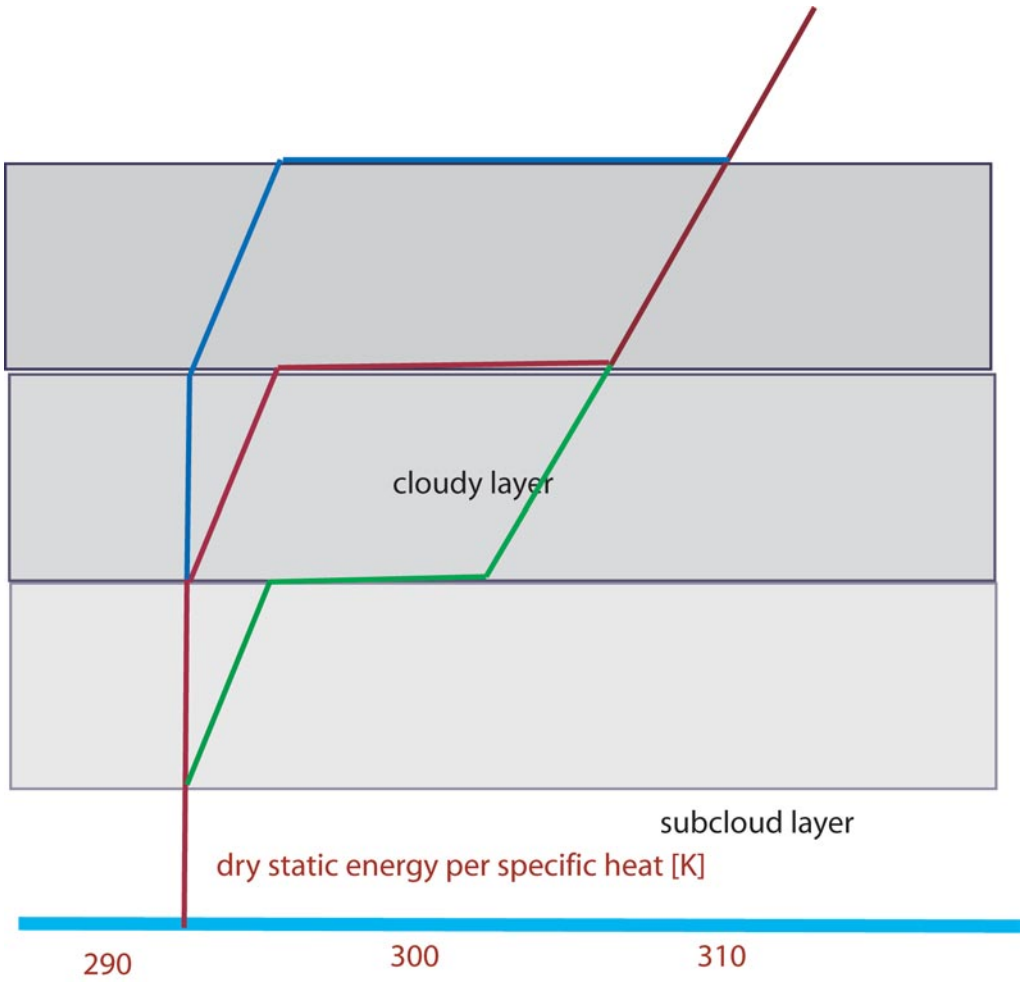

Figure 4.29: Schematic dry static energy profile for cloudy layers and PBL tops at different heights. Green: shallow PBL, red: medium PBL, blue: deep PBL

above and in the PBL were defined. However, when choosing the pressure levels, the mixed layer values q_B and s_B always changed in the same direction (i.e. picking a lower atmospheric level increased q_B as well as s_B, picking a higher level decreased both), not in opposite directions (i.e. decreasing q_B, but at the same time increasing s_B). The four NCEP months were re-run with a mixed layer water vapor mixing ratio reduced by 10% in the entrainment terms. I. e. the term

$$w_E(q_H - q_B) \tag{4.6}$$

changes into

$$w_E(q_H - 0.9 \cdot q_B) \tag{4.7}$$

The dry static energy in the entrainment terms is increased by the corresponding latent heat release, i.e. the expression

$$w_E(s_H - s_B) \tag{4.8}$$

becomes

$$w_E[s_H - (s_B + L_C(0.1 \cdot q_B))]. \tag{4.9}$$

This effectively changes the jumps in s and q across the PBL top in the entrainment terms. The model results show a significantly reduced PBL depth in areas of convection, and slight increases in the PBL depth off the Chilean coast in October. Perhaps the most significant improvement is the reduction of spots with far too deep PBL (> 3000 m) in the convective regions. The PBL depth is now more uniform over the domain and somewhat smaller than in the original runs (on the order of 600 m over most of the domain).

The entrainment velocity increases fairly uniformly by about half a mm s^{-1} over the whole domain. The exceptions are those grid points where the PBL was very deep

(>3000 m) initially. Here, the entrainment velocity is reduced. This tends to even out the spots with very large entrainment velocities that coincide with very large PBL depths.

The increase in entrainment velocity combined with a smoother PBL depth field lead to a noise reduction for the cumulus mass flux velocity. The areas with negative cumulus mass flux velocities are smaller in all months. The cumulus mass flux velocity still does not clearly mark areas or bands of deep convection, but in October, there is a tendency for lower velocities in the south-east Pacific, and higher values north of the equator and in the west Pacific.

Switching the reduced q_B back to the original value of q_B, but retaining the increase in s_B shows that most of these improvements are due to the change in dry static energy, not moisture.

The choice of a 10% water vapor mixing ratio decrease is somewhat arbitrary. A less arbitrary way of looking at the magnitude of the jump across the PBL top is as a function of PBL depth. Since changes in q have little effect on the PBL depth, only the changes in s are considered from here on. As Fig. 4.29 illustrates, the jump in dry static energy increases for deeper PBLs. Due to the small influence of the Coriolis force in the tropics, large horizontal pressure and temperature gradients cannot be supported. The temperature (and therefore also the dry static energy) of the free atmosphere is primarily determined by the saturated moist adiabate in deep convective regions and is horizontally fairly uniform all over the domain. Assuming a well mixed boundary layer, a deeper PBL

will result in an effectively larger dry static energy jump across the PBL top (blue). A shallower PBL would tend to have a smaller jump (green).

In order to account for this functionality, the model was re-run with a dry static energy jump linearly depending on height. Three ways of implementing this dependency were tested: 1) s_H a linear function of height with fixed s_B; 2) s_B a linear function of height with fixed s_H; 3) $s_H - s_B$ a linear function of height. The results for methods 1) and 2) are very similar to each other and to the results for a 10% reduction (increase) in q_B (s_B). Method 3) is more problematic because very low PBL depths can lead to negative jumps at the PBL top. Method 2) works somewhat better than method 1); when calculated iteratively, it converges faster and is more effective at reducing the spots with unreasonably large PBL depths.

The original choice of pressure levels for s_B and s_H assumed that the PBL top would be located somewhere between 1000 m and 1500 m, based on EPIC soundings and general observations of a temperature inversion around 850 hPa in subtropical regions. Dry static energy profiles calculated from EPIC radiosonde measurements show an increase in s/c_P of ~2K per 500 m above the PBL top. In Method 2), s_B is defined as follows:

$$s_B = s_0 + \varphi_s H \tag{4.10}$$

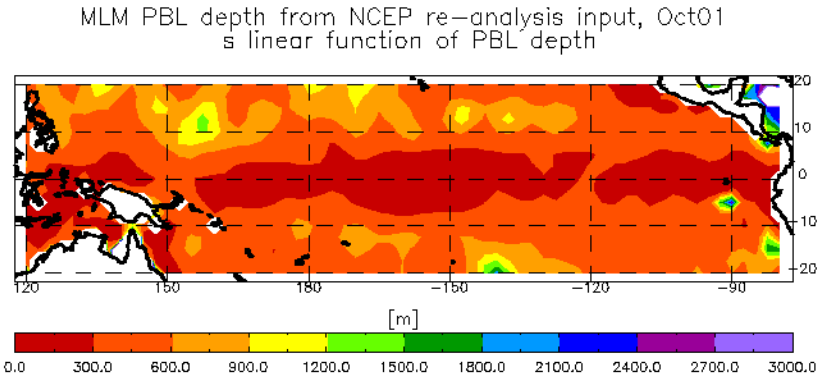

Figure 4.30: PBL depth for MLM run with mixed layer value of dry static energy a function of PBL depth. Black indicates areas of below-scale values

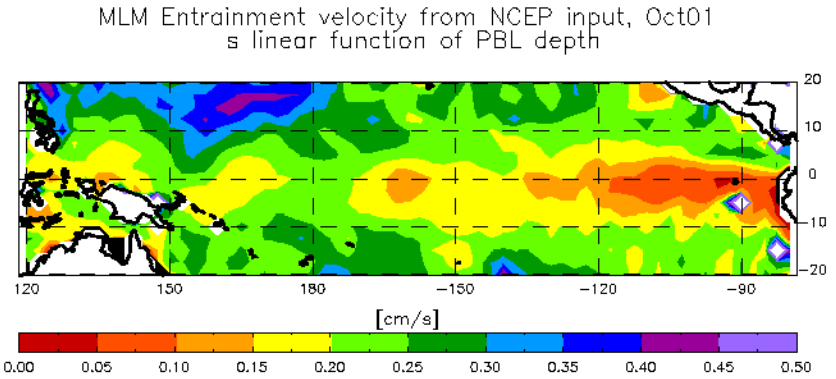

Figure 4.31: Entrainment velocity for MLM run with mixed layer value of dry static energy a function of PBL depth. Black indicates areas of below-scale values

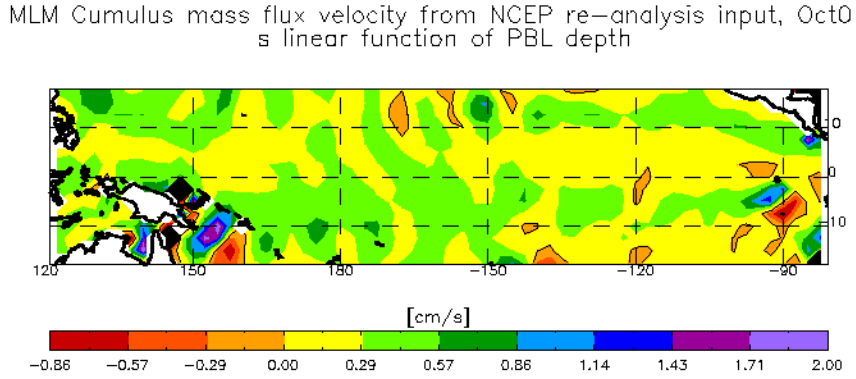

Figure 4.32: Cumulus mass flux velocity for MLM run with mixed layer value of dry static energy a function of PBL depth. Black indicates areas of below-scale values. The black contour is the zero contour.

where $\varphi_s = \frac{0.01 \cdot s_0}{2000}$ and s_0 is the original mixed layer value for dry static energy. The linear factor φ_s effectively adds 1% of the original mixed layer value ($\Delta(s_0/c_P) \approx 2-3K$) to s_B at a PBL depth of 2000 m. The results are not very sensitive to the exact choice of this factor. This linear dependency leads to a quadratic equation in PBL depth H when solving the system of equations. Solving the equation analytically produces two solutions for H:

$$H^{plus} = -\frac{A}{2} + \sqrt{\left(\frac{A}{2}\right)^2 - B} \tag{4.11}$$

and

$$H^{minus} = -\frac{A}{2} - \sqrt{\left(\frac{A}{2}\right)^2 - B} \tag{4.12}$$

where

$$A = \frac{(q_H - q_B)(\mathbf{v}_{hB} \cdot \nabla s_B) - (s_H - s_B)(\mathbf{v}_{hB} \cdot \nabla q_B) - EVP \cdot \varphi_s + \gamma(q_H - q_B)}{\varphi_s(\mathbf{v}_{hB} \cdot \nabla q_B)} \tag{4.13}$$

and

$$B = \frac{EVP(s_H - s_B) - SH(q_H - q_B)}{\varphi_s(\mathbf{v}_{hB} \cdot \nabla q_B)} \tag{4.14}$$

In those cases where only one of the solutions is positive, the positive solution is

picked as the one with physical meaning. In cases where both H^{plus} and H^{minus} are positive, H^{plus} is always significantly larger than H^{minus} (often on the order of 10 km). Therefore, the smaller solution (H^{minus}) is picked in this case.

Solving the quadratic equation iteratively with the unchanged s_B and s_H as first guesses leads to the same solution in approximately five iterations at the majority of grid points. In the exceptions, the iteration converges to the negative solution.

Since the results from method 2) are so similar to Fig. 4.23 through Fig. 4.28, only the results for the sample month October are shown in Fig. 4.30 a) through c). For the plots, the solutions from the analytically solved equation are used.

Considering the very first version of the MLM with fixed radiative cooling and dry static energy, the dependency of these two parameters on PBL depth is essential for the diagnosis of a finite, positive PBL depth, entrainment velocity and mass flux velocity of reasonable magnitude. Even as simple a relationship as a linear function improves the model significantly.

4-D-1 Summary

The MLM shows a sensitivity to the jump of dry static energy and water vapor mixing ratio across the PBL top. Following the concept depicted in Fig. 4.29, deeper mixed layers should have larger jumps across the PBL top. Implementing a simple linear functionality to that effect improves the MLM output such that the PBL depth field and

entrainment velocity field are smoother, and the areas of negative cumulus mass flux velocity are reduced. The cumulus mass flux velocity field starts showing the pattern of a southern ITCZ in the east Pacific, however, and the PBL depth is becomes very low.

Chapter 5: Comparison to Available Observations

In this chapter, we present some of the available observations on PBL depth over the tropical Pacific and compare them to the MLM's output.

5-A: Observations from soundings

The advantages of sounding data are their high vertical resolution and, in some cases, good temporal resolution (~3 hours). The disadvantages are that there are very few permanent sounding sites in the domain discussed in this thesis, and measurement missions usually have a limited duration (weeks to months). Therefore, a comparison between sounding data and global (or domain) coverage monthly mean data is difficult.

5-A-1 EPIC

During the East Pacific Investigation of Climate (EPIC), the ship Ronald H. Brown traveled from approximately 95°W, 12°N along the 95th meridian to the Galapagos Islands and from there to Arica, Chile, releasing radiosondes every 6 hours (see cruise track figures in Chapter 2: Fig. 2.4 and Fig. 2.5). Over roughly the same period of time, the NSF C-130 aircraft flew over the same general area as the fist leg of the Ronald H. Brown's cruise track, dropping 181 sondes every degree latitude between the equator and ~12° N.

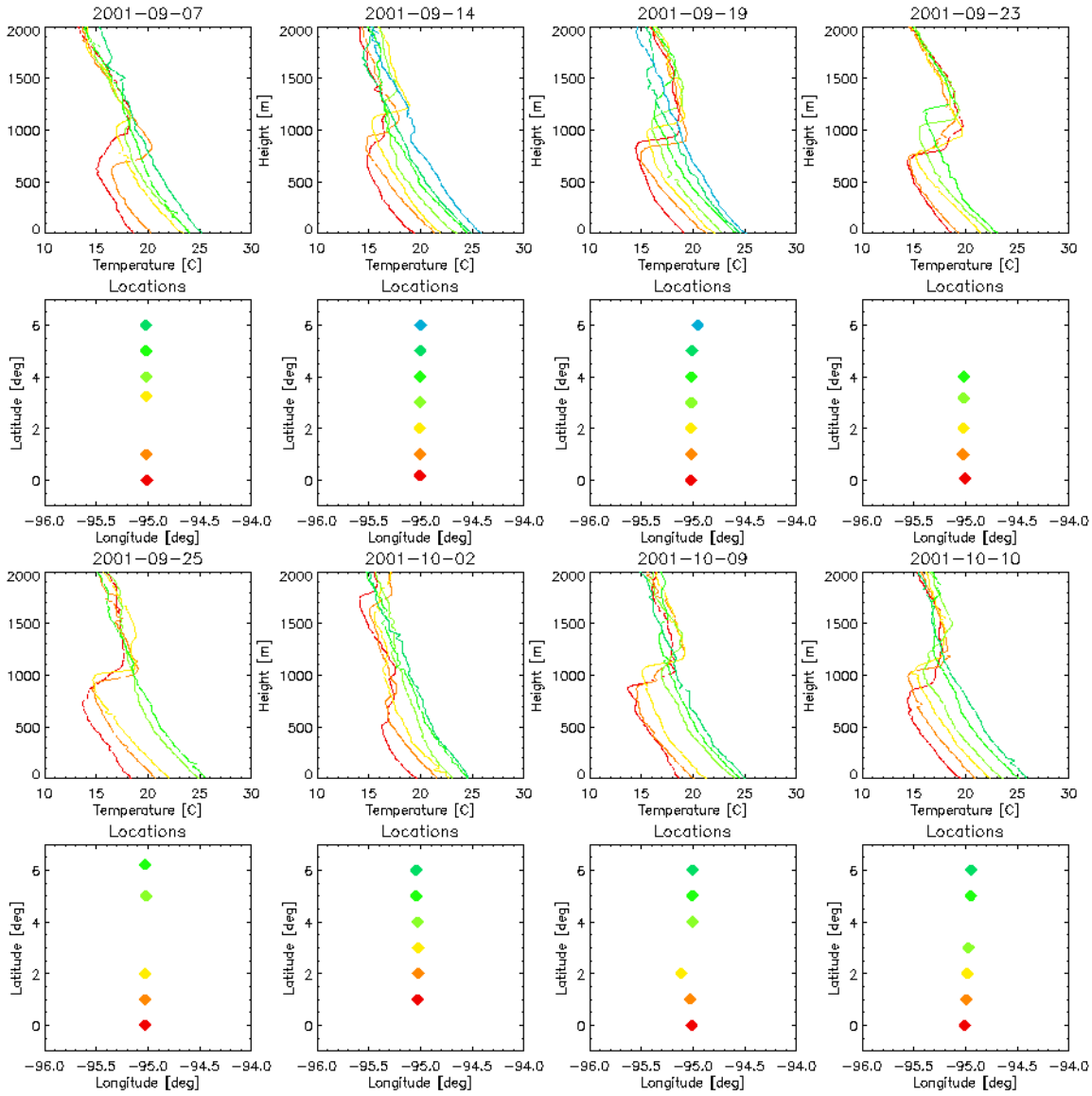

Figure 5.1: Temperature profiles and location of those profiles from the eight out of 14 flights the C-130 plane did from the equator northward during EPIC. Under each plot with the temperature profiles are the locations of the dropsondes. Only profiles south of 6.5° N are plotted. The first dropsonde was deployed near the equator, usually between 18:00 UTC and 20:00, then roughly every 20 min one degree further north.

5-A-1-a: Dropsonde soundings from the National Science Foundation (NSF) C-130 aircraft

Only in eight out of the 14 flights did the plane actually fly all the way to the equator. In the other six cases, the plane stayed further north in the ITCZ. The eight flights on September 7,14, 19, 23, 25 and October 2, 9 and 10 2001 all show a clear temperature inversion near the equator that lifts and weakens as the plane progresses towards the north and into the ITCZ. Fig. 5.1 shows the temperature profiles and release locations of the southernmost dropsondes of those eight flights. The base of the temperature inversion in the profiles closest to the equator lies for most flights around 700 m. The inversion base height lifts to between 1100 m and 1250 m in most cases before it disappears. At 6° N, the profiles don't show a clear inversion anymore, so the profiles plotted are limited to

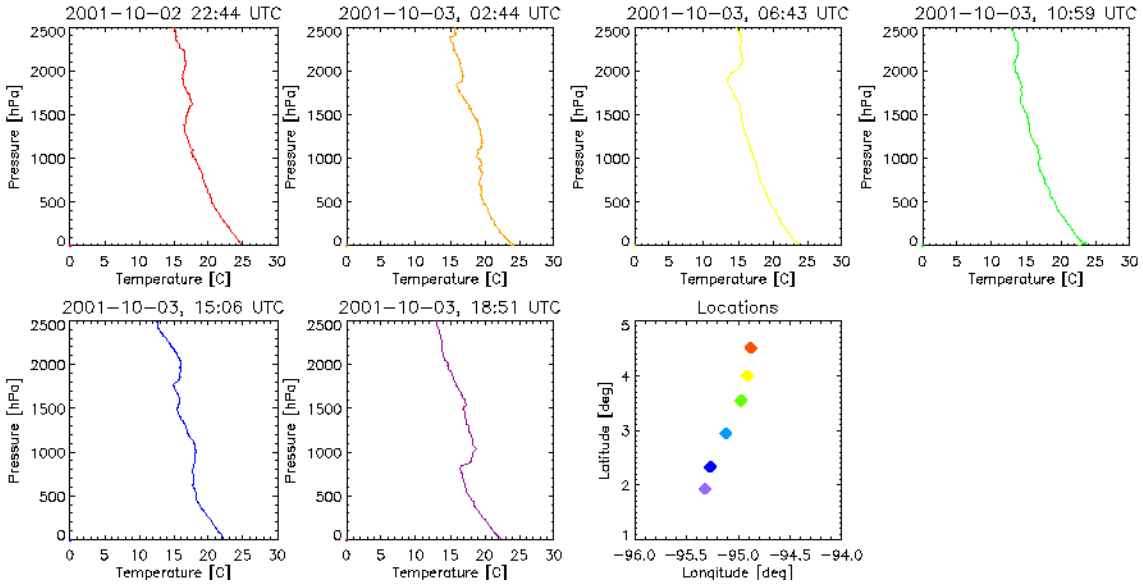

Figure 5.2: Temperature profiles from select Ronald H. Brown EPIC (Leg 1) radiosondes.

latitudes between 0° and 6.5° N.

5-A-1-b: Radiosonde soundings from the Ronald H. Brown's leg 1 of the cruise

During the first leg of the Ronald H. Brown's EPIC cruise, the ship spent the majority of its time at a buoy location in the ITCZ at 95° W, 12° N (September 12 to October 1 2001). Then it traveled on along the 95th meridian towards the Galapagos Islands before continuing on to Leg 2. Only 14 out of the 140 sondes released during Leg 1 were released on the trip south towards the Galapagos Islands. The soundings from the ITCZ buoy are of less interest for this study because they are more concerned with the temporal variability of the atmosphere at a fixed location rather than large spatial coverage. Also, few of those soundings show a clear indication of a temperature inversion and therefore they are of little help in defining a distinct PBL top. Fig. 5.2 shows the six southernmost temperature profiles. Though all of the profiles have weak inversions at some height or another, the inversions are not as distinct as in the profiles from the dropsondes, and the inversions appear at very different heights.

5-A-1-c: Radiosonde soundings from the Ronald H. Brown's leg 2 of the cruise

The Ronald H. Brown cruised the south east Pacific ocean from October 9th to October 25th 2001. During this leg of the cruise, the ship traveled from the Galapagos islands (90.3° W, 1.2° S) to IMET mooring site at (85.0° W, 20.0° S), where it stayed for six days and then continued on to Arica, Chile (70.3° W, 18.3° S). 54 of a total of 116 soundings were taken at the mooring, the rest along the ship track. Fig. 5.2 shows

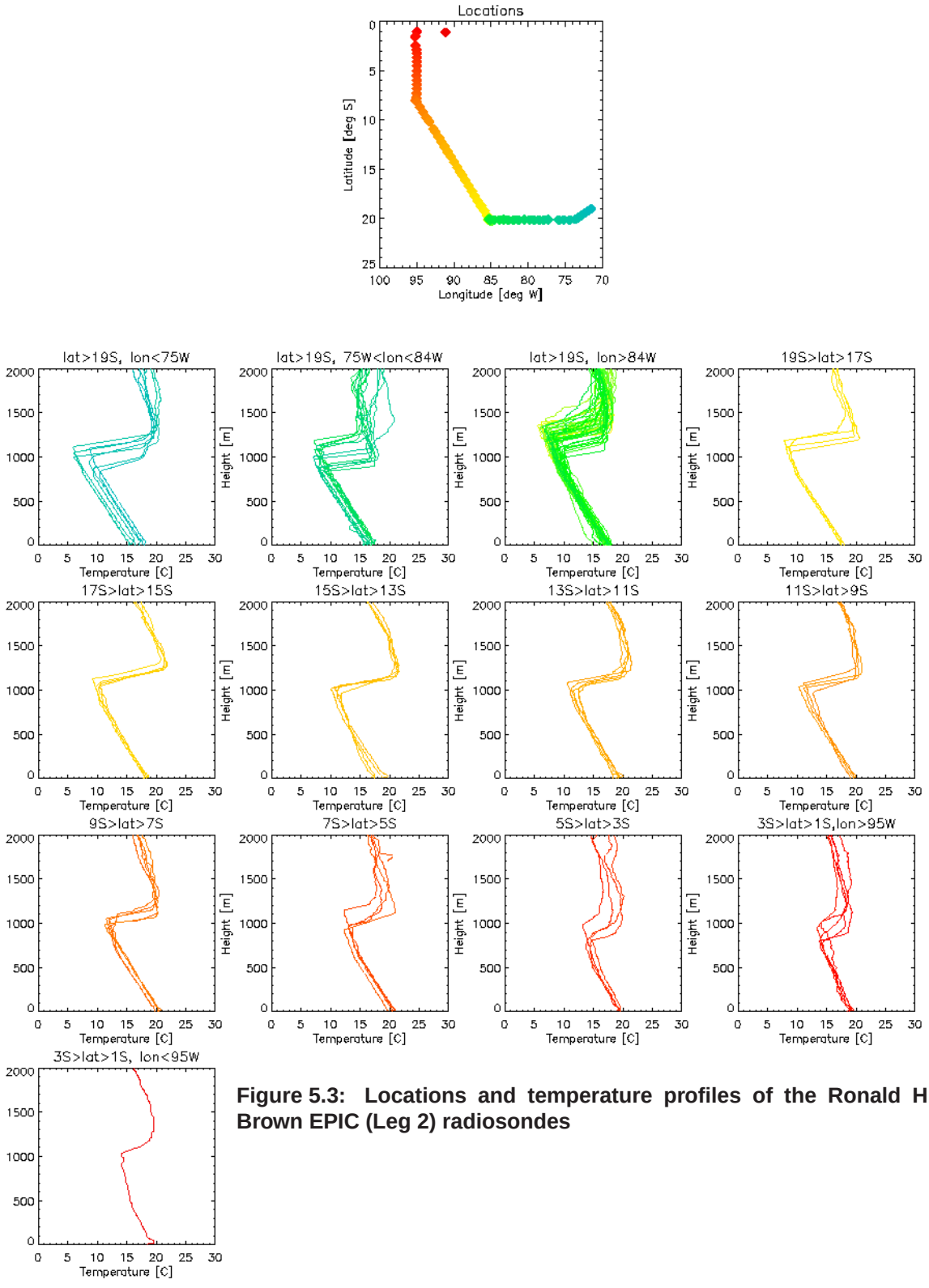

Figure 5.3: Locations and temperature profiles of the Ronald H. Brown EPIC (Leg 2) radiosondes

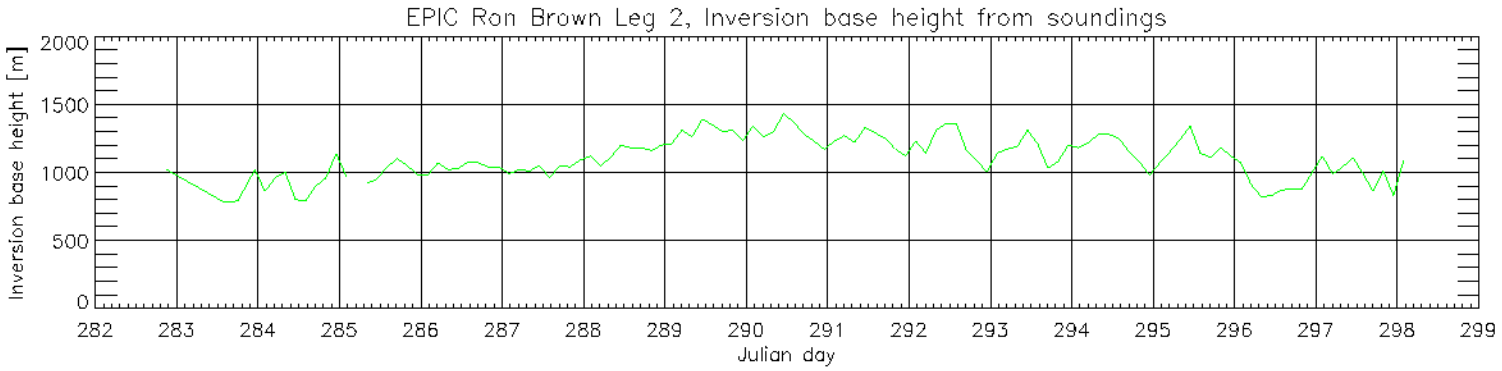

Figure 5.4: Time series of inversion base height obtained from Ronald H. Brown (Leg 2) radiosonde temperature profiles

temperature profiles sorted into longitude-latitude bins as designated in the title of each plot. The ship track is shown in the last plot. The strong temperature inversion in all soundings is obvious. The inversion is stronger and more distinct in the soundings closer to the Chilean coast (blue). In the soundings closer to the equator (red), the inversion becomes weaker and less distinct. Using an algorithm that picks out the slope reversal in the temperature soundings, we determine the inversion base height. The algorithm works well for most soundings. One sounding has too much missing data, and for eight more soundings the algorithm failed to find the inversion base height. In these cases, the inversion base height was determined subjectively by looking at the particular sounding. The vertical resolution of the soundings is 10 m. Fig. 5.3 is a plot of the inversion base height along the ship track against the Julian day of the year 2001. If we consider the inversion base height as a measure of PBL depth, this plot shows an average PBL depth of ~1190 m. During part of the timeseries, a diurnal cycle is evident (Julian days 289 to 296) with deeper PBLs in the middle of the Julian day (this corresponds to the early morning local time). The overall variability of the inversion base height is on the order of several hundred meters. This is true for the diurnal variability as well as for the spatial variability along the ship track. Note that the ship was stationary from Julian day 288 to 294, and that the temporal variability over this time period is approximately the same as the spatial variability from the Chilean coast to the Galapagos Islands. It is therefore impossible to tell if, in the time average, the inversion base height slopes up away from Chilean coast, as is the case off the Californian coast. During the cruise, the inversion base was never lower than 780 m or higher than 1430 m, and the change in inversion base height from one

sounding to the next never exceeded 260 m.

5-A-1-d: Summary

The variability of the PBL depth as derived from the inversion base height of the EPIC soundings is much smaller than what the timeseries from the GCM (presented in Chapter 4) shows. The average PBL depth is close to 1200 m away from equator, and somewhat lower over the cold tongue, as derived from the dropsonde profiles.

The picture that emerges from all of the EPIC soundings is that of universal, strong temperature inversions in the east Pacific between equator and 20° S, with an average inversion base height of ~1200 m and an overall variability of 200-300 m. Close to the equator and just north of it, the temperature inversion is weaker and not always as distinct as south of the equator (Ronald H. Brown Leg 1). The inversion base height seems to be lower there (700 m to 900 m), increasing and weakening northward until the inversion disappears at 5° to 6° N. Comparing this to the October 2001 MLM run (Fig. 4.11 d), the

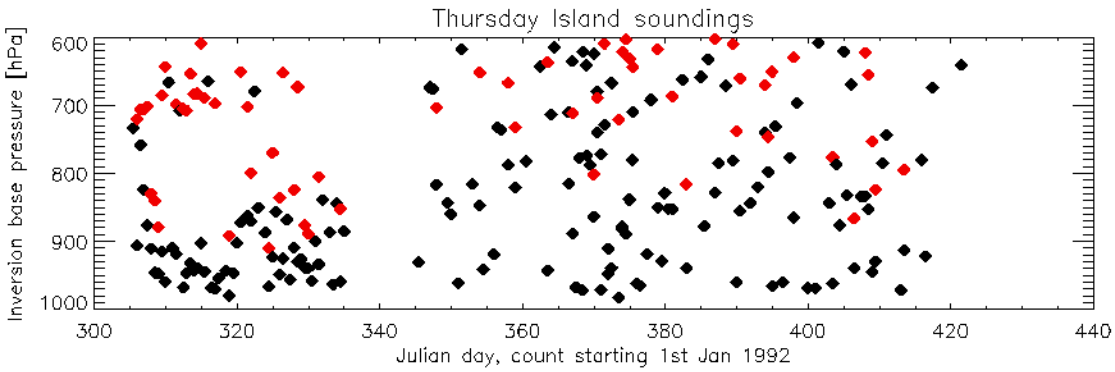

Figure 5.5: Inversion base height at Thursday Island, black diamonds indicate the lowest detected inversion base, red diamonds a secondary inversion base.

MLM's PBL depth is several hundred meters too low. It varies from ~700 m at (80° W, 20° S) to less than 300 m over the cold tongue and then increases northward to ~1200 m in the ITCZ. The MLM model captures the shallower depths over the cold tongue and the increase into the ITCZ, but the MLM's overall variability in the EPIC area is larger than observed. In the modified run shown in Fig. 4.30, the PBL depth is even smaller, but the variability is smaller as well.

5-A-2 TOGA/COARE

The Tropical Ocean Global Atmosphere/Coupled Ocean Atmosphere Response Experiment (TOGA/COARE) set out to investigate the coupled ocean-atmosphere in the warm pool. Little attention has been paid to non-convective phases where an inversion-topped mixed layer similar to the EPIC cases develops. That this is the case has been observed, among, others by Johnson et al. (1996) and Johnson and Lin (1997), though

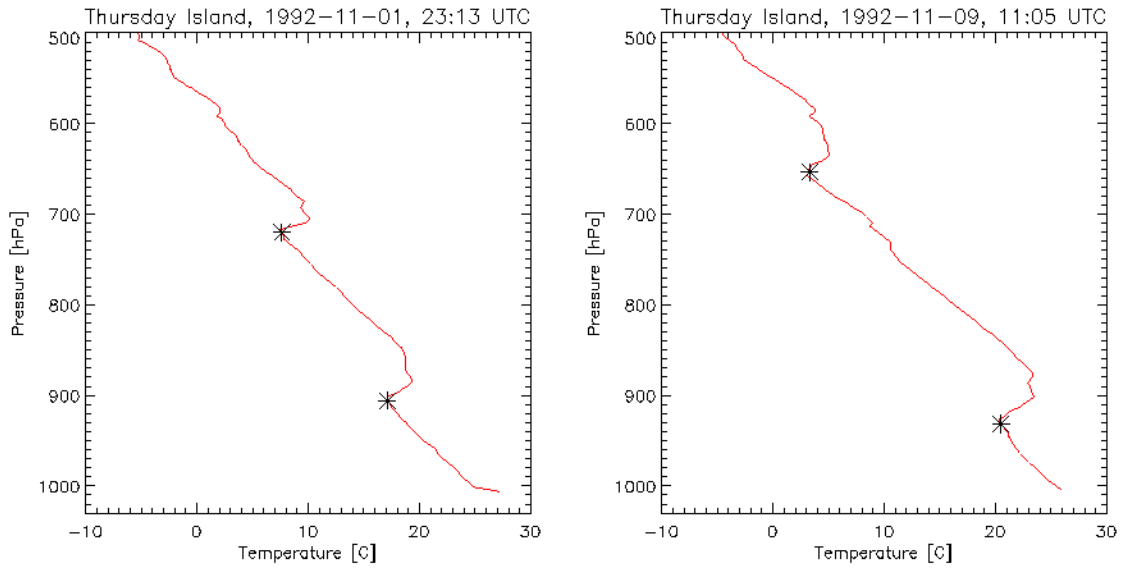

Figure 5.6: Sample profiles from Thursday Island, the stars mark the inversion base as detected by the algorithm mentioned in the text.

more as an aside. Similarly, Yin and Albrecht (2000), for example, found that during the First GARP Global Experiment (FGGE) temperature inversions around 800 hPa were not unusual in the central equatorial Pacific. Fig. 5.5 shows a plot of inversion base height at the sounding location Thursday Island (142.2°E, 10.6°S) as determined through an algorithm that searches for an increase in potential temperature with height that exceeds a certain threshold. This algorithm is not very discriminating and tends to miss very weak inversions and inversions with a more gradual rather than sharp increase in potential temperature. Nevertheless, there is a distinction in Fig. 5.5 between the first month of observations (November 1992, Julian days 305 to 334) and the following three months. In November, the inversion base height lies around 900 hPa, with a secondary inversion around 700 hPa and few inversions detected between those levels. In addition, Fig. 5.5 illustrates how noisy conditions are at Thursday Island. Two sample profiles from November are shown in Fig. 5.6, the inversion bases marked with a star. The upper inversion is the tropical inversion near the 0°C level described by Johnson et al. (1996). The inversion base in November 1992, when detected at all, ranges between 500 m and 1300 m. The island sits off the northernmost tip of Australia and south of New Guinea, and would therefore be influenced by the continents.

5-A-2-a: Summary

The soundings from the TOGA/COARE experiment show that the mixed-layer approach is not only applicable to the mixed subcloud layer in situations with deep convection, but is also be viable during non-convective phases. Traditionally, the mixed-

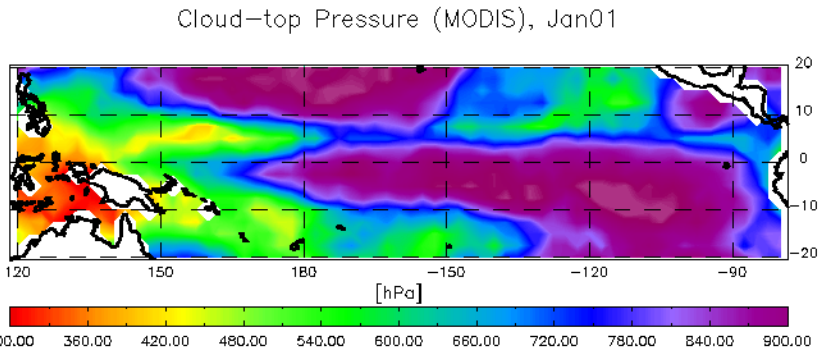

Figure 5.7: a) Monthly mean MODIS cloud-top pressure for January 2001

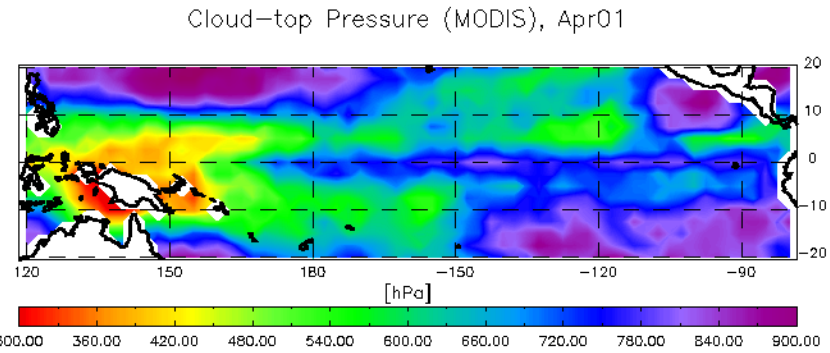

Figure 5.7: b) same as a) for April 2001

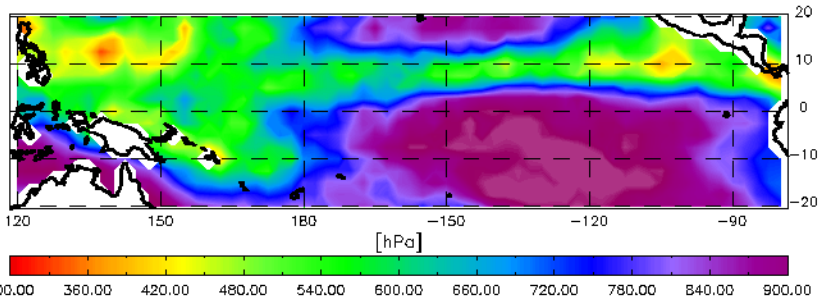

Figure 5.7: c) same as a) for July 2001

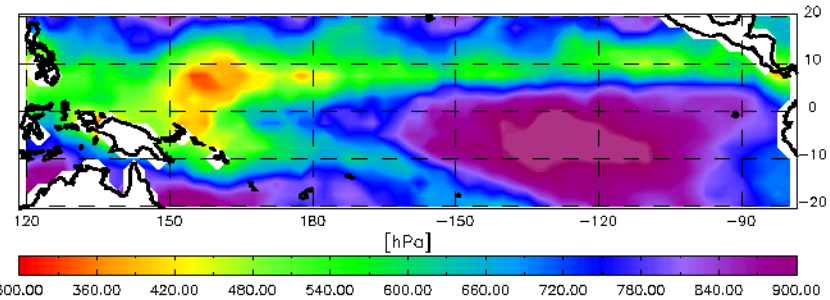

Figure 5.7: d) same as a) for October 2001

layer approach has been associated more with the stratocumulus-topped PBL. It seems it may do a reasonable job describing the PBL even in the warm pool area. In Chapter 3, the MLM with GCM input performed best in the warm pool area and the SPCZ.

5-B: Observations with global coverage

More recently, methods have been developed to retrieve the PBL depth from satellite data. Two products are cloud top pressure from the Moderate Resolution Imaging Spectroradiometer (MODIS) aboard the Terra Earth Observing System platform, and Geoscience Laser Altimeter System data from the Ice, Cloud, and land Elevation (ICESat) satellite launched in February 2003.

5-B-1 MODIS cloud-top pressure

Fig. 5.7 a) through d) show the monthly mean cloud-top pressure for the four 2001 sample months on a $1^\circ x1^\circ$ grid. In the averaging process, clear-sky pixels are neglected, i.e. one pixel per $1^\circ x1^\circ$ grid box per month is enough to make that grid non-missing. No pixel count screening is done. As mentioned in Chapter 2, the CO_2 slicing method used in this retrieval works only for pressures lower than ~700 hPa because the signal strength is too weak in the lower atmosphere. For the lower atmosphere, the cloud-top temperature is determined from the $11-\mu m$ infrared band, assuming the cloud is optically thick, and the cloud-top pressure is assigned by comparison to the NCEP Global Data Assimilation System (GDAS) temperature profile. Therefore, the cloud-top pressure is most inaccurate for the low clouds of interest here. Surprisingly, this data set indicates that the monthly mean cloud top just off the Chilean coast lies around 750 hPa and that the cloud-top

pressure increases off shore to about 890 hPa. This seems contrary to, for example, the EPIC observations in this region. This maybe the result of the limited applicability of the CO_2 slicing method, as mentioned above.

Comparing Fig. 4.11 a) through d) to Fig. 5.7 a) through d) we see that the MLM does a fairly good job of picking out the areas of high and low cloud tops as observed by MODIS. If the cloud-top pressures of the MODIS retrieval can be trusted, the lowest observed cloud tops in the south-central Pacific roughly correspond to 1000 m PBL depth. Compared to this number, the MLM's PBL depths in the low hundreds of meters are too low. Interestingly, those spots of above-scale PBL depth in Fig. 4.11 a) through d) roughly correspond to those areas with lowest cloud-top pressure in the MODIS figures.

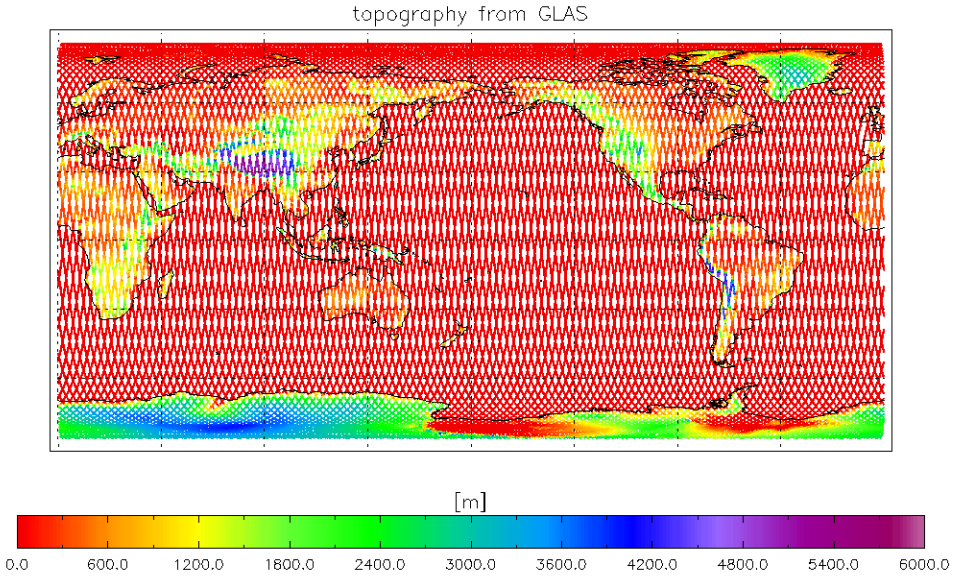

Figure 5.8: Topography as detected by GLAS, preliminary data set

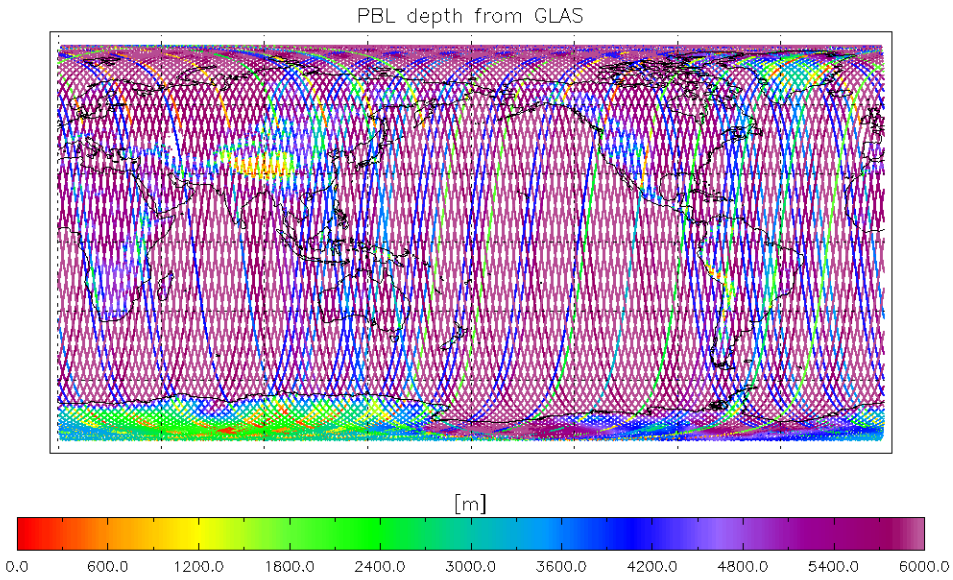

Figure 5.9: PBL depth as detected by GLAS, preliminary data set

5-B-2 GLAS

Shortly after its release in October 2003, we obtained the preliminary PBL data from the GLAS (Geoscience Laser Altimeter System, see section 2-C-4 on page 30) instrument. The PBL depth is determined at a 4 s sampling rate from the 532 nm channel only. The PBL is the lowest distinct layer of aerosols that can be resolved by the instrument. The retrieval is given a confidence rating based on the ratio of the average signal within the PBL to the signal above the PBL and is flagged for clear or cloudy conditions. The PBL thickness (top minus ground height) cannot exceed 6 km. If the layer top is greater than 6 km above the local ground height, it is not identified as the PBL top. The PBL top is first searched by using a 4 s average profile. If the top is found at that resolution, then the PBL top is located from each of the 20 (5 Hz) shots that make up that 4 sec period.

The preliminary data shows that the retrieval does a good job at detecting the topography, but the PBL depth is 6 km almost everywhere, indicating that no PBL top could be identified. Obviously, work still has to be done, or perhaps unreported work already has been done, on the PBL depth retrieval. For purposes of this thesis, the GLAS data is unfortunately of little help.

5-C: Observations of entrainment velocity

One of the foci of the Dynamics and Chemistry of Marine Stratocumulus (DYCOMS-II) Experiment in 2001 was to measure entrainment of the stratocumulus topped boundary layer off the Californian coast. The evaluation of data obtained on this field experiment has just begun. Early results place the measured nighttime entrainment velocity between 0.3 and 0.7 cm s^{-1} (Faloona et al. submitted). The MLM's entrainment velocity lies at the low end of this range.

5-D: Summary

Due to the lack of observations of similar coverage as the model's input data (global, gridded, monthly mean) it is hard to directly compare the model output with observations. Comparing the MLM's PBL depth to what observations are available, the MLM performs well when it comes to distinguishing between non-convective and convective regions, but the magnitude of the PBL depth is comparatively low. The spatial variability of the PBL depth over the domain is a little higher than that of the EPIC observations. The MLM's entrainment velocity falls into the general range of the observed entrainment velocities. Until more observational data is available, we cannot say whether

the MLM's entrainment velocity distribution over the domain is correct or not.

One cannot help but notice that the various observations mentioned in this chapter do not agree very well with each other. The upward slope of the trade inversion off the Californian coast is a well observed phenomenon. Similar observations off the Chilean coast are fewer and not as conclusive. The map created by Neiburger (1961) from ship based radiosonde observations over half a century ago (Fig. 1.1) does show an upward slope of the inversion base height. The EPIC cruise however does not show a significant slope in the statistical sense. The sample size is simply too small. While the MODIS monthly mean cloud-top pressure does a good job distinguishing between deep convective regions and stable regions, the cloud-top pressure is rather low (around 750 hPa) off the coast of Chile with a gradual downslope towards the west. The pixel-level MODIS product as presented by Platnick et al. (2003) also shows a rather low cloud-top pressure of about 720 hPa off the Chilean coast for July 18, 2001 at 15:30 UTC. The highest cloud-top pressures can be found in the central south Pacific. This is rather contrary to surface based observations, which place either shallow convection with cloud top pressures similar to or lower than the stratocumulus', or clear sky in this area. Since no pixel screening is done during the averaging process, we cannot know how robust the monthly mean is over the south central Pacific. As mentioned before, the cloud-top retrieval does not work as well for low clouds as it does for mid level and high clouds. The retrieval method may also work better for one type of low clouds compared to another (shallow cumulus vs. marine stratocumulus).

So far, the lidar-based PBL depth products are of little use for comparison with global-coverage, time-averaged model output. In the future, a more comprehensive set of lidar data will be invaluable for model validation and other large scale applications.

Chapter 6: Conclusions

6-A: Summary and Conclusion

This thesis set out to assess the mixed-layer model's ability to diagnose the three PBL parameters PBL depth, entrainment velocity and cumulus mass flux velocity from monthly mean data over the tropical Pacific. This assessment was done through comparison with existing observational data and a month-long run from the CSU GCM, which uses a time-dependent but otherwise similar mixed-layer scheme.

This study differs from previous work (e.g., Stevens et al., 2002; Stevens, 2002; Wood and Bretherton, submitted) in that it purposefully applies the mixed layer concept to the whole domain. While some GCMs use the mixed-layer scheme on a global scale, this is usually done because of the scheme's simplicity and low computational expense, not so much to assess its applicability for different types of PBL. In-depth studies involving the mixed-layer concept are usually confined to the stratocumulus regime. Last but not least, the MLM discussed here diagnoses PBL depth, entrainment and cumulus mass flux velocity rather than parameterizing these variables and predicting PBL properties such as temperature, moisture and surface fluxes.

6-A-1 Conclusions about nature

Ignoring for a moment the many uncertainties concerning the MLM's

performance, its output can tell us something about the spatial and seasonal distribution of PBL depth, entrainment velocity and cumulus mass flux velocity.

The PBL depth is generally lowest over the cold tongue and along the Equator and increases polewards. It can be as shallow as 300 m at its minima, and increases to over 1500 m in the convective regions (ITCZ, SPCZ and warm pool, as well as the southern ITCZ in April and January), occasionally even exceeding 3000 m. In the non-convective areas, the PBL depth averages at about 800 m. Overall, the SPCZ, marked by a band of deep PBL, is fairly parallel to the Equator, and there is evidence of a southern ITCZ in April, and to a lesser extent in January. The horizontal gradients of the PBL depth can be very large.

The entrainment rate is smallest over the cold tongue and along the Equator and increases poleward. Other than this general pattern, there is little additional structure in the fields that might be consistent with, e.g., cloud regimes. The largest entrainment velocities generally occur where the PBL is deep. Over most of the domain, the entrainment velocity varies between 1.5 mm s^{-1} and 3 mm s^{-1}. For the runs with reduced q_B and increased s_B, the entrainment velocity is 0.5 mm s^{-1} larger (Fig. 4.26 a) through d)).

The cumulus mass flux velocities from the original NCEP re-analysis runs are so obviously dominated by noise that any deduction from the model output to the actual state of the atmosphere seems unjustified. The results from the run with reduced q_B and increased s_B look somewhat better. Here, the model results indicate the largest cumulus

mass flux velocities, as well as largest horizontal gradients in w_C, in the ITCZ and SPCZ, and in case of April and January, the southern hemisphere's ITCZ. This is most apparent in October and probably April. The magnitude of cumulus mass flux velocity ranges between 2.5 mm s^{-1} and 5 mm s^{-1} over most of the domain. Velocities above 2 cm s^{-1} are usually confined to small areas and negative velocities, where they appear, are generally small.

We are aware that the MLM is only a model and any conclusions drawn from the model's output have to carefully weighed by the model's performance.

Of the three PBL parameters, the PBL depth is the one we know most about. It appears that the PBL depth from the MLM is generally lower, and horizontal gradients larger, than suggested by the available observations. In a north-south cross section at 100° W for the month of April, the PBL depth increases by 1600 m over one grid box (2.5°), for example, which is the equivalent of a gradient of 5.7×10^{-3} m m^{-1}. This is one order of magnitude larger than observed (300 m per 1000 km, or 3×10^{-4} m m^{-1}, see Chapter 1). The same gradient is reduced by a factor of three in the runs with reduced q_B and increased s_B (Fig. 4.24 b). Firestone and Albrecht (1986) also remark on how relatively invariant the trade wind inversion height is across the Pacific ocean. If we take the inversion height as a measure for the PBL depth, this suggests that the MLM seriously overestimates the horizontal gradients in PBL depth. The EPIC data shows a PBL depth around 1100 m with relatively low temporal and spatial variability in the eastern Pacific, a

PBL several hundred meters deeper than the one diagnosed by the MLM. Those same observations also suggest generally lower PBL depths over the cold tongue, a pattern that the MLM does capture.

We know less about the entrainment and cumulus mass flux velocities. The MLM suggests that entrainment velocities of several $\mathrm{cm\,s^{-1}}$, as in the GCM, are too large and that the entrainment velocity should not exceed $1\ \mathrm{cm\,s^{-1}}$. This is in agreement with preliminary results from DYCOMS-II. The MLM also diagnoses large entrainment in areas with a deep PBL, and small entrainment in areas of shallow PBL depths. This is consistent with the concept that strong entrainment leads to deeper PBLs. We have even fewer constraints for the cumulus mass flux velocity. From the model formulation, the cumulus mass flux velocity should be maximal in areas of strong convection, and be close to zero in areas without convection. It should never be negative. The MLM fails on the last point, and can barely distinguish between convective and non-convective regions. The MLM results for this quantity are therefore, at best, unreliable.

6-A-2 Conclusions about the method

Comparing the MLM to the GCM shows that the steady state assumption introduces errors by neglecting the time-dependent part of the fluxes across the PBL top. Leaving out those fluxes leads to unrealistically low PBL depths, as well as unreasonably large PBL depths in some convective areas. This is, however, a result based on input data generated by the GCM, which are not necessarily without errors themselves. This is particularly apparent in the GCM surface buoyancy flux near the continental coasts, as

well as in a very moist free atmosphere of the GCM. Also, this result cannot be reproduced when the MLM is run with NCEP re-analysis data. Here, the time-dependent fluxes, such as can be determined from the re-analysis data, do not have a significant impact on the MLM's results.

In the MLM run with GCM input data, the model performs best in the warm pool - SPCZ area, and worst along the ITCZ. For the NCEP re-analysis runs, weak spots in the model output (i.e. PBL depth larger than 3 km) usually occur in areas of deep convection. Without more reliable observations, we cannot say that the MLM performs best in any one particular area of the domain. With the general upslope of the PBL top towards the convective regions, the MLM's PBL top appears to be most in line with the trade inversion level, which has been observed to gradually slope up into the ITCZ. It is not quite clear, then, where the MLM places the PBL top in the deep convective zones. The PBL depth is largest there, but in the real atmosphere, the mixed layer in those regions consists of the mixed subcloud layer, whose top (i.e. the cloud base) is usually lower than the average trade inversion.

The MLM succeeds in diagnosing a positive PBL depth and entrainment velocity of reasonable magnitude. This result depends critically on the linear-with-height formulation of radiative cooling. For a fixed radiative cooling, all three diagnosed parameters show large areas with negative values. The MLM's formulation is also sensitive to the PBL top jumps in q and θ (or s), but less so to the absolute magnitude of q_B, θ_B (s_B), q_H and θ_H (s_H) (i.e. the pressure level chosen to represent mixed-layer

values and above-PBL values). This is not surprising, considering the formulation of the model equations. The above-PBL values enter the equations only in form of the PBL top jump in the entrainment terms. The mixed-layer values, in addition to their contribution in the entrainment terms, show up only as gradients in the advective terms. A linear dependence of the PBL top jumps on height reduces the horizontal gradients of the diagnosed parameters and increases the entrainment velocity, with the result of increasing the areas with positive cumulus massflux velocities over the domain. Unfortunately, it also leads to an overall even shallower PBL.

The fixed PBL water vapor mixing ratio results in a somewhat counterintuitive behavior of the model when the PBL is moistened by a reduction in entrainment: Even though less air is entrained into the mixed layer, the model tends to increase the PBL depth to maintain a constant mixing ratio.

6-A-3 Conclusions about the GCM

This study has shed light on some of the characteristics of the GCM's boundary layer scheme. The monthly mean PBL properties in the warm pool and in the SPCZ are well described by the steady component of the input fields, hence the good agreement in this region between the full GCM run and the MLM with its steady state assumption. The ITCZ is the area where the time-varying component of all the input fields is essential for the GCM's results. It is curious that, despite this, there is no indication of the ITCZ in the monthly mean PBL depth field.

Timeseries of the PBL properties at various grid points elucidate the boundary

layer scheme's behavior: The PBL depth in the GCM is constrained between ~ 200 m and ~1500 m. If the PBL depth wants to exceed the upper limit, or collapses due to a decrease in turbulence (triggered, e.g., by a decrease in surface buoyancy flux), the model responds by removing air from the PBL through the cumulus mass flux, in case of existing convection, or through negative entrainment velocities, in the case where no convection is present. Since the GCM uses an upstream scheme, the air removed from the PBL by either flux always carries PBL properties.

On the positive side, the monthly mean PBL depth is very smooth and its magnitude is in good agreement with observations, particularly in the non-convective areas. The spatial distribution of the monthly mean entrainment and cumulus mass flux velocities are good as well: Entrainment is largest in the stratocumulus regions, and the cumulus mass flux velocity has its maxima right where the model's convective precipitation is largest. Some of the timeseries even show indications of a diurnal cycle in the cumulus mass flux velocity.

On the negative side, the GCM's monthly mean entrainment velocity is actually negative along the coast lines. In addition, the ITCZ is absent in the monthly mean PBL depth, but the SPCZ is well developed and maybe a little too parallel to the Equator. Timeseries of all three PBL parameters show that, although the monthly mean fields are nice and smooth, the parameters change rapidly from hour to hour. This is not the case in the EPIC observations, for example. In some parts of the domain, the PBL depth swings rapidly between the maximum and minimum PBL depth allowed by the GCMs boundary

layer scheme. In non-convective regions, a deflation of the PBL is frequently facilitated by negative entrainment velocities. Along the continental coasts, where the monthly mean entrainment velocity is negative, the surface buoyancy flux is very large and negative, obviously a shortcoming of the GCM. Also, the surface sensible heat flux is negative over large parts of the domain, and the air above the PBL top appears to be too moist.

6-A-4 General Conclusion

Concluding, we can state that it is possible to diagnose PBL depth, entrainment velocity and, to a point, cumulus mass flux velocity from available monthly mean data and produce results that lie inside the general bounds derived from observations. Data is too scarce, at this point, for a case-by-case comparison of diagnosed quantities with observed quantities (, which of course was one of the reasons to diagnose those PBL quantities in the first place). The model shows some weaknesses, e.g., a tendency for an overall low PBL depth, spots with very high PBL depth in the convective regions, and negative cumulus mass flux velocities.

6-B: Outlook

There is still room for improvement in the MLM's formulation. A more "interactive" model, i.e. one that involves more realistic functionalities with height, for example, than a linear relationship, is likely to further improve the model's performance. This would, however, alter the setup from a linear set of equations that can be solved analytically to one that needs to be solved iteratively in some manner. This would move the MLM from a simple diagnostic tool to a more complicated prognostic model whose

behavior may be harder to interpret and understand. An expansion of the model to include precipitation in a more realistic way than was briefly described in Chapter 2, might also be interesting. The noise in the cumulus mass flux velocity field that is in part responsible for the occasional negative values might be reduced by an improved finite difference scheme, or a smoothing of the PBL depth field prior to the differencing.

In order to better evaluate the model results, satellite-based observations of the PBL depth will be invaluable. It is unlikely that there will be global observations of entrainment and cumulus mass flux velocities anytime soon, if ever. With reliable observations of PBL depth, the model could be better constrained. In fact, if the now diagnosed PBL depth could be replaced by observations, the presumably smoother field might well solve the problem of the negative mass flux velocities.

REFERENCES

Arakawa, A., 1969: Parameterization of cumulus convection. *Proc. WMO/IUGG Symp. Num. Wea. Pred.*, Tokyo, Japan Meteor. Agency. IV, **8**, 1-6.

Ball, F. K., 1960: Control of inversion height by surface heating. *Quart. J. Roy. Meteor. Soc.*, **86**, 483-494.

Betts, A. K. 1976: Modeling Subcloud Layer Structure and Interaction with a Shallow Cumulus Layer. *J. Atmos. Sci.*, **33**, 2363–2382.

Bougeault, P., and J.-C. André, 1986: On the Stability of the THIRD-Order Turbulence Closure for the Modeling of the Stratocumulus-Topped Boundary Layer. *J. Atmos. Sci.*, **43**, 1574–1581.

Bunker, A.F., B. Haurwitz, J.S. Malkus, and H. Stommel, 1949: Vertical Distribution of Temperature and Humidity over the Caribbean Sea. *Pap. Phys. Ocean. Meteor.*, **11**, 2-82.

Deardorff, J.W.. 1966: The Counter-Gradient Heat Flux in the Lower Atmosphere and in the Laboratory. *J. Atmos. Sci.*, **23**, 503–506.

Deardorff, J.W.. 1980: Cloud Top Entrainment Instability. *J. Atmos. Sci.*, **37**, 131–147.

Ding, P., and D. A. Randall, 1998: A Cumulus Parameterization with Multiple Cloud Base Levels. *J. Geophys. Res.*, **103**, 11341-11354

Faloona, I., D. Lenschow, T. Campos, B. Stevens, M. van Zanten, B. Blomquist, D. Thornton, A. Bandy, and H. Gerber, submitted. Observations of Entrainment in

Eastern Pacific Marine Stratocumulus Using Three Conserved Scalars.

Ficker, H. von, 1936: Die Passatinversion. *Veroeff. Meteor. Inst. Univ. Berlin*, **1**, 1-33.

Firestone, J. K., and B. A. Albrecht, 1986: The Structure of the Atmospheric Boundary Layer in the Central Equatorial Pacific during January and February of FGGE. *Mon. Wea. Rev.*, **114**, 2219–2232.

Fowler, L. D., D. A. Randall, and S. A. Rutledge, 1996a: Liquid and Ice Cloud Microphysics in the CSU General Circulation Model. Part 1: Model Description and Simulated Microphysical Processes. *J. Climate*, **9**, 489–529.

Fowler, L. D., and D. A. Randall, 1996b: Liquid and Ice Cloud Microphysics in the CSU General Circulation Model. Part II: Impact on Cloudiness, the Earth's Radiation Budget, and the General Circulation of the Atmosphere. *J. Climate*, **9**, 530–560.

Fowler, L. D., and D. A. Randall, 1996c: Liquid and Ice Cloud Microphysics in the CSU General Circulation Model. Part III: Sensitivity to Modeling Assumptions. *J. Climate*, **9**, 561–586.

Fowler, L. D., and D. A. Randall, 2002: Interactions between Cloud Microphysics and Cumulus Convection in a General Circulation Model. *J. Atmos. Sci.*, **59**, 3074–3098.

Grenier, H., and C. S. Bretherton, 2001: A Moist PBL Parameterization for Large-Scale Models and Its Application to Subtropical Cloud-Topped Marine Boundary Layers. *Mon. Wea. Rev.*, **129**, 357–377.

Harshvardhan, R. D., D. A. Randall, and T. G. Corsetti, 1987: A Fast Radiation

Parameterization for Atmospheric Circulation Models. *J. Geophys. Res.*, **92**, 1009 - 1016.

Holtslag, A. A. M., and C.-H. Moeng, 1991: Eddy Diffusivity and Countergradient Transport in the Convective Atmospheric Boundary Layer. *J. Atmos. Sci.,* **48**, 1690–1700.

Johnson, R. H., J. F. Bresch, P. E. Ciesielski and W. A. Gallus, 1993: The TOGA/COARE atmospheric sounding array: Its performance and preliminary scientific results. Preprints, *20th Conf. on Hurricanes and Tropical Meteorology,* San Antonio, TX, Amer. Meteor. Soc., 1-4.

Johnson, R. H., P. E. Ciesielski, and K. A. Hart, 1996: Tropical Inversions near the 0°C Level. *J. Atmos. Sci.,* **53**, 1838–1855.

Kirtman, B. P., Y. Fan, and E. K. Schneider, 2002: The COLA Global Coupled and Anomaly Coupled Ocean–Atmosphere GCM.. *J. Climate*, **15**, 2301–2320.

Klein, S. A., D. L. Hartmann, and J. R. Norris, 1995: On the Relationships among Low-Cloud Structure, Sea Surface Temperature, and Atmospheric Circulation in the Summertime Northeast Pacific. *J. Climate*, **8**, 1140–1155.

Kloesel, K. A., and B. A. Albrecht, 1989: Low-Level Inversions over the Tropical Pacific—Thermodynamic Structure of the Boundary Layer and the Above-Inversion Moisture Structure. *Mon. Wea. Rev.,* **117**, 87–101.

Lappen, C.-L., and D. A. Randall, 2001: Toward a Unified Parameterization of the Boundary Layer and Moist Convection. Part I: A New Type of Mass-Flux Model. *J. Atmos. Sci.,* **58**, 2021–2036.

Lietzke, C. E., C. Deser, and T. H. Vonder Haar, 2001: Evolutionary Structure of the Eastern Pacific Double ITCZ Based on Satellite Moisture Profile Retrievals. *J. Climate*, **14**, 743-751.

Lilly, D. K., 1968: Models of cloud-topped mixed layers under a strong inversion. *Quart. J. Roy. Meteor. Soc.*, **94**, 292-309.

Ma, C.-C., C. R. Mechoso, A. W. Robertson, and A. Arakawa, 1996: Peruvian Stratus Clouds and the Tropical Pacific Circulation: A Coupled Ocean-Atmosphere GCM Study. *J. Climate*, **9**, 1635–1645.

Malkus, J. S., 1958: On the Structure of the Trade Wind Moist Layer. *Pap. Phys. Ocean. Meteor.*, **13**, 2-47.

Mellor, G. L., and T. Yamada, 1974: A Hierarchy of Turbulence Closure Models for Planetary Boundary Layers. *J. Atmos. Sci.*, **31**, 1791–1806.

Menzel, W. P., W. L. Smith, and T. R. Stewart, 1983: Improved Cloud Motion Wind Vector and Altitude Assignment Using VAS. *J. Appl. Meteor.*, **22**, 377–384.

Moeng, C.-H., and J. C. Wyngaard, 1989: Evaluation of Turbulent Transport and Dissipation Closures in Second-Order Modeling. *J. Atmos. Sci.*, **46**, 2311–2330.

Moeng, C.-H., 2000: Entrainment Rate, Cloud Fraction, and Liquid Water Path of PBL Stratocumulus Clouds. *J. Atmos. Sci.*, **57**, 3627–3643.

Neiburger, M., D. S. Johnson and C. W. Chien, 1961: Studies of the structure of the atmosphere over the Eastern Pacific Ocean in summer, I, The inversion over the Eastern North Pacific Ocean. *Univ. Calif. Publ. Meteor.*, **1**, No.1.

Pan, D.-M., and D. A. Randall, 1998: A Cumulus Parameterization with a Prognostic Closure. *Quart. J. Roy. Met. Soc.*, **124**, 949-981

Platnick, S., M. D. King, S. A. Ackerman, W. P. Menzel, B. A. Baum, J. C. Riedi, and R. A. Frey, 2003: The MODIS cloud products: algorithms and examples from Terra. *IEEE Transactions on Geoscience and Remote Sensing*, **41**, 459- 473.

Randall, D. A. 1980 a: Entrainment into a Stratocumulus Layer with Distributed Radiative Cooling. *J. Atmos. Sci.*, **37**, 148–159.

Randall, D. A. 1980 b: Conditional Instability of the First Kind Upside-Down. *J. Atmos. Sci.*, **37**, 125–130.

Randall, D. A., Q. Shao, and M. Branson, 1998: Representation of clear and cloudy boundary layers in climate models. Clear and Cloudy Boundary Layers. *A. A. M. Holtslag and P.G. Duynkerke (eds.), Royal Netherlands Academy of Arts and Sciences, Amsterdam* , 302-322.

Randall, D. A., P. J. Sellers, J. A. Berry, D. A. Dazlich, C. Zhang, G. J. Collatz, A. S. Denning, S. O. Los, C. B. Field, I. Fung, C. O. Justice, C. J. Tucker, and L. Bounoua, 1996: A Revised Land-Surface Parameterization (SiB2) for Atmospheric GCMs. Part 3: The Greening of the CSU General Circulation Model. *J. Climate*, **9**, 738-763.

Ringler, T. D., R. P. Heikes, and D. A. Randall, 2000: Modeling the Atmospheric General Circulation Using a Spherical Geodesic Grid: A New Class of Dynamical Cores. *Mon. Wea. Rev.*, **128**, 2471–2490.

Schubert, W. H. 1976: Experiments with Lilly's Cloud-Topped Mixed Layer Model. *J.*

Atmos. Sci., **33**, 436–446.

Schubert, W. H., J. S. Wakefield, E. J. Steiner, and S. K. Cox, 1979: Marine Stratocumulus Convection. Part I: Governing Equations and Horizontally Homogeneous Solutions. *J. Atmos. Sci.*, **36**, 1286–1307.

Schubert, W. H., P. E. Ciesielski, C. Lu, and R. H. Johnson, 1995: Dynamical Adjustment of the Trade Wind Inversion Layer. *J. Atmos. Sci.*, **52**, 2941–2952.

Sellers, P. J., D. A. Randall, G. J. Collatz, J. Berry, C. Field, D. A. Dazlich, C. Zhang, and L. Bounoua, 1996a: A Revised Land-Surface Parameterization (SiB2) for Atmospheric GCMs. Part 1: Model formulation. *J. Climate*, **9**, 676-705.

Sellers, P. J., S. O. Los, C. J. Tucker, C. O. Justice, D. A. Dazlich, G. J. Collatz, and D. A. Randall, 1996b: A Revised Land-Surface Parameterization (SiB2) for Atmospheric GCMs. Part 2: The generation of global fields of terrestrial biophysical parameters from satellite data. *J. Climate*, **9**, 706-737.

Stevens, B., J. Duan, J. C. McWilliams, M. Münnich, J. D. Neelin, 2002: Entrainment, Rayleigh Friction, and Boundary Layer Winds over the Tropical Pacific. *J.Climate*, **15**, 30–44.

Stevens, B., 2002: Entrainment in Stratocumulus Topped Mixed Layers, *Quart. J. Roy. Meteorol. Soc.*,**128**, 2663-2690.

Stull, R. B., 1988: An Introduction to Boundary Layer Meteorology. *Kluwer Academic Publishers Group, Dordrecht, The Netherlands*, 666pp.

Waliser, D. E., and C. Gautier, 1993: A Satellite-derived Climatology of the ITCZ. *J.*

Climate, **11**, 2162–2174.

Wang, S., and B. A. Albrecht, 1990: A Mean-Gradient Model of the Dry Convective Boundary Layer. *J. Atmos. Sci.*, **47**, 126–126.

Winker, D. M., R. H. Couch and M. P. McCormick, 1996: An overview of LITE: NASA's Lidar In-space Technology Experiment. *Proc. of the IEEE*, **84**, 1-17.

Wood, R., C. S. Bretherton, in print: Boundary layer depth, entrainment and decoupling in the cloud-capped subtropical and tropical marine boundary layer. *J. Climate*.

Wylie, D. P., and W. P. Menzel, 1999: Eight Years of High Cloud Statistics Using HIRS. *J. Climate*, **12**, 170–184.

Yin, B., and B. A. Albrecht, 2000: Spatial Variability of Atmospheric Boundary Layer Structure over the Eastern Equatorial Pacific. *J. Climate*, **13**, 1574–1592.